INVESTIGATION OF FSO COMMUNICATION SYSTEM BASED ON VARIOUS MODULATION SCHEMES OVER COASTAL REGION OF SOUTH AFRICA

by

Kholekile Mtshiza

(20817081)

Submitted in fulfilment of the requirements for the degree of:

MASTER OF ENGINEERING

in the

DEPARTMENT OF ELECTRONIC AND COMPUTER ENGINEERING,

FACULTY OF ENGINEERING AND THE BUILT ENVIRONMENT

at the

DURBAN UNIVERSITY OF TECHNOLOGY

February 2025

Supervisor: Prof. N. Pillay

Co-Supervisor: Dr. E. O. Olurotimi

PREFACE

The growing interconnectedness of societies through smart technologies has accelerated demand for more robust and high-capacity wireless communication systems. This thesis presents an exploration of Free Space Optical (FSO) communication, a promising solution that uses light beams for wireless data transmission. FSO offers the potential for high-speed, long-distance, and energy-efficient communication, making it a compelling alternative or supplement to conventional radio frequency (RF) networks. However, FSO communication faces significant challenges, particularly in adapting to variable weather and atmospheric conditions that can impair signal quality and reliability.

This study seeks to expand the understanding of FSO communication's strengths and limitations in diverse meteorological environments, with a focus on two coastal regions in South Africa: Cape Town (west coast) and Port Elizabeth (east coast). Both locations present unique atmospheric conditions, impacting FSO signal performance. Using extensive meteorological data from the South African Weather Service (SAWS) and analyzing the effects of specific atmospheric parameters such as visibility, temperature, and humidity, this research investigates FSO signal attenuation over time and evaluates the performance of various modulation schemes. The findings are critical in understanding the influence of regional climate characteristics on FSO communication capabilities, specifically with respect to channel capacity and signal strength over varying distances. This work contributes to the field by modelling and simulating FSO transmission schemes across different propagation links and wavelengths, providing practical insights into bandwidth requirements and capacity potential for FSO links in real-world applications. Through this study, I hope to offer a foundational perspective that will guide future advancements in FSO communication, ultimately supporting more resilient wireless networks capable of adapting to environmental challenges.

Kholekile Mtshiza

Durban University of Technology

February 2025

DECLARATION 1: SUPERVISOR

According to the contents of this thesis, as the candidates' Supervisor, I agree to the submission of the thesis.

Prof. N. Pillay

(Main supervisor)

Date: 10/02/2025

Dr E. O. Olurotimi

(Co-supervisor)

Date: 10 February 2025

DECLARATION 2: PLAGIARISM

I, **Kholekile Mtshiza (20817081)**, the undersigned, declare that:

(i) The research reported in this thesis, except where otherwise indicated, is my original work.

(ii) This thesis has not been submitted for degree or examination at any other university.

(iii) This thesis does not contain other persons' data, images, graphs, or other information unless specifically acknowledged as being sourced from other persons.

(iv) This thesis does not contain other persons' writing unless specifically acknowledged as being sourced from other researchers. Where other written sources have been quoted, then:

a. their words have been re-written, but the general information attributed to them has been referenced.

b. where their exact words have been used, their writing has been placed inside quotation marks and referenced.

(v) Where I have reproduced a publication of which I am an author, co-author, or editor, I have indicated in detail which part of the publication was written alone and have fully referenced such publications.

(vi) This thesis does not contain text, graphics, or tables copied and pasted from the Internet unless specifically acknowledged and the source is detailed in the dissertation and the Reference sections.

Kholekile Mtshiza

February 2025

DECLARATION 3: PUBLICATIONS

I, **Kholekile Mtshiza (20817081)** declare that the following publications came from this thesis:

i. Free Space Optical Communication Link Performance Based on Various Transmission Schemes Over Gamma-Gamma Distribution Channel, in 3rd International Conference on Electrical, Computer and Energy Technologies (ICECET), 2023: IEEE, pp. 1-6. DOI: 10.1109/ICECET58911.2023.10389300.

ii. Free-Space Optical (FSO) Link for Different Transmission Schemes Influenced by Atmospheric Turbulence with Pointing Errors, in 4th International Conference on Electrical, Computer, and Energy Technologies (ICECET), 2024: IEEE, pp. 1-6. DOI: 10.1109/ICECET61485.2024.10698422.

iii. Performance Analysis of Subcarrier Intensity Modulation and Direct Detection (SIM/DD) on the Free Space Optical Communication (FSOC) Link under Atmospheric Turbulence and Weather Conditions, in 5th Euro-Mediterranean Conference for Environmental Integration, Italy, 2023. *Presented at the Conference and awaiting publication.*

iv. Evaluation of Fog-induced Attenuation on the Optical Signal Propagation Link in South Africa, in 6th Euro-Mediterranean Conference for Environmental Integration, Morocco, 2024. *Presented at the Conference and awaiting publication.*

ACKNOWLEDGEMENTS

This project could not have been completed without the guidance and strength of God Almighty.

I am indebted to my supervisors, Prof. N Pillay and Dr. E.O Olurotimi. I am grateful to my supervisors for their invaluable support and guidance during this study.

I thank my friends and family for believing in me.

This project was supported by a bursary from the DUT Staff Higher Education Subsidy financial scheme for funding my research work. Research funds were provided by Faculty research. During the journey of this research, I have acquired so much knowledge. To my family for their support, encouragement, and words of wisdom.

ABSTRACT

The recent advancement in intelligent technology, where the highest percentage of the population is connected through smart devices, requires robust wireless communications infrastructure. Free Space Optical (FSO) communication, a system that uses light beams to transmit data wirelessly, has recently emerged to enhance radio frequency (RF). The advantages include a large bandwidth over long distances, low power consumption, an unfettered spectrum, and sizeable high-speed data transfers. However, FSO communication has challenges, particularly the significant impact of weather conditions such as fog visibility, temperature, wind, and atmospheric turbulence on signals' performance and link availability. Furthermore, the scintillations directly impact the FSO communication performance, fading the signal and increasing the bit error rate. The primary objective of this work is to elucidate the functioning of the FSO system, a crucial step in examining various modulation strategies that rely on transmitting FSO signals through the Gamma-Gamma atmospheric channel. For this study, the influence of selected meteorological parameters (visibility range, wind speed, maximum temperature, and relative humidity) on FSO signal attenuation over Cape Town and Port Elizabeth in South Africa, is evaluated and demonstrated for the feasible performance, reliability, and resilience of the FSO communication link. This study utilized two years (2018-2019) meteorological data from the South African Weather Service (SAWS).

The average attenuation at the selected locations was calculated by quantifying the impact of aerosol scattering on signal strength, which is attributed to the visibility conditions in foggy environments. Wavelength-dependent parameters (about aerosol scattering) were computed using four distinct operating wavelengths, specifically 650 nm, 850 nm, 1200 nm, and 1550 nm, within the maximum transmission link of 5 km. The result demonstrates that the specific average attenuation at an average visibility of 25.96 km in Cape Town throughout the two years is 2.634 dB/km at 650 nm and 0.851 dB/km at 1550 nm. Port Elizabeth recorded a higher mean visibility of 28.34 km, surpassing Cape Town's value by 2.38 km, and the observed specific average attenuation is 2.412 dB/km at 650 nm and 0.779 dB/km at 1550 nm, respectively. Furthermore, three FSO transmission schemes have been evaluated and analyzed under atmospheric turbulences and weather conditions at 1550 nm

wavelength and three different propagation links. The power transmission was constant, only considering varying the required bandwidth for each scheme.

The system was modelled and simulated, thus achieving an average channel capacity of 4.559 bps/Hz in Cape Town at the highest transmission range of 2.5 km at a 35 dB signal-noise ratio. This capacity indicates the amount of data reliably transmitted per unit bandwidth. At a medium transmission range of 2.5 km, the achieved channel capacity is 44.928 bps/Hz in Port Elizabeth. However, Port Elizabeth has the highest transmission range of 3.5 km; the achieved channel capacity decreases drastically to 2.12 bps/Hz. This significant decrease in capacity at more extended ranges highlights the practical limitations of FSO communication under certain conditions, emphasizing the need for further research and development in this area to overcome these challenges.

These findings underscore the significant influence of visibility variation between Cape Town and Port Elizabeth on transmission range classification, ultimately affecting channel capacity. Port Elizabeth's higher visibility enables a more precise signal path, reducing attenuation and increasing capacity. In contrast, Cape Town's lower visibility can lead to increased signal degradation, reducing capacity. This implies that high visibility and optimized transmission range can enhance channel capacity, while lower visibility and longer ranges can decrease it. This underscores the importance of considering meteorological conditions in designing and deploying FSO systems, as they can significantly impact their performance and reliability. This research provides crucial insights that can inform and prepare the field for the challenges and opportunities in FSO communication.

Furthermore, this study contributes to the field of FSO communication by providing insights into the effectiveness of three modulation schemes within the South African coastal regions: binary phase shift, differential phase shift, and on-off keying. This research significantly enhances the research's applicability and potential impact on FSO communication by delving into the influence of meteorological parameters on the transmission path and the resulting changes in the refractive index.

TABLE OF CONTENTS

LIST OF FIGURES

LIST OF TABLES

LIST OF ABBREVIATIONS

ACC	Average Channel Capacity
AM	Amplitude Modulation
APD	Avalanche Photo Diodes
AWGN	Addictive white Gaussian noise
BER	Bit Error Rate
BPSK	Binary Phase Shift Keying
DPSK	Differential Phase Shift Keying
DQPSK	Differential Quadrature Phase Shift Keying
DTN	Delay Tolerant Networking
EDFA	Erbium-Doped Fiber Amplifier
FM	Frequency Modulation
FSO	Free Space Optics
FSOC	Free Space Optical Communication
FSOWC	Free Space Optical Wireless Communication
FTTH	Fiber to the Home
Gbps	Gigabits per Second
IEC	International Electrotechnical Commission
IR	Infrared
ITU	International Telecommunication Union
Nd:YAG	Neodymium Yttrium Aluminum Garnet
OOK	On/Off Keying
OWN	Optical Wireless Networking
PDF	Probability Density Function
PM	Phase Modulation
PPM	Pulse Position Modulation
RF	Radio Frequency

RISP	Refractive Index Structure Parameter
RMSE	Root Mean Square Error
SAWS	South African Weather Service
SDRT	Space Diversity Reception Technique
SDRT	Signal-to-Disturbance Ratio
SI	Scintillation Index
SIM-FSO	Sub-Carrier Intensity Modulation Free Space Optics
SOA	Semiconductor Optical Amplifier
SNR	Signal-Noise-Ratio
TCP	Transmission Control Protocol
UAVs	Unmanned Aerial Vehicles
VCSEL	Vertical Cavity Surface Emitting Laser
WDM	Wavelength Division Multiplexing

LIST OF SYMBOLS

τ_a	Absorptive transmittance
$\alpha_a(\lambda)$	Aerosol absorption coefficient
$\beta_m(\lambda)$	Aerosol scattering coefficient
α	Atmospheric large-scale scintillation
(λ, L)	Atmospheric transmittance
h	Altitude (m)
β	Atmospheric small-scale scintillation
R	Detector responsivity
f	Frequency
Υ_f	Fog attenuation factor
$\alpha_m(\lambda)$	Molecular absorption coefficient
K	Optical wave number
P_0	Radiated optical power
P_r	Received optical power
q	Particle size distribution
$p(I)$	Probability distribution function of I
L	Propagation link distance
$\beta_a(\lambda)$	Rayleigh scattering coefficient
I	Received optical intensity
C_n^2	Refractive index structure parameter ($m^{-2/3}$)
σ_R^2	Rytov variance
τ_s	Scattering transmittance
c	Speed of light
$\Upsilon_f(V)$	Specific atmospheric attenuation
$\Upsilon_T(\lambda)$	Total extinction coefficient
x	Transmitted signal
I_0	Turbulence free irradiance
A_0	Turbulence strength at the ground level
V	Visibility of the atmosphere

λ	Wavelength
v	Wind speed (m/s)

Chapter One Introduction

1.1 Background and Scope

Free Space Optical (FSO) communication is an innovative wireless system that harnesses light waves to transmit data through open space, revolutionizing telecommunications networking and wireless communication. With its lightning-fast speed, FSO offers a high-speed and reliable alternative to traditional radio frequency (RF) communication. It is a game-changing technology for various applications, including high-capacity data transfer in aerospace and terrestrial communication networks [1]. The potential of FSO is vast, promising a future of high-speed, reliable communication. However, it is not without its challenges. Random changes in atmospheric parameters [2], thermal expansion, earthquakes, and high-rise buildings [3] can all impact the propagating optical signal wave in FSO communication, highlighting urgent need for further research and development in this field.

The growing demand for bandwidth in mobile communication for large amounts of data drives research on data services and the application of new technologies, necessitating improvements in data transfer. The demand for efficient data transfer increases as the volume of data sent or received increases. In certain areas, there is a pressing need for faster and more reliable internet connectivity, which supports data rates of 256 kbit/s or higher. This scarcity hinders the ability to access online content, communicate, and utilize digital services, posing a significant challenge in the modern world [4]. Installing optical fibre lines in urban areas with developed infrastructures can be significantly costly [5, 6]. These regions strongly demand wireless internet services, where access to online resources is crucial, but traditional fiber optic connections are not readily available. Previous approaches, such as optical fibre and RF, have limitations, including high installation and maintenance costs and susceptibility to environmental factors; hence, cable-free technology like FSO has been developed.

Wireless communication has proven to be a reliable and effective solution when laying fibre optic cables is not feasible. This is particularly relevant in places of significant architectural value, spanning across roads and with international parks [7, 8], such as Kruger National Game Reserve, South Africa. The FSO system offers advantages in data transfer, such as a

cost-effective network design and deployment, reduced development costs, and maintenance flexibility on operating networks. These advantages, particularly the cost-effectiveness, set FSO apart from other communications systems. FSO technology can also be applied in disaster recovery, military communications, and remote sensing scenarios, demonstrating its versatility and potential.

The FSO system utilizes laser technology exclusively, operating at a designated wavelength of 800 nm, 900 nm, and 1.5 μm. These wavelengths interact with a wide range of atmospheric particles, including raindrops (0.1 mm - 10 mm), fog particles (1 m - 100 m in radius), snowflakes (up to 0.5 cm), and various aerosols such as sand, dust, and ash [9], which makes the FSO link less available and less effective [10]. The atmosphere functions as the medium for FSO communication. Attenuation from the atmosphere compromises the effectiveness of the system. Among various atmospheric influences, fog plays a crucial role, causing a reduction in FSO signal strength by up to 480 dB/km [11].

Previous studies in this field have mainly concentrated on utilizing gamma-gamma, log-normal, and K-distributions to model optical links. Despite the widespread use of these channel distributions for optical link modeling, researchers have found that they fail to adequately capture the complexity of real-world turbulence, leading to a significant mismatch between experimental and simulated data. Consequently, their applicability is restricted, and they must accurately predict performance across diverse turbulence conditions [12]. The generalized dual gamma model is a more comprehensive representation of irradiance, encompassing a wider range of turbulence conditions and outperforming the gamma-gamma and double Weibull channels in accuracy and applicability [13]. Therefore, to combat the impact of atmospheric turbulence and diverse weather conditions on signal quality at the receiving end, this research takes a comprehensive approach, implementing several strategies to minimize these effects and ensure reliable signal transmission. These include employing aperture averaging, choosing resilient modulation schemes, incorporating spatial, temporal, and frequency diversity, implementing channel coding, and utilizing adaptive optics [14, 15].

In the context of FSO communication systems, the most examined modulation and transmission strategy is subcarrier intensity modulation (SIM) combined with on/off keying (OOK). In [16], the authors looks at the error performance of FSO systems using various modulation schemes, transmitted over gamma-gamma channels, and subjected to diverse weather conditions and atmospheric turbulence regimes. Additionally, the study utilizes Meijer's - G function to derive a closed-form expression for the Bit Error Rate (BER), providing a mathematical framework for analyzing and evaluating the performance of FSO systems. Furthermore, [17] analyzes various mathematical techniques to assess the performance of FSO systems transmitting through gamma-gamma fading channels and the SIM Binary Phase Shift Keying (BPSK) scheme to determine the most effective analytical approach.

An adaptive optical system plays a pivotal role in extending the communication range, ensuring that any distortion in the optical signal can be effectively modified and coupled into the optical fiber at the receiving end. The primary objective of this study is to exploit the effectiveness of FSO link-based modulation schemes over FSO atmospheric channels while meeting the demands of larger channel capacity with a minimum BER. The accuracy and reliability of data transmission for the FSO links are characterized based on OOK, Differential Phase Shift Keying (DPSK), and BPSK schemes for FSO transmission over the atmosphere channels. It is crucial to note that the choice of modulation method significantly impacts the performance of the FSO links in terms of BER and channel capacity [18]. Therefore, a study through simulation of these various modulation schemes based on the FSO link performance would identify the best modulation scheme.

Apart from accomplishing a system that offers bandwidth efficiency, low BER, and strengthened security, the other constraints are based on link availability due to long-range communication. The FSO system operates based on a line of sight to transmit data wirelessly for computer networking and telecommunication [19]. Over long-range communication, the received signal quality can be degraded due to random fluctuations during transmission. Therefore, the factors that affect data transmission quality will be evaluated and modified to achieve a reliable system when analyzing the effectiveness of the FSO systems in South

Africa within the two coastal regions, namely Cape Town and Port Elizabeth which was officially renamed as Gqeberha on the 24th of February 2021.

This research has the potential to significantly enhance the reliability of FSO systems in the region. By observing and modifying network parameters, such as BER, signal-to-noise ratio (SNR), spectral efficiency, and receiver sensitivity, we can overcome the challenges associated with link failure for various weather conditions within these coastal regions.

1.2 Research Problem

The fundamental requirements for optimizing the performance of wireless telecommunication systems are based on achieving larger channel capacity, high transmission speeds, and a more excellent connection range with the lowest BER possible. The major challenge with FSO communication links is atmospheric turbulence, which degrades the system's performance. System link degradation occurs when the links experience a random fluctuation of air refractive index, which is caused by variations in the received optical intensity due to inhomogeneous changes in pressure and temperature [20]. These impairments can increase the bit error probability in the link, reducing the channel capacity and limiting the FSO system's reliability and availability. Furthermore, the system's performance can be degraded by other factors, such as atmospheric attenuation and geometric losses caused by scattering and absorption [21].

Based on the aforementioned factors, the proposed study can, therefore, deduce the following difficulties:

i. Issues on the performances and availability of FSO systems due to the effects of index inhomogeneities.
ii. The performance of the FSO links concerning BER and channel capacity is affected by various modulation methods.

However, the potential for optimization and the urgent need for investigating, implementing, and reporting on several mitigation techniques to overcome these challenges have been recognized in the literature. Through data and simulation analysis, the study proposes to shed light on the potential impact of different modulation techniques on the FSO link across the two coastal regions of South Africa.

1.3 Research Aim and Objectives

This section outlines the purpose, and goals of the research conducted in this study, stating the specific aims and objectives that guided the investigation.

1.3.1 Aim of the Research

This study aims to analyze and verify the feasibility of various modulation techniques based on FSO technology and review the link performance over SA coastal regions.

1.3.2 The Objectives of the Research

The objectives of this study are to:

i. Study the impact of weather conditions and atmospheric turbulence on laser beam propagation and link availability.

ii. Enhance the FSO's achieved transmission link performance and availability under different climate conditions and atmospheric turbulence within SA coastal regions.

iii. Achieve minimum BER with a high-quality signal between the transceiver components.

iv. Analyze the average channel capacity achieved by the identified modulation techniques.

1.4 Research Motivation

The motivation for this study is:

i. Demand for high-speed communication and increasing bandwidth requirement of present and emerging wireless communication systems.

ii. There is a high demand for internet access connectivity, leading to bandwidth demand on today's networks.

iii. Several applications and services that require larger bandwidth are launched through specific devices, namely smartphones, tablets, laptops, and desktops.

iv. However, telecommunication companies may no longer support these high bandwidth demands because they must compensate by investing in fiber cables for their backbone networks.

v. Compelling companies to rely on microwave RF links because of the challenges associated with laying cables to cities that have developed infrastructures (roads and buildings).

vi. Therefore, FSO can be used to provide backup links providing emergency links in the event of fiber optic cable failure and can also serve as a robust backbone infrastructure.

1.5 Limitations of the Study

This research is limited to exploring the effects of weather conditions within the specified regions, such as scintillation loss and fog visibility. The impact on FSO link reliability and strategies to overcome bad weather conditions are also considered. Thus, due to the complexity of the FSO study, there are certain limitations considered in this work, which are as follows:

i. Atmospheric conditions: The study focuses on analyzing weather conditions on FSO links by considering the following weather conditions only, namely fog visibility, relative humidity, temperature, and wind speed.

ii. Environmental conditions: FSO systems are susceptible to some environmental conditions such as foggy environment, path losses, and scintillation which can affect the performance metrics of modulation schemes.

iii. Analysis of data and simulation: This study is strictly based on data analysis and simulation and not experimental setup.

iv. Limited data: Due to the limited data availability, two years from 2018 and 2019 were considered.

v. Geographical scope: The study focuses on two coastal regions with different climate conditions which result in distinct fog characteristics that need to be addressed.

vi. Fog prediction and forecasting: The study explores fog prediction and forecasting methods, which are crucial for mitigating fog-induced attenuation.

vii. Mitigation strategies: The study investigates the modulation technique as a possible mitigation strategy considering only three modulation schemes (BPSK, DPSK, and OOK).

1.6 Thesis Structure

The dissertation is structured into six chapters, each addressing a specific aspect of the research, as summarized below:

Chapter One – Introduction: This chapter concisely overviews FSO systems, highlighting their principles and applications. It also emphasizes the significance of the research objectives and outlines the scope of the study.

Chapter Two – Literature Review: This chapter provides a comprehensive overview of FSO communication systems, delving into their fundamental characteristics, versatile applications, and typical system configurations. This review offers a solid foundation for understanding the technology's potential and limitations and highlights its practical implications in various fields.

Chapter Three – Research Methodology: This chapter introduces the study location and provides an overview of the statistical models utilized in this research. The use of Kim's model to predict the atmospheric attenuation and signal quality and the provision of the statistical channel model, mathematical parameters, and expression to derive the FSO system's performance metrics underscore this study's scientific rigor.

Chapter Four – Results and Discussion: This section investigates into the crucial relationships and patterns between visibility and parameters of the atmospheric phenomena (relative humidity, maximum temperature, and wind speed) for two years (2018-2019). The dataset is meticulously explored using graphical and regression analysis to identify monthly average visibility, maximum visibility, and standard deviation, unveiling significant trends and correlations between these variables.

Chapter Five – Link Performance Analysis: The visibility patterns were used to calculate and examine the atmospheric attenuation coefficients of physical layer FSO systems for South Africa's coastal regions. Attenuation losses caused by scattering and its effects are assessed, providing practical insights for system optimization. The system link availability based on visibility data is examined and discussed, offering valuable information for system

planning. Furthermore, the transmission schemes such as OOK, BPSK, and DPSK are evaluated and compared in terms of the critical performance matrices such as BER and average channel capacity achieved, guiding the selection of the most suitable transmission scheme for FSO systems.

Chapter Six – Conclusions and Recommendations: Subsequently, this chapter presents a comprehensive summary of the key findings, emphasizing the thoroughness and completeness of the results and findings.

1.7 Summary

This section provides a brief background and introduction to the study. It also outlines the aim and objectives, the motivation of the study, and its limitations.

Chapter Two Literature Review

2.1 Introduction

Optical Wireless Communication, known by designations such as FSO communication or Optical Wireless Networking (OWN), is a technique for transmitting data in which light functions as the communication medium. This technology permits data to be transmitted through the atmosphere by utilizing modulated light signals, typically found within the infrared or visible light spectrum.

The remainder of the chapter is organized as follows: Section 2.2 provides a complete description of the light and radiation spectrums. The study presents the selection of optical wavelength in the FSO communication system in Section 2.3, further discusses the limitations of the study in Section 2.4, introduces the application of optical wireless communication technology in Section 2.5, provides a brief overview of the FSO system transceiver in Section 2.6, provide an overview of atmospheric turbulence models in Section 2.7, discuss FSO mitigation techniques in Section 2.8, and cover the summary of the chapter in Section 2.9.

2.2 Spectrum of Light and Radiation

The optical bandwidth is the span of frequencies employed in optical communication setups, which are categorized into distinct segments. Presently, a large portion of optical systems function within the short-wave infrared range (780 nm to 850 nm). This is mainly attributed to the cost benefits and the ready availability of dependable semiconductor laser diode sources within this wavelength interval [22].

Figure 2.1 displays the spectrum of light and radiation, which can be characterized by its wavelength and energy pulse rate. The frequency (f) and wavelength (λ) are inversely related, with a specific mathematical equation connection as shown in (2.1), illustrating the spectrum's versatility in description. The greater frequency corresponds to the greater energy [23].

$$\lambda = \frac{c}{f} \tag{2.1}$$

where c is the symbol of the speed of light (2.998 x 10^8 m/s) and within the wavelength range of 780 nm to 1600 nm, there exist multiple transmission windows characterized by

their near transparency (attenuation < 0.2 dB/km). These transparent windows are centered around specific wavelengths [24, 25]. These will be discussed in the subsequent section.

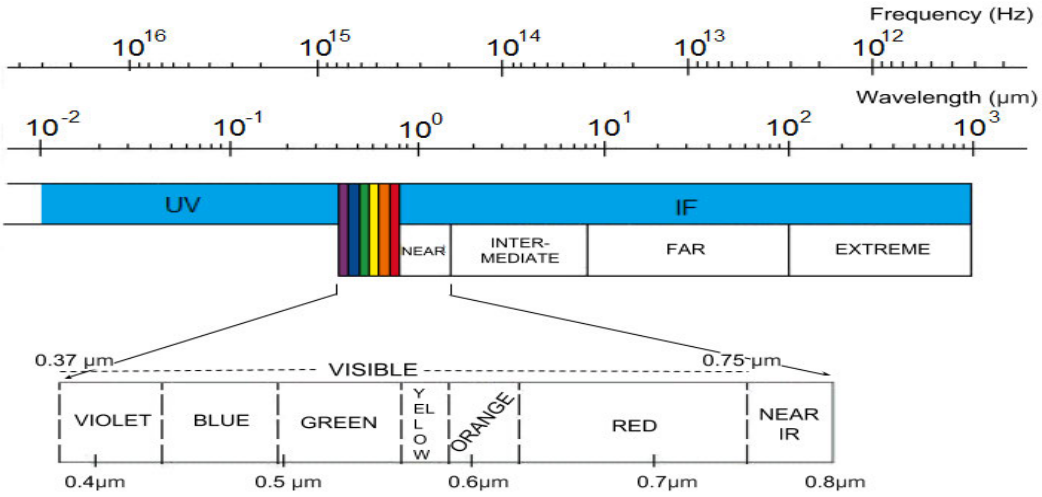

Figure 2.1 Electromagnetic spectrum [22].

The 850 nm wavelength range is appropriate for FSO operations [24, 25]. Furthermore, dependable, high-capacity, and cost-effective transmitter and sensor elements are widely accessible and frequently utilized in contemporary service provider networks and transmission apparatus. Cutting-edge technologies such as the advanced Vertical Cavity Surface Emitting Laser (VCSEL) technology and silicon Avalanche Photodiode (APD) with heightened sensitivity could be exploited to function within this specific atmospheric range.

The 1060 nm transmission window demonstrates significant minimal signal loss [26]. Nonetheless, the availability of transmission elements for constructing FSO systems within this wavelength range is restricted, and these components tend to be bulky, exemplified by solid-state lasers such as Neodymium Yttrium Aluminum Garnet (Nd: YAG) laser [27]. The limited demand for these components in wireless communication systems has resulted in a scarcity of optimal data transmission components, making them difficult to procure. Laser diodes with a wavelength of 980 nm, commonly used in fiber optic amplifiers, can be readily purchased from commercial suppliers. Nevertheless, the 980 nm wavelength band is prone to considerable atmospheric attenuation, leading to signal degradation of several dB/km, even in fair weather conditions.

The transmission range of 1250 nm provides minimal signal loss, yet transmitters within this wavelength range are uncommon. Commercially accessible are telecommunications-grade lasers with lower power that generally operate between 1280 nm and 1310 nm. Despite the potential of the 1290 nm wavelength, its suitability for atmospheric transmission is limited due to a substantial increase in atmospheric attenuation, leading to notable signal degradation.

Additionally, the 1550 nm wavelength range is highly suitable for transmitting through atmospheric space due to its minimal signal loss and abundant of top-notch transmitter and sensor elements. The ideally suited transmission wavelength is 1550 nm for atmospheric transmission, offering optimized signal fidelity and minimal signal loss, combined with the availability of high-performance transmitters and sensors. These components encompass rapid semiconductor laser technology suitable for Wavelength Division Multiplexing (WDM) functionality, along with amplifiers such as Erbium-Doped Fiber Amplifiers (EDFA) and Semiconductor Optical Amplifier (SOA) designed to enhance transmission power. Given the favourable attenuation characteristics and the availability of components within this range, creating WDM-free space optical systems to be is achievable.

2.3 Selection of Optical Wavelengths in FSO Communication Systems

For FSO applications, one of the critical design factors that is crucial for FSO communication systems is the choice of wavelength. This decision significantly impacts both the optical link's performance and the detector's sensitivity. Transmitting at shorter wavelengths offers a significant advantage, as the antenna's gain increases inversely with the operating wavelength, resulting in improved signal strength and directionality. However, utilizing higher wavelengths between 1330 nm and 1500 nm can mitigate the impact of pointing errors on signal strength, resulting in improved optical link quality and reduced signal fade [28]. Optimizing the wavelength is crucial when designing an FSO link, as it directly impacts system performance. Careful tuning of the wavelength is essential to achieve the best possible results, balancing the trade-offs between signal strength, antenna gain, and atmospheric interference. The choice of wavelength is heavily influenced by atmospheric conditions, attenuation, and background noise power, all of which play a significant role. Besides, in designing an FSO system, various factors, including compliance

with eye safety regulations, the availability of transmitter and receiver components, and the cost of optical units, all play a significant role in determining the optimal wavelength. The International Commission on Illumination (CIE) has categorized optical radiations into three distinct groups [29] as seen in Table 2.1:

Table 2.1 The categorization system established by the CIE [29].

Type	Wavelength	Photon energy (THz)
IR A (Near IR)	0.7 μm–1.4 μm (700 nm–1400 nm)	215–430
IR B (Mid-IR)	1.4 μm–3.0 μm (1400 nm–3000 nm)	100–215
IR C (Far-IR)	3.0 μm–100 μm (3000 nm– 0.1 mm)	3–100

2.4 Limitations of FSO

FSO communication is a technology that employs light to convey data through the atmosphere, usually covering relatively short distances and eliminating the requirement for physical cables or fibers. The atmospheric channel pertains to the pathway through which the optical signal moves, encompassing the influence of the atmosphere on signal transmission. Atmospheric conditions can notably influence the performance of FSO systems; that is, they are predominantly influenced by the climatic and physical attributes of their installation site [30], as indicated by Figure 2.2.

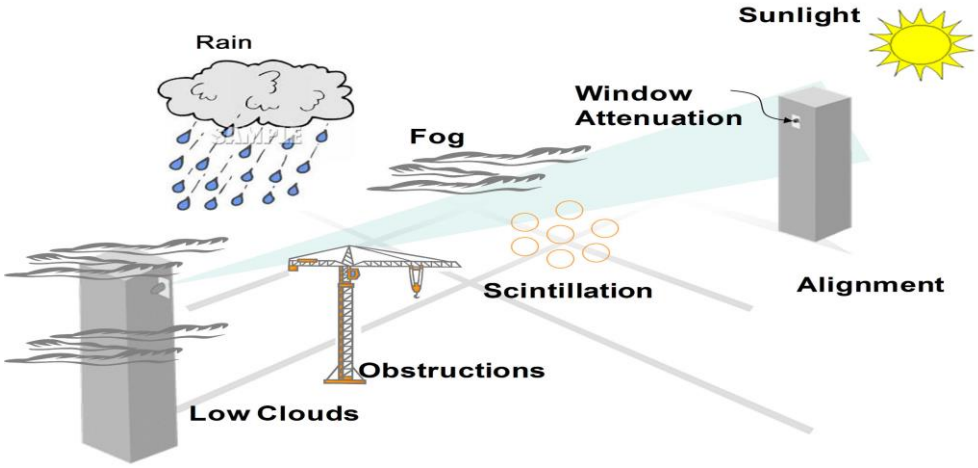

Figure 2.2 Different physical and weather conditions affecting FSO link [31].

The following is a breakdown of how the atmosphere affects signal loss in FSO communication [23]:

i. Absorption: Various molecules present in the atmosphere, including water vapour and oxygen, can absorb specific light wavelengths. This absorption phenomenon can decrease the intensity of the signal as the light traverses through the atmosphere.

ii. Scattering: Scattering takes place when light engages with small particles within the atmosphere, leading to alterations in its trajectory. This process can result in the dispersion of light and a subsequent reduction in signal strength upon reaching the receiver. The type of scattering that occurs is determined by the following conditions [32]:

   a. If the object is smaller than the wavelength, it results in Rayleigh scattering.
   b. When the object's size is like the wavelength, it leads to Mie scattering.
   c. If the object is significantly larger than the wavelength, it causes nonselective scattering.

iii. Turbulence: Atmospheric turbulence, triggered by fluctuations in air temperatures and wind patterns, can induce changes in the refractive index of air. Consequently, the optical beam becomes distorted, which in turn causes signal fading and degradation.

iv. Refraction: Temperature gradients leading to alterations in air density cause light to bend or refract when it traverses distinct atmospheric layers. This phenomenon can result in the displacement of the optical beam and subsequent signal attenuation.

v. Attenuation: Attenuation pertains to the gradual weakening of signal intensity during light propagation through the atmosphere. This phenomenon primarily arises from the combined effects of absorption and scattering. Atmospheric attenuation can be categorized into three types [33]:

   a. Rayleigh scattering (molecular scattering).
   b. Mie scattering (aerosol scattering).
   c. Nonselective scattering (geometric scattering).

vi. Weather Conditions: Unfavourable weather situations like rain, snow, fog, and smog can exacerbate the deterioration of FSO signal quality. Water droplets and airborne

particles have the potential to disperse and absorb light, resulting in increased channel losses.

vii. Link Distance: Extended FSO connections are more vulnerable to atmospheric losses due to the heightened interaction between the signal and atmospheric elements across the greater distance, and physical obstruction along the path.

2.5 Applications of Optical Wireless Communication Technology

The FSO communication link, a versatile technology that uses modulated light to transmit data through the air, is employed across various locations and for multiple services. Its versatility is evident in the diverse range of applications, including:

i. Last-Mile Connectivity: Most buildings are linked through coaxial and fiber optic cables. However, many end-users do not have access to optical fiber infrastructure, such as Fiber to the Home (FTTH). FSO communication emerges as a crucial solution for connecting remote end-users, especially those in rural areas, offering high-speed connections in the Gigabits per Second (Gbps) range over extensive distances. The thrill of high-speed connections in the Gigabits per Seconds (Gbps) range over extensive distances is a crucial feature of FSO, sparking excitement about its performance. FSO can swiftly provide service to existing fiber optic users when their current fiber connections are disrupted. Furthermore, FSO technology enables broadband internet services in remote and challenging-to-reach areas where traditional access technologies struggle to establish connectivity [34].

ii. Outdoor Wireless Service: This term refers to the provision of wireless communication services in outdoor environments. Wireless service providers can utilize FSO for communication purposes, and unlike microwave bands, a license is not needed to operate FSO [32].

iii. Unmanned Area Vehicle (UAV): A UAV, or drone is an aircraft without a human polit on board. Lately, there has been a notable rise in the utilization of drones across various commercial and military sectors. These applications involve distant observation, surveillance, data transmission, supervision, and protection. The increasing use of networked aerial platforms is mainly due to their ability to adapt

and expand quickly. Leveraging the benefits of FSO technology, UAVs equipped with FSO systems provide efficient solutions for the data transmission needs of various networks, including front-haul and back-haul applications [35].

iv. Military and Defence: Military applications include secure communication, surveillance, reconnaissance, and UAVs for intelligence gathering and tactical operations. FSO technology has applications in secure military communication, reconnaissance, and surveillance. Due to the narrow beam divergence, its resistance to jamming and eavesdropping, as the beam is difficult to intercept without physical access to the transmission path, is particularly advantageous for military operations [36].

v. Security: FSO communication is inherently secure, offering a high level of reassurance. Its resistance to interception, due to the difficulty of accessing the laser beam transmission path, makes it an appealing choice for secure military communications, financial institutions, and confidential data transfer. This inherent security feature of FSO technology provides a strong sense of reliability and reassurance [37].

vi. Backhaul: FSO can be used for wireless backhaul, connecting cellular base stations and Wi-Fi hotspots to the core network. It offers high capacity and low latency, improving the performance of wireless networks [38].

2.6 FSO System Transceiver

The three essential elements of a fixed FSO communication system are the transmitter, which encodes and transmits the data; the free space channel, the optical link through which the signal propagates; and the receiver, a crucial component that captures and decodes the signal. These main components can be further dissected into numerous constituent parts [23], as depicted in the transceiver block diagram for a Free Space Optical Wireless (FSOWC) communication system in Figure 2.3. Information waveforms within the transmitter are generated by a source, which is subsequently impressed onto a laser carrier through modulation. The resulting laser field is emitted into the atmospheric channel, traversing the distance to the intended receiver. Subsequently, the optical signal gathered by the receiver

undergoes conversion into an electrical current using a photodetector. This received current is then processed to retrieve the initial transmitted data [26]. Nonetheless, the received data might not perfectly match the initially transmitted information due to signal attenuation during transmission through the channel. This aspect needs to be revised considerably to maintain the effectiveness of wireless communication systems.

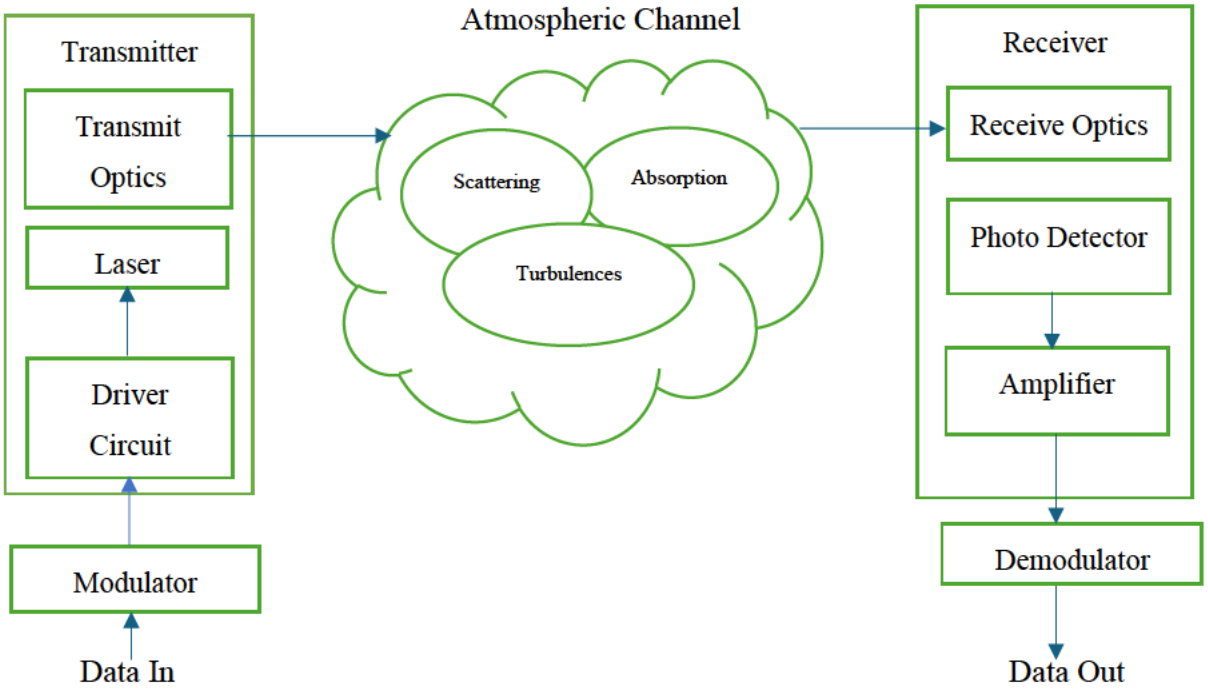

Figure 2.3 FSOWC Transceiver System Block Diagram [39].

2.6.1 The Transmitter

The transmitter sends data signals through free space via the modulation of optical radiation. Its fundamental constituents include a radiation source, a laser modulator, and various optical devices [40]. The laser modulator achieves optical signal modulation by manipulating an electrical signal, often by adjusting parameters like the laser biasing current. One commonly utilized optical components is the telescope, which is used to orient optical radiation toward the receiver.

Therefore, the transmitter within the FSO system configuration assumes a critical function in producing and forming the optical signal, which is intended for transmission across the

atmosphere. Recent significant advancements in FSO transmitter technology have resulted in improved functionality and flexibility, shaping the future of FSO communication systems:

i. High-Power Laser Source: A crucial element of the FSO transmitter is an exceedingly powerful laser source responsible for delivering the optical carrier signal. Noteworthy progressions in laser technology have witnessed the utilization of semiconductor-based lasers with elevated output power and spectral integrity. A prime example is the implementation of diode-pumped solid-state lasers and Vertical-Cavity Surface-Emitting Lasers (VCSELs), which have exhibited potential in FSO applications [41].

ii. Wavelength Agility: Recent FSO transmitters' adaptability to diverse atmospheric conditions and modulation schemes using wavelength-agile capabilities is a promising development. This feature allows for optimal wavelengths, effectively mitigating the detrimental consequences of atmospheric absorption and scattering. It instils optimism about the future adaptability of FSO transmitters [28].

iii. Advanced Beam Shaping: Recent studies have emphasized sophisticated methods of shaping beams to enhance the efficiency of transmitting optical beams in FSO systems. These methods, including adaptive optics, diffractive optical elements, and beam collimation optics, play a crucial role in augmenting beam quality and sustaining a narrow beam divergence. This emphasis on advanced beam shaping reassures the audience about the performance of FSO systems [42].

2.6.2 The Free Space Channel

The laser signal traveling through the atmosphere from the transmitter will experience scattering, absorption, or fluctuations in irradiance based on the prevailing atmospheric conditions in a specific layer or area. Thus, leading to reduced signal quality and reliability. These conditions include haze, low clouds, turbulence, rain, smoke, dust particles, snow, and fog [43]. However, atmospheric turbulence and fog are the most significant contributors to losses in FSO communication links caused by atmospheric conditions, surpassing other factors [44]. These conditions can reduce signal quality and reliability, posing significant challenges in FSO communication. Within FSO communication systems, the main

impairments throughout the traversing of laser signals stem from atmospheric absorption and scattering, especially in the absence of scintillations. These impairments arise due to the inevitable interaction between the propagating optical beam and the atmosphere, which contains various airborne particles (aerosols) of different types and shapes in varying concentrations at any given time.

The interaction between light and the atmosphere is a quantum mechanical process. The efficiency of atmospheric absorption is strongly wavelength-dependent, meaning its impact varies significantly depending on the specific wavelength of transmitted light. The absorption process occurs when a photon of light is absorbed and annihilated by tiny amounts of atmospheric gases, effectively eliminating it from the transmission [45].

The energy from photons is transferred into gas molecules, which gain kinetic energy and start vibrating faster, effectively converting light energy into thermal energy. This phenomenon underlies the random warming of the Earth's atmosphere, contributing to its thermal energy. When absorption is negligible, choosing the right wavelength window is crucial to reduce absorption to the lowest possible level. Thus, absorption losses can be safely neglected without significantly impacting the practical outcomes, as their effects are negligible.

Consequently, gas molecules absorbing photon energy increase their kinetic energy. This process is fundamental of atmospheric physics and is crucial in shaping our planet's climate and weather patterns. When absorption has a minimal impact, selecting a specific wavelength range with care is essential to reduce further absorption to the lowest possible level [46]. In practical applications, absorption losses can be disregarded without any substantial impact. Choosing wavelengths with high transmittance in the absorption spectrum can effectively mitigate the absorption effect, resulting in minimal signal degradation and optimal transmission performance [23]. Figure 2.4 is a typical overview of the atmospheric transmittance window with absorption contribution

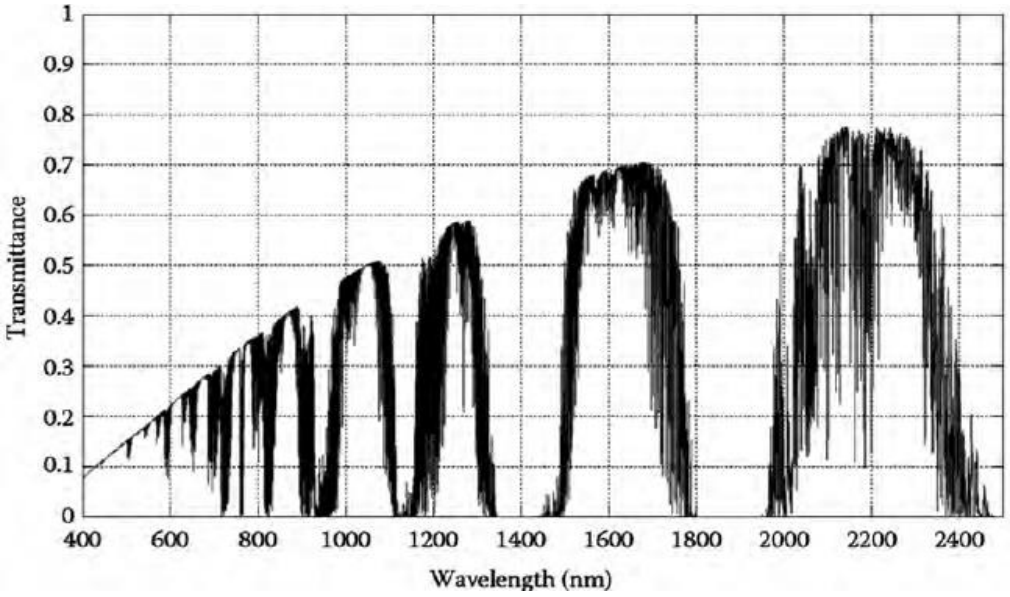

Figure 2.4. Atmospheric transmittance window with absorption contribution [26].

2.6.3 The Receiver

In this process, the original information signal is extracted from the received optical radiation. This is accomplished by collecting and focusing the incoming optical beam onto a photodetector using an optical bandpass filter. The filter's selective allowance of only the desired wavelengths effectively recovers the transmitted signal. More importantly, the optical bandpass filter plays a crucial role in reducing background noise, as it filters out unwanted signals, ensuring the system's performance is not compromised. As the aperture of the receiving telescope expands, it enhances the ability to collect diverse incoming optical beams. Nevertheless, this increase in aperture size also leads to a more significant influx of background noise, potentially degrading the SNR. The filtered output is then sent to the photodetector, which converts the optical signals into electrical signals [47].

The receiver's terminal can utilize two primary optical receivers: non-coherent and coherent. Non-coherent receivers directly measure the instantaneous power of the received signal without analyzing the phase component, enabling simple and efficient signal detection. In contrast, a coherent receiver employs a more sophisticated approach, where a locally generated light wave field is optically mixed with the received field, resulting in an integrated wave. This combined wave is then subjected to photodetection, enabling the

receiver to extract amplitude and phase information from the signal. These receiver types are suitable for use when data is encoded onto the optical carrier wave using various modulation techniques, such as Phase Modulation (PM), Frequency Modulation (FM), or Amplitude Modulation (AM), which alter the phase, frequency, or amplitude of the light wave to convey data. At the receiver end, Avalanche Photo Diodes (APDs) and PIN diodes are widely used, with APDs being the preferred choice for photodetection due to their high sensitivity and gain [47]. The post-detection processor, also known as the decision circuit, is a crucial component that amplifies, filters, and processes the electrical signal produced by the photodetector. Its role is paramount in extracting the original information signal from the sender, ultimately recovering the transmitted data and ensuring the system's efficiency.

2.7 Atmospheric Turbulence Models

Different statistical models have been applied to describe atmospheric turbulence along FSO links. The log-normal model represents weak turbulence conditions at distances less than 1 km. For more intense turbulence spanning several kilometers, models such as the negative exponential and K-distribution have been suggested [48, 49]. The versatile gamma-gamma distribution model is commonly used to represent turbulence across a spectrum of intensity, from weak to intense conditions, and is recognized as a multiplicative random process [50]. One of the fundamental tasks in addressing mitigation techniques to achieve the effectiveness of optical communication systems is the precise representation of atmospheric turbulence across various scenarios. Several irradiance functions using probability distribution functions are described in the following section.

2.7.1 Lognormal distribution model

The lognormal distribution is extensively utilized to describe the characteristics of weak atmospheric instability. In this context, concerning the received irradiance I at the receiver the probability density function (PDF) adheres to the lognormal distribution as seen in equation (2.2) [51]:

$$f_I(I) = \frac{1}{2I\sqrt{2\pi\sigma_I^2}} \exp\left(-\frac{(ln\,(I)+2\sigma_I)^2}{8\sigma_I^2}\right) \tag{2.2}$$

whereby $\sigma_I^2 \approx \sigma_I^2/4$, illustrates the variability in log amplitude (signal strength) for both spherical waves and plane waves, formulated by equations (2.3) and (2.4), consequently [26]:

$$\sigma_I^2|_{sphercal} = 0.124 \times K^{7/6} \times C_n^2 \times L^{11/6}, \tag{2.3}$$

$$\sigma_I^2|_{plane} = 0.31 \times K^{7/6} \times C_n^2 \times L^{11/6}, \tag{2.4}$$

where σ_I^2 is Rytov variance then $K = \frac{2\pi}{\lambda}$ is the optical wave number (m^{-1}), λ is the operating optical wavelength, the optical transmission link has a constant value of C_n^2 as the Refractive Index structure Parameter (RISP) ($m^{-2/3}$) during weak turbulence, remaining less than unity [52], and L is the propagation link distance (m).

2.7.2 Negative exponential distribution

The negative exponential turbulence model is utilized to describe saturated turbulence scenarios. A considerable abundance of independent scatterings in this model contributes to the establishing of the saturation regime. Consequently, the fluctuations in irradiance adhere to the Rayleigh distribution [53], producing negative exponential statistics for the irradiance. The PDF of the negative exponential with the mean received irradiance I_0, can be mathematically expressed [54] as shown in equation (2.5):

$$f(I) = \frac{1}{I_0} \exp\left(-\frac{I}{I_0}\right), \; I_0 > 0 \tag{2.5}$$

where $E[I] = I_0$ is the mean received optical irradiance and I is the radiance.

2.7.3 K-distribution

The K-distribution turbulence model is commonly applied to characterize intense atmospheric turbulence situations (non-Rayleigh Sea clutter) [55]. Furthermore, the K-distribution can be represented as the product of an Exponential distribution and a Gamma distribution, implying that the K-distribution can be decomposed into two independent components, each characterized by a distinct distribution [56]. In the case of the K-distribution atmospheric turbulence model, the PDF $f(I)$ is formulated in equation (2.6):

$$f(I) = \frac{2\alpha}{\Gamma(\alpha)}(\alpha I)^{\frac{\alpha-1}{2}} K_{\alpha-1}\left(2\sqrt{\alpha I}\right), I > 0, \alpha > 0 \quad (2.6)$$

where $\Gamma(.)$ is the gamma-gamma function, then $K_{(\alpha-1)}$ is the nth-order modified Bessel function of the second kind and order $\alpha - 1$. The parameter α is often interpreted as a measure of the number of significant scatterers that contribute to the scattering process.

2.7.4 Gamma-Gamma Turbulence Model

The gamma-gamma model [57] is extensively utilized in the literature related to FSO communication due to its versatility in addressing a broader spectrum of turbulence conditions. When contrasted with actual observations, the gamma-gamma distribution is adept at portraying atmospheric turbulence conditions spanning from weak to strong. The PDF is thus represented in [58] as (2.7):

$$f(I) = \frac{2(\alpha\beta)^{(\alpha+\beta)/2}}{\Gamma(\alpha)\Gamma(\beta)} I^{\frac{\alpha+\beta}{2}-1} K_{(\alpha-\beta)}(2\sqrt{\alpha\beta I}\,,\ I > 0 \quad (2.7)$$

whereby, $\Gamma(\cdot)$ represents the gamma function, I denotes the intensity of the signal, $K_{(\alpha-\beta)}$ is the modified Bessel function of the second kind order $(\alpha - \beta)$, α and β parameterize the effective number of eddies in the turbulent flow with a focus on large and small-scale components of turbulence [59] defining the scintillation parameters, respectively.

2.8 FSO Mitigation Techniques

While posing challenges, the atmospheric channel also presents opportunities for the FSO system to demonstrate its adaptability. The decline in the received signal's quality, which compromises the FSO system BER performance and increases the likelihood of data transmission errors, can be mitigated. A range of mitigation methods can be implemented to enhance the effectiveness and dependability of the FSO system across diverse environmental situations. These techniques, which can be applied at the physical or different layers of the Transmission Control Protocol (TCP), ensure optimal performance and underscore the resilience of the FSO system.

Many methods are employed at the physical layer to address challenges in the FSO system. These include hybrid RF/FSO links, relay transmission, aperture averaging, diversity, modulation, adaptive optics, coding, background noise rejection, and jitter isolation.

Similarly, methods within the TCP layer involve data retransmission, reconfiguration, rerouting, and quality of service control [60]. Figure 2.5 provides an overview of various methods for mitigating atmospheric turbulence. This research focuses explicitly on modulation and coding techniques.

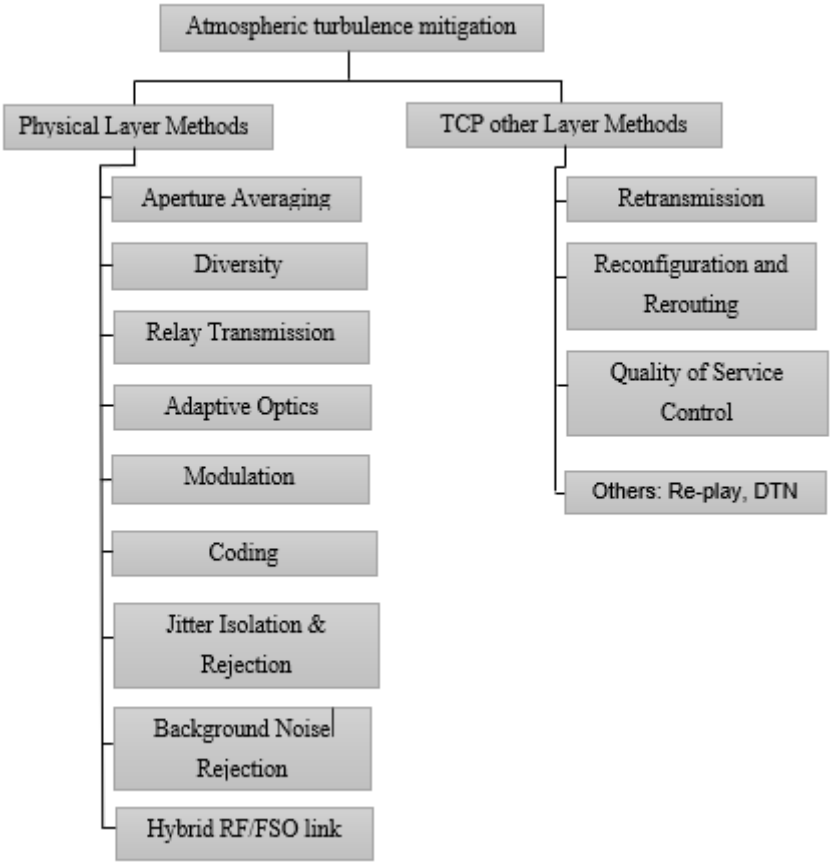

Figure 2.5. Atmospheric turbulence mitigation technique [26, 28].

2.8.1 Modulation and Coding

Regarding FSO communication, the selection of modulation and coding techniques is influenced by two primary factors: optimizing optical power and maximizing bandwidth utilization. Optical power efficiency is determined by comparing the optical power gain achieved with OOK, assuming both modulation methods share the same Euclidean distance, denoted as d_{min}. Transmission schemes that prioritize power efficiency are straightforward to implement and show notable efficacy in counteracting turbulence effects, especially at lower data rates. Nonetheless, these schemes must adhere to safety regulations to protect the

human eye, which restricts their range during periods of high turbulence. On the contrary, bandwidth efficiency dictates the utmost data capacity attainable for a given link length using a specific modulation scheme [28].

Ongoing research endeavours aim to address the limitations of Free Space Optical Communication (FSOC) and boost its effectiveness through applying modulation techniques and aperture averaging. These research activities are diligently working to investigate innovative approaches, methodologies, and protocols to counter FSOC's constraints and are broadly categorized in [36] through the following areas:

i. Modulation Techniques: Extensive research has been conducted on various modulation methods in atmospheric turbulence scenarios. These include Q-ary Pulse Position Modulation (PPM), Subcarrier BPSK, and OOK. The findings [61] have equivocally established BPSK as the superior choice among these options, underscoring its significance in the field.

ii. Space Diversity Reception Technique (SDRT): This minimizes the deterioration of transmission quality caused by robust atmospheric turbulence interference. When comparing Differential Quadrature Phase Shift Keying (DQPSK), DPSK, and OOK, both DPSK and OOK exhibit significant improvements in Signal-to-Disturbance Ratio (SDRT) [62].

iii. Scintillation Mitigation by Modulation: OOK represents the most straightforward implementation and partially addresses scintillation issues. DPSK modulation can effectively mitigate the impact of scintillation and provides twice the spectral efficiency compared to both DPSK and OOK [36].

iv. Pointing Error: Expanding the beam’s diameter can alleviate PE resulting from buildings’ swaying motion [63].

v. Scintillation Mitigation: The method of aperture averaging, and adaptive adjustment of the receiver diameter effectively mitigates fluctuations in intensity and the deterioration of received light in FSOC caused by atmospheric turbulence [64, 65].

2.9 Summary

This chapter briefly overviews the laser and electromagnetic spectrum used to transmit modulated light signals through the atmosphere, this includes the wavelength selection. It also revised the various challenges, such as obstacles the laser beam faces as it passes through the Earth's atmosphere. The FSOWC transceiver system block diagram layout, detailing each subsystem, is further discussed. Mathematical models for specific atmospheric turbulence models are provided, but some techniques used to mitigate these effects in FSO communication systems must be considered.

Chapter Three Research Methodology

3.1 Introduction

This section presents the methodology employed in this study to investigate the feasibility of various modulation techniques for the FSO technology under atmospheric turbulence and weather conditions. The FSO link performance is evaluated based on two selected coastal locations in South Africa; namely Port Elizabeth, and Cape Town. The study focused on the coastal regions due to their status as a popular tourist destination, where the FSO system can facilitate the enhancement of tourism infrastructure, including high-speed internet access. The research used data collection methods and data analysis techniques to achieve the objectives of this study. Also, the research is grounded in statistical analysis and a graphical representation. It exploits tools such as PDF to model atmospheric turbulence over gamma-gamma distribution channels and mathematical tools such as Meijer-G Function to derive meaningful insights from the dataset. The gamma-gamma distribution channel was selected for this study due to its numerous benefits, including its ability to cover all turbulence conditions, accuracy in modelling, and flexibility, which are not present in other distribution channels. Furthermore, this study evaluates the influence of atmospheric transmission on optical signals within the selected study areas under various conditions, including different visibility patterns and turbulence strengths. Through the analysis of climatic data, this study seeks to uncover the precise impacts of atmospheric instability on laser signal transmission, including the resulting attenuation patterns and changes, and to examine these phenomena in a detailed and comprehensive manner. This will provide valuable insights into the challenges and limitations of optical communication in these locations.

This chapter is organized as follows: Section 3.2 provides an overview of atmospheric parameters, Section 3.3 reviews South African coastal climates, Section 3.4 discusses the laser system and channel modelling, Section 3.5 presents the FSO atmospheric channel loss, Section 3.6 addresses scattering attenuation, and Section 3.7 provides information on turbulence-induced signal attenuation. The subject of turbulence modelling is then presented in Section 3.8, followed by a chapter summary in Section 3.9.

.

3.2 Overview of Atmospheric Parameters

The knowledge of atmospheric parameters is crucial for the communication system's performance with FSO inclusive. These parameters usually vary per time and locations and thereby play a vital role in shaping the system's behaviour and determining its overall performance. In this study, the following parameters were analyzed and assessed to achieve results.

i. Visibility is one of the meteorological parameters which indicates the distance at which light of an object can be seen. It is measured in *km.*

ii. Wind Speed is the velocity of air movement. It is measured in *km/h.*

iii. Humidity: Expressed as a percentage, it indicates the amount of moisture in the air.

iv. Temperature: Measured in degrees Celsius (°C), it represents the air temperature.

v. Turbulence: Refers to the irregular fluctuations in wind speed and direction, that affect the stability of the atmosphere.

3.3 Review of Coastal Climates in South Africa

South African coastal regions usually experience different climatic seasons, which are autumn, winter, spring and summer that occurs between mid-February and April, May and July, August and mid-October, and finally between mid-October and mid-February, respectively. The two coastal cities selected for this study were well-known as adventurous, attractive and densely populated, where the use of high data transfer technology is crucial. The cities were Cape Town and Port Elizabeth. The climate data gathered from these cities weather stations serves a specific purpose in this study. They are used to explore and predict the attenuation of the transmitted optical signals because of the instability of the atmospheric and diverse weather conditions, examining the impact on various transmission schemes. Furthermore, it examines the optical link availability in various cities under different atmospheric conditions from each city. Therefore, this analysis and collection of data efforts are undertaken specifically to assess the effects of signal attenuations in diverse atmospheric conditions. Hourly readings of different weather patterns such as visibility, wind speed, temperature, and humidity levels were gathered for the two coastal regions over two years (2018-2019) from the South African Weather Service (SAWS) database. This study converted hourly fog visual range data from local climate records into three-hour synoptic

hour intervals and applied these transformed data to estimate optical signal attenuation at a specific wavelength, enabling the estimation of signal weakening due to fog conditions.

The climate and geographical coordinates of the two cities differ, their features and descriptions are summarized in Table 3.1 and Figure 3.1 is the South African geographic map highlighting the study locations.

Table 3.1 Features of the Study Locations

Site	Province	Latitude (S)	Longitude (E)	Climate Condition	Elevation (m)
Cape Town	Western Cape	33° 58'	18° 36'	Mediterranean	42
Port Elizabeth	Eastern Cape	33° 57′	25° 36′	Moderate oceanic	85

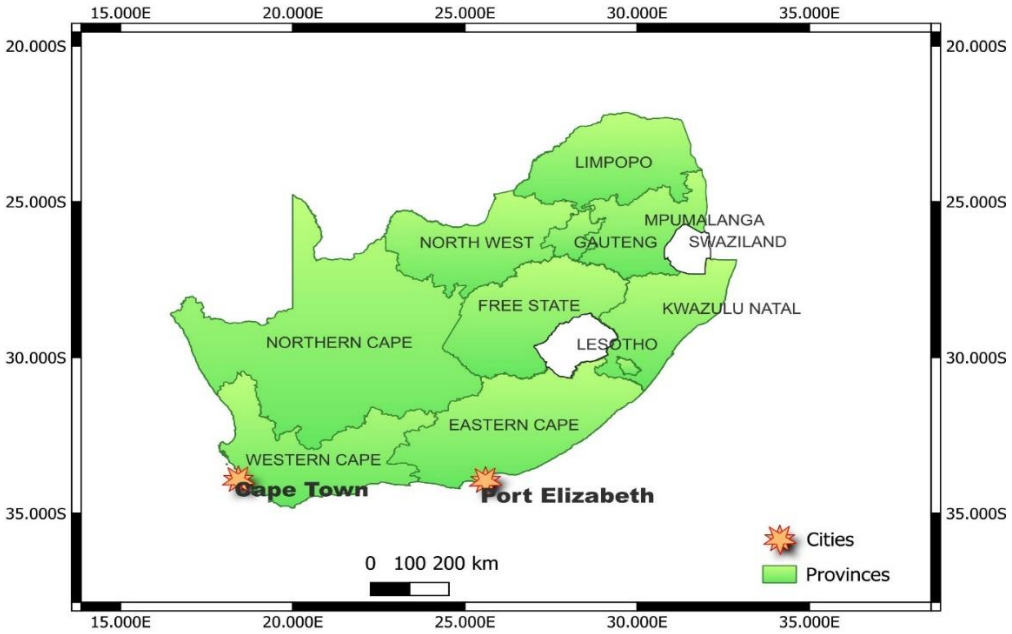

Figure 3.1 Map of SA topology highlighting the location of the study.

3.4 Laser System and Channel Modelling

Considering a simulation of an FSO link employing SIM-OOK modulation, at the transmission end, the information is encoded onto the optical beam by modulating its intensity in real-time. The optical power transmitted from the sender's aperture into free space is subject to degradation due to various factors, including misalignment-induced signal

loss, atmospheric turbulence-caused fading, and background noise, before it reaches the receiver's aperture, affecting the signal's strength and quality. These factors result in variations in the signal's intensity [66], the APDs convert the received laser beam signal into an electrical signal, y, at the receiving aperture, effectively detecting and retrieving the signal [17] as in equation (3.1).

$$y = IRx + n \tag{3.1}$$

where I is the magnitude of the optical signal that is detected at the receiver, which is also defined as the channel state in [67], the transmitted signal is represented by x, the photodiode detector has a responsivity of R, and n is a random variable representing AWGN with a zero mean and a variance of (σ_n^2), distributed as $\sim\mathbb{N}(0, \sigma_n^2)$ [68]. Channel state is characterized by atmospheric turbulence, weather conditions, and pointing errors, and these factors are independent, therefore $I = I_l + I_a + I_p$. Where I_a accounts for the fading losses resulting from atmospheric turbulence, I_l represents the fixed loss factor of the atmospheric channel which is dependent on weather conditions and a link distance [69]. I_p accounts for the losses incurred due to inaccurate pointing and geometric spread, which occurs when the transmitter and receiver are not perfectly aligned, and the beam diverges over distance [67]. However, this research focuses solely on the atmospheric attenuation loss or path loss, which is affected by scintillation resulting from atmospheric turbulence and diverse weather conditions like fog, neglecting other potential sources of loss. Therefore, $I = I_l + I_a$.

3.5 FSO Atmospheric Channel Loss

During the laser beam's atmospheric transmission, the beam interacts with the air molecules and aerosols, producing atmospheric attenuation. When the optical signal is attenuated, the propagation path distance has an exponential decay relation with the laser beam power [70], and the optical signal's power and intensity deteriorate as it traverses through the channel [71]. Fog is the main contributing factor amongst other atmospheric attenuation that severely affects an optical signal because of fog particles comparable to the optical transmission wavelength [19], thus, fog attenuation results in scattering and absorption [72].

The attenuation may rise to more than 350 dB/km when the visibility is less than 50 m. To mitigate this situation, considering a powerful laser must include special procedures to

enhance communication [73]. For a reasonable data rate, lasers with high radiating power operating at a 1550 nm transmission wavelength are the most preferred choice under dense fog conditions [74]. Transmittance measures how much optical power is preserved as it travels a certain distance through the atmosphere, calculated by comparing the initial power (P_o) to the received power (P_r). Beer-Lambert law formulates the optical transmittance of light in the atmosphere [75] in equation (3.2):

$$\tau(\lambda, L) = \tau_s + \tau_a = \frac{P_r}{P_o} = e^{-\Upsilon_T(\lambda).L} \tag{3.2}$$

where $\tau(\lambda, L)$ is the atmospheric transmittance in (km^{-1}), $\Upsilon_T(\lambda)$ is the total extinction coefficient or atmospheric attenuation or fading per unit length as a result of four different processes (aerosol and molecular absorption coefficients including aerosol and molecular scattering coefficients) [76], τ_s is the scattering-induced transmission, and τ_a is the transmittance through absorption [70]. The function $\Upsilon_T(\lambda)$ is thus an amalgamation of both atmospheric scattering and absorption representing the attenuation of the transmitted laser beam [77] and is further expressed in [8] as in equation (3.3):

$$\Upsilon_T(\lambda) = \alpha_m(\lambda) + \alpha_a(\lambda) + \beta_m(\lambda) + \beta_a(\lambda) \tag{3.3}$$

where $\alpha_m(\lambda)$ and $\alpha_a(\lambda)$ are the molecular and aerosol absorption coefficients, respectively. $\beta_m(\lambda)$ and $\beta_a(\lambda)$ is the molecular or Rayleigh scattering coefficient and is the aerosol or Mie scattering coefficient, respectively.

3.6 Scattering Attenuation

Mie scattering and Rayleigh scattering are recognized as the main scattering mechanisms. Mie scattering occurs when the radiated wavelength is of a similar sequence to the particle size of the molecular and atmospheric gases [20]. Then Rayleigh scattering occurs when the particle size of the gaseous molecules in the atmosphere is smaller than the optical light signal wavelength [78].

The significant photon scatterer is fog because of its particle size comparable to the wavelength band of interest in FSOC (0.5 μm – 2 μm), such that the particle scattering becomes the most significant factor during the scattering process in FSO technology [79].

Mie scatterings are used to calculate the effects of fog, but this method is so complex that it demands precise and detailed information about the fog's properties. Another option would be to utilize visibility range data as an alternative approach [80]. This approach uses an empirical model, grounded in Mie scattering theory, to quantify the attenuation coefficient of fog, enabling the estimation of fog's impact on optical signals. Thus, the scattering transmittance is given as in equation (3.4):

$$\tau_s = e^{-\Upsilon_{f.L}} \tag{3.4}$$

where L defines the length of the propagation channel, and Υ_f is the fog attenuation factor caused by Mie scattering [81]. The behaviour for the fog coefficient of the induced signal loss in the atmosphere is the predominant source of FSO scattering from visibility to near-infrared wavelength, expressed through the Kruse model [82] in equation (3.5):

$$\Upsilon_f = \frac{3.91}{V} \times \left(\frac{\lambda}{550\ nm}\right)^{-q} \tag{3.5}$$

where V is the visual range (visibility) of the atmosphere, λ is the operating transmission wavelength corresponding to the maximum spectrum of the solar band (550 nm), and q is the particle diameter distribution of the atmosphere [38]. Then, the derived specific atmospheric attenuation in decibels per propagation length (dB/km) is specified in equation (3.6) by [83]:

$$\Upsilon_f(V) = 10\log e^{\Upsilon_f} \approx 4.343\Upsilon_f \tag{3.6}$$

The absorption characteristics are wavelength-dependent, so the wavelength band with the least amount of absorption is also known as the propagation or transmission window, as illustrated in Table 3.2.

Table 3.2. Optical Propagation Window [26]

Thermal radiation spectrum	**Spectral range (μm)**
Visible and very near Infrared	0.4–1.4
Near Infrared	1.4–1.9 and 1.9–2.7
Mean Infrared	2.7–4.3 and 4.5–5.2
Far Infrared	8–14
Extreme Infrared	16–28

The requirements to calculate the fading attenuation are the properties of the particle size distribution coefficient. To determine the particle size distribution coefficient within fog conditions, Kruse's and Kim's Model are utilized [84].

i. *Kruse's Model:* To determine the particle size distribution coefficient in Kruse's Model, the expression is given in equation (3.7) by [85]:

$$q = \begin{cases} 1.6 & \text{if } V > 50 \text{ km} \\ 1.3 & \text{if } 6 \text{ km} < V < 50 \text{ km} \\ 0.585V^{\frac{1}{3}} & \text{if } V < 6 \text{ km} \end{cases} \tag{3.7}$$

ii. *Kim's Model:* The appropriate model for extremely high attention is Kim's Model. To determine the particle size distribution coefficient in Kim's Model, the expression is given in (3.8):

$$q = \begin{cases} 1.6 & \text{if } V > 50 \text{ km} \\ 1.3 & \text{if } 6 \text{ km} < V < 50 \text{ km} \\ 0.16V + 0.34 & \text{if } 1 \text{ km } V < 6 \text{ km} \\ V - 0.5 & \text{if } 0.5 \text{ km} < V < 1 \text{ km} \\ 0 & \text{if } 6 \text{ km} < V < 0.5 \text{ km} \end{cases} \tag{3.8}$$

Al-Gailani et al. in [31] have anticipated the prediction of fog attenuation coefficient for the wavelengths between 690 and 1550 nm, and have separated these as advection and radiation fog [86]. They give the expression for the advection fog attenuation coefficients as in equation (3.9):

$$\alpha_{advection}(\lambda) = \frac{0.11478\lambda + 3.8367}{V} \tag{3.9}$$

Radiation fog is related to the ground cooling by radiation. Ali in [87] provides the radiation fog attenuation coefficients as in equation (3.10):

$$\alpha_{Radiation}(\lambda) = \frac{0.18126\lambda^2 + 0.13709\lambda + 3.7502}{V} \tag{3.10}$$

The specific attenuation for both types of fog is given by Ghoname et al. in [88] as in equation (3.11):

$$\Upsilon_{spec} = \frac{10}{\ln(10)}\alpha(\lambda) \tag{3.11}$$

There are certain categories for various atmospheric attenuation and visibility bands as shown in Table 3.3.

Table 3.3 Visual range of weather conditions and attenuation values [74]

Climatic Parameters	**Visual Range (km)**	**Attenuation (dB/km)**
Thick Fog	0.2	75
Moderate fog	0.5	28.9
Light fog	0.770–1	18.3
Thin fog/heavy rainfall (25 mm/hr)	1.9–2	6.9
Haze/medium rain (12.5 mm/hr)	2.8–4	4.6
Clear weather /drizzle (12.5 mm/hr)	18–20	0.54
Very clear weather	23–50	0.19

3.7 Turbulence-Induced Signal Attenuation

The impact of index inhomogeneities on the FSO signal propagation relies on the turbulence cell size, as defined below [89]:

i. The laser beam tends to bend and becomes distorted once the turbulence cell's diameter gets smaller than the laser beam diameter. There is constructive and destructive interference caused by the small deviation in the arrival times of different elements of the beam wavefront, as shown in Figure 3.2(a). This causes a temporal imbalance in the signal strength of a laser beam at the detection point. This effect is called scintillation.

ii. The optical path bends when the beam is more collimated than the air turbulence molecules. As seen in Figure 3.2(b), the solid rays (beams) leave the optic source and are deflected the moment they pass through the larger air cells, appearing off-axis instead of on-axis as required in the absence of turbulence.

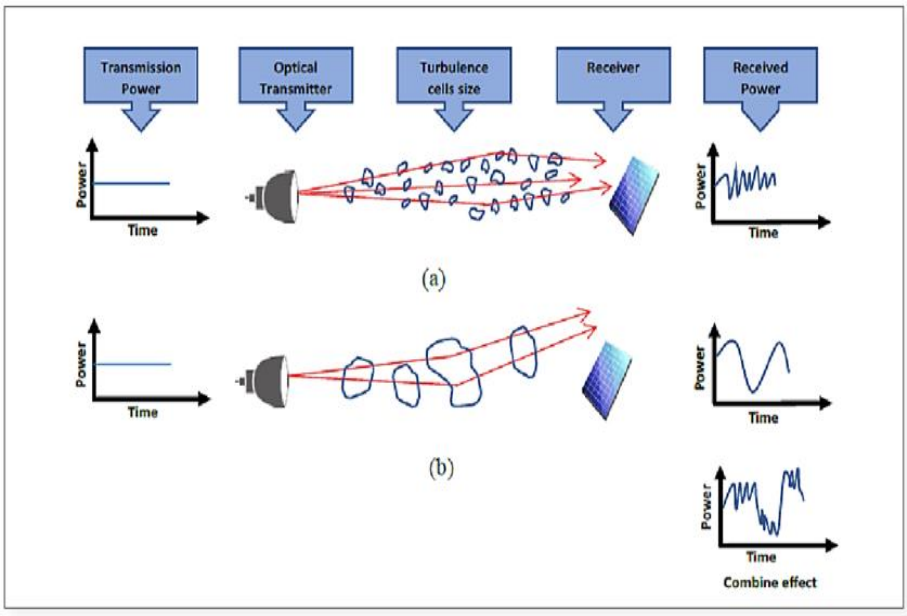

Figure 3.2 Comparison of Turbulent Cell Size with (a) Scintillation and (b) Beam Wander [89].

When the laser beam propagates through the atmosphere, it contacts temporal random fluctuations and a small spatial refractive index, commonly known as optical turbulence, which is typically due to turbulent eddies caused by stochastic variations in temperature. The atmospheric temperature is not constant at any given location due to these fluctuations. As a result, every variation occurring in the air temperature leads to spatial and temporal variation in the refractive indices of the atmospheric optical channel [90].

3.7.1 Scintillation losses

In FSOC systems, the primary cause of turbulence is the spreading of the beam due to diffraction, which redistributes the beam's energy across its width, leading to distortions and signal degradation. The state of robust diverged beams is also known as scintillation, the scintillation strength parameter σ_I^2 is the standardized fluctuation in light wave strength and is referred to equation (3.12) in [91]:

$$\sigma_I^2 = \frac{\langle I^2 \rangle - \langle I \rangle^2}{\langle I \rangle^2} \tag{3.12}$$

For a given time, a series of intensity measurements, represented by I, the angle brackets are used to represent the average over time. According to Rytov's theory [92], the scintillation index is a quantitative parameter that characterizes the extent of scintillation, offering a

mathematical representation of the signal's intensity fluctuations induced by atmospheric turbulence. This describes the variations in intensity caused by atmospheric turbulence, enabling the calculation of this phenomenon's impact on optical signals. The scintillation index is a mathematical parameter that measures the turbulence intensity in FSOC links [76], characterizing the fluctuations in signal strength and phase caused by atmospheric disturbances. The Rytov theory describes the scintillation index as a function of atmospheric conditions and laser link characteristics [93] and formulated in equation (3.13):

$$\sigma_I^2(L) = 1.23 \times K^{7/6} \times C_n^2 \times L^{11/16} \tag{3.13}$$

where the constant variables have been previously defined in Section 2.7.1. However, the constant 1.23 in (3.13) presumes that the signal is a plane signal. While for a spherical signal, it would assume 0.5 as the constant. Then, the turbulence attenuation recommended by the International Telecommunication Union (ITU) is determined by the structure parameter of the refractive index C_n^2 based on the atmospheric transmission medium. In characterizing the intensity of atmospheric turbulence, the RISP variation of the air (C_n^2) is the key aspect [94, 95]. The most popular turbulence structure model of atmospheric turbulence strength is based on the Hufnagel Valley (H-V) model in $m^{-2/3}$ and it is mathematically expressed in [96, 97] as seen in equation (3.14):

$$C_n^2 = \left[0.00594 \times \left(\frac{v}{27}\right)^2 \times \left((10^{-5})h\right)^{10} \times e^{\frac{-h}{1000}}\right] + \left[(2.7 \times 10^{-16}) \times e^{\frac{-h}{1500}}\right] + \left[A_0 \times e^{\frac{-h}{100}}\right] \tag{3.14}$$

where v is rms of wind speed (m/s), h is the altitude (m), and A_o represents the typical standard turbulence intensity at ground level, equal to 1.7 x 10^{-14}.

The wind and altitude are the primary factors contributing to the alteration of this variable. Turbulence gives rise to three principal consequences: scintillation, beam wander, and beam spreading [98]. The C_n^2 value for FSO links closer to the ground is ≈ 1.7 x 10^{-14} $m^{-2/3}$ and 8.4 x 10^{-14} $m^{-2/3}$. In general, the C_n^2 value typically ranges between 10^{-13} $m^{-2/3}$ (strong turbulence strength) and 10^{-15} $m^{2/3}$ (weak turbulence strength), with the usual mean value of 10^{-15} $m^{-2/3}$ [26].

3.8 Turbulence Modelling

This research specifically chooses the gamma-gamma distribution channel to model the FSO link among various turbulence models. The gamma-gamma channel modelling will be combined with the mathematical tool Meijer-G Function. This tool, known for its ability to handle complex mathematical functions, will be used to derive the formulas for the performance metrics. This integrated approach enables evaluating the FSO link's performance under various turbulence conditions.

3.8.1 Gamma-gamma Model

According to [99], the gamma-gamma model comprehensively represents atmospheric turbulence across various intensities, from mild to severe, including intermediate conditions. This distribution channel model is founded upon the modulation process, which suggests that the fluctuation of light radiation as it travels through a turbulent atmosphere can be divided into two distinct effects: scattering on a small and refracting on a large scale. The normalized received irradiance is denoted as I_o, and described as the multiplication of two random variables namely $I_x$and I_y, thus, expressed in [100] as seen in equation (3.15):

$$I_o = I_x I_y \tag{3.15}$$

The application of the gamma-gamma distribution channel model is not just theoretical. It enables the derivation of the PDF of the atmospheric turbulence-induced beam variation, which is attributed to the variations in air mass, as described by [101] in (2.7). Therefore, the scintillation parameters α and β are formulated for the plane wave [102] given in equations (3.16) and (3.17):

$$\alpha = \left[exp\left(\frac{0.49\sigma_I^2}{\left(1+1.11\sigma_I^{12/5}\right)^{7/6}} \right) - 1 \right]^{-1} \tag{3.16}$$

$$\beta = \left[exp\left(\frac{0.51\sigma_I^2}{\left(1+0.69\sigma_I^{12/5}\right)^{5/6}} \right) - 1 \right]^{-1} \tag{3.17}$$

For spherical wave, it is then formulated in [103] and expressed as equations (3.18) and (3.19):

$$\alpha = \left[exp\left(\frac{0.49\sigma_I^2}{\left(1+0.18d^2+0.56\sigma_I^{12/5}\right)^{7/6}} \right) - 1 \right]^{-1} \tag{3.18}$$

$$\beta = \left[exp\left(\frac{0.51\sigma_I^2\left(1+0.69\sigma_I^{12/5}\right)^{-5/6}}{\left(1+0.9d^2+0.62d^26\sigma_I^{12/5}\right)^{5/6}} \right) - 1 \right]^{-1} \tag{3.19}$$

where $d \triangleq (kD^2/4L)$, D typically represents the diameter of the receiver aperture, which is the size of the opening of the receiver that collects the optical signal, and σ_I^2 is the Rytov is a theoretical measure of the plane wave's scintillation, determining the severity of the scintillation index, which assesses the number of intensity fluctuations caused by atmospheric turbulence. Rytov variance is established for both planar and spherical waves, denoted in [51], then formulated by equations (3.20) and (3.21):

$$\sigma_{I|_{plane}}^2 = 1.23 \times K^{7/6} \times C_n^2 \times L^{11/6} \tag{3.20}$$

$$\sigma_{I|spherical}^2 = 0.492 \times K^{7/6} \times C_n^2 \times L^{11/6} \tag{3.21}$$

where the constant variables have been previously defined in Section 2.7.1. The scintillation index measures the strength of the turbulence along the FSOC link [76, 104, 105].

The performance evaluation of the FSO system is conducted considering performance metrics such as the average BER, SNR, and channel capacity through the gamma-gamma distribution channel. This analysis is not just theoretical but has direct implications for the real-world performance of the FSO system. The Meijer-G-function is the mathematical tool employed to expand the approach of obtaining the closed-form expression for the performance of the three metrics parameters. The general overview of the PDF curve of the gamma-gamma distribution channel is plotted using MATLAB, as shown in Figure 3.3. This considers various atmospheric turbulence strength conditions as in equation (2.7). Figure 3.4 displays the PDF curves for both the Bessel Function and the gamma-gamma statical model. The modified Bessel function is per scintillation parameters found in equations (3.16) and (3.17) for the plane wave. Both curves are observed at the channel state, which has an extreme turbulence strength within a 3 km range.

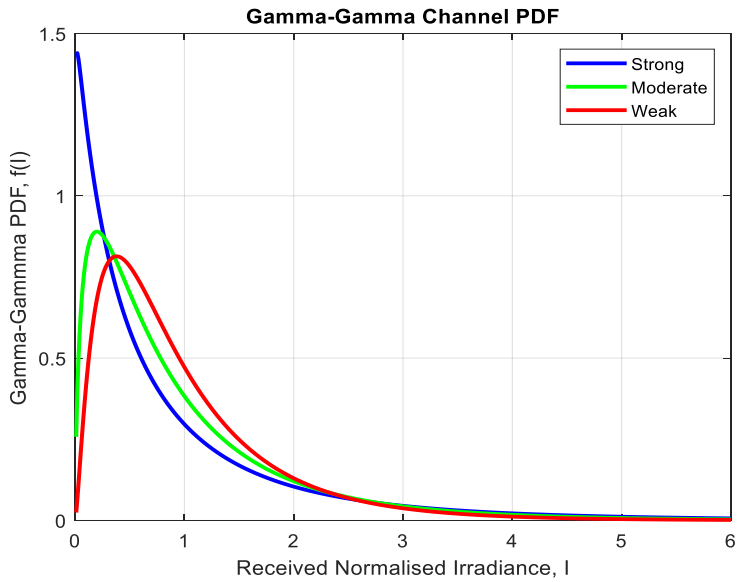

Figure 3.3 PDF curve for gamma-gamma distribution channel subjected to various turbulence conditions.

Therefore, the Scintillation Index (SI) serves as a metric to measure the severity of turbulence in the system, and its value is represented in [106, 107] as equation (3.22):

$$SI = \frac{1}{\alpha} + \frac{1}{\beta} + \frac{1}{\alpha\beta} \tag{3.22}$$

The PDF $f_I(I)$ for the state of the channel I combining both the path loss I_l and scintillation I_a in [16, 108] can be expressed as equation (3.23):

$$f_I(I) = \left|\frac{d}{dI}\left(\frac{I}{I_l}\right)\right| f_{I_a}\left(\frac{I}{I_l}\right) \tag{3.23}$$

where, the $\left|\frac{d}{dI}\left(\frac{I}{I_l}\right)\right|$ is the absolute value of the derivative of the normalized intensity (I/I_l) concerning the intensity (I).

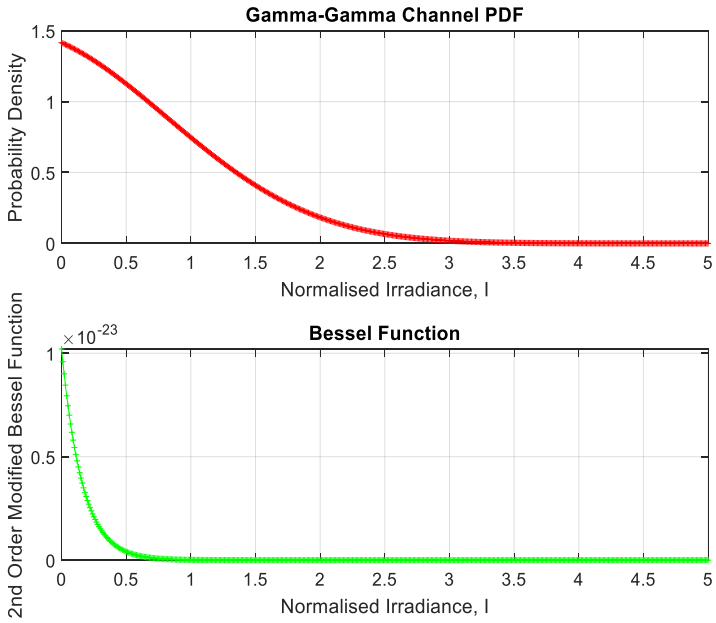

Figure 3.4 Gamma-gamma distribution and Bessel Function versus Normalised Signal.

3.8.2 Meijer-G Function

The Meijer-G function is utilized to derive the Bessel Function $K_v(x)$ formulation [17] as in equation (3.24):

$$K_v(x) = \frac{1}{2} G_{0,2}^{2,0}\left(\frac{x^2}{4}\middle|\begin{matrix}\frac{-}{v}, \\ \frac{v}{2}, \frac{-v}{2}\end{matrix}\right) \tag{3.24}$$

where $G_{\mathrm{n,m}}^{\mathrm{m,n}}(x)$ is a standard G function parameter, and furthermore, according to [17] the PDF of the gamma-gamma distribution, $f_{I_a}(I_a)$ has a closed-form expression involving the Meijer-G function, which is given as equation (3.25):

$$f_{I_a}(I_a) = \left(\frac{(\alpha\beta)^{\frac{\alpha+\beta}{2}}}{\Gamma(\alpha)\Gamma(\beta)} I_a^{\frac{\alpha+\beta}{2}-1}\right)\left(G_{0,2}^{2,0}\alpha\beta I_a\middle|\begin{matrix}\frac{\alpha-\beta}{-}, \\ \frac{2}{2}, \frac{\beta-\alpha}{2}\end{matrix}\right) \; I > 0 \tag{3.25}$$

The parameter variables have been previously defined in Section 2.7.4. Furthermore, the combined PDF of the channel states $f_I(I)$ is derived by incorporating the effects of path losses and scintillation into the gamma-gamma model resulting in a comprehensive expression for the PDF in [64] as equation (3.26):

$$f_I(I) = \frac{(\alpha\beta)^{\frac{\alpha+\beta}{2}}}{\Gamma(\alpha)\Gamma(\beta)} \frac{I^{\frac{\alpha+\beta}{2}-1}}{I_l^{\frac{\alpha+\beta}{2}}} G_{0,2}^{2,0}\left(\alpha\beta\frac{I}{I_l}\middle|\begin{matrix}\frac{\alpha-\beta}{-}, \\ \frac{2}{2}, \frac{\beta-\alpha}{2}\end{matrix}\right) \tag{3.26}$$

where $I = I_l + I_a$, combines the effects of atmospheric turbulence-induced intensity fluctuations and path losses, providing a comprehensive representation of the channel r behaviour.

3.8.3 BER Analysis using Meijer-G Function

The average BER can be calculated by integrating the conditional error probability $P_e(I)$, through the PDF of the atmospheric turbulence channel state $f_I(I)$ in [109, 110] as in equation (3.27):

$$BER = \int_0^\infty P_e(I)\, f_I(I) dI \tag{3.27}$$

i. OOK Modulation Scheme

The SNR of the electrical signal in an OOK modulated system [64] is measured as seen in equation (3.28):

$$SNR(I) = \gamma I^2 = \frac{P_t^2 R^2 I^2}{\sigma_n^2} \tag{3.28}$$

where the SNR is represented by γ which is the product of the mean amount of optical power transmitted P_t and the responsivity of the APD receiver, R divided by the channel noise variance, σ_n^2.

By implementing the complementary error function (erfc(·)), the $P_e(I)$ for the OOK modulation is defined [101] in equation (3.29):

$$P_e(I) = \frac{1}{2} erfc\left(\sqrt{\frac{SNR(I)}{2}}\right) \tag{3.29}$$

where the instantaneous value of the received SNR is γI^2, and γ is the mean SNR. Now, the above erfc(·) can be expressed as a Meijer-G [101] in equation (3.30):

$$P_e(I) = \frac{1}{2\sqrt{\pi}} G_{1,2}^{0,2}\left(\frac{\gamma I^2}{2}\middle|\begin{matrix}1\\0,\frac{1}{2}\end{matrix}\right) \tag{3.30}$$

The modified value of $P_e(I)$ from equation (3.30) and the merged channel behaviour from equation (3.26) are substituted into equation (3.27) and the resulting mean BER is given by (3.31):

$$f_I(I) = \int_0^{\infty} \frac{(\alpha\beta)^{\frac{\alpha+\beta}{2}}}{\Gamma(\alpha)\Gamma(\beta)} \frac{I^{\frac{\alpha+\beta}{2}-1}}{I_l^{\frac{\alpha+\beta}{2}}} G_{0,2}^{2,0}\left(\alpha\beta \frac{I}{I_l}\middle| \frac{\alpha-\bar{\beta},}{2}, \frac{\beta-\alpha}{2}\right) \times \frac{1}{2\sqrt{\pi}} G_{1,2}^{0,2}\left(\frac{\gamma I^2}{2}\middle| \begin{matrix}1\\ 0,\frac{1}{2}\end{matrix}\right) \quad (3.31)$$

Evaluating these integrals yields a derived closed-form expression for the average BER of SIM-OOK is provided in equation (3.32):

$$P_{e(OOK)} = \frac{2^{\alpha+\beta}}{8\sqrt{\pi^3}\,\Gamma(\alpha)\Gamma(\beta)} G_{5,2}^{2,4}\left(\frac{8\gamma I_l^2}{(\alpha\beta)^2}\middle| \begin{matrix}\frac{1-\alpha}{2}, \frac{2-\alpha}{2}, \frac{1-\beta}{2}, \frac{2-\beta}{2}, 1\\ 0, \frac{1}{2}\end{matrix}\right) \quad (3.32)$$

where the rest of the above parameter variables have been previously defined in Section 2.7.4 and Section 3.8.2.

ii. BPSK Modulation Scheme

Furthermore, the $P_e(I)$ for BPSK modulated system is defined in terms of the erfc(·) as seen in equation (3.33):

$$P_e(I) = \frac{1}{2} erfc\left(\sqrt{SNR(I)}\right) \quad (3.33)$$

where the parameter variables have been previously defined in (3.29). Furthermore, the equation (3.33) can be represented by its equivalent erfc(·) in terms of the Meijer G-function in equation (3.34):

$$P_e(I) = \frac{1}{2\sqrt{\pi}} G_{1,2}^{0,2}\left(\frac{\gamma I^2}{2}\middle| \begin{matrix}1\\ 0,\frac{1}{2}\end{matrix}\right) \quad (3.34)$$

Giving out the corresponding close form expression for BER as in (3.35):

$$P_{e(BPSK)} = \frac{2^{\alpha+\beta}}{8\sqrt{\pi^3}\,\Gamma(\alpha)\Gamma(\beta)} G_{5,2}^{2,4}\left(\frac{16\gamma I_l^2}{(\alpha\beta)^2}\middle| \begin{matrix}\frac{1-\alpha}{2}, \frac{2-\alpha}{2}, \frac{1-\beta}{2}, \frac{2-\beta}{2}, 1\\ 0, \frac{1}{2}\end{matrix}\right) \quad (3.35)$$

where the parameter variables have been previously defined in Section 2.7.4 and Section 3.8.2.

iii. DPSK Modulation Scheme

Then the $P_e(I)$, for DPSK modulated system is defined in terms of the erfc(·), is seen in equation (3.36):

$$P_e(I) = \frac{1}{2} erfc\left(\frac{\sqrt{SNR(I)}}{\sqrt{2}}\right) \quad (3.36)$$

The corresponding Meijer-G function for this complementary function, erfc(·) can be expressed as shown in (3.37):

$$P_e(I) = \frac{1}{2\sqrt{\pi}} G_{0,1}^{1,0}\left(\gamma I^2 \middle| \begin{matrix} - \\ 0 \end{matrix}\right) \tag{3.37}$$

Now, the corresponding closed-form expression for BER is given by equation (3.38):

$$P_{e(DPSK)} = \frac{2^{\alpha+\beta}}{8\sqrt{\pi}\,\Gamma(\alpha)\Gamma(\beta)} G_{4,1}^{1,4}\left(\frac{8\gamma I_l^2}{(\alpha\beta)^2} \middle| \begin{matrix} \frac{1-\alpha}{2}, \frac{2-\alpha}{2}, \frac{1-\beta}{2}, \frac{2-\beta}{2} \\ 0 \end{matrix}\right) \tag{3.38}$$

where the parameter variables have been previously defined in equation (3.29), Section 2.7.4 and Section 3.8.2.

3.8.4 Channel Capacity Analysis using Meijer-G function

Another essential factor for describing the effectiveness of an FSO communication system is the average channel capacity. This parameter pertains to the highest amount of information sent over a specific duration and is being assessed in this context as well. As per Shannon's theorem [111], the channel capacity when optical intensity remains constant can be formulated as $C = B\log_2(1 + SNR)$, where B is the transmission bandwidth. The capacity is defined as a random variable that varies with the received SNR values as a function of variable *I*. Thus, the average channel capacity is formulated [112] as in equation (3.39):

$$C = \int_0^\infty B\log_2(1 + SNR(I)) f_I(I) dI \tag{3.39}$$

By substituting equation (3.26) into (3.39) the average channel capacity of the OOK format is thus simplified in (3.40):

$$C = \int_0^\infty B log_2(1 + \gamma I^2) \frac{(\alpha\beta)^{\frac{\alpha+\beta}{2}}}{\Gamma(\alpha)\Gamma(\beta)} \frac{I^{\frac{\alpha+\beta}{2}-1}}{I_l^{\frac{\alpha+\beta}{2}}} G_{0,2}^{2,0}\left(\alpha\beta \frac{I}{I_l} \middle| \begin{matrix} \frac{\alpha-\beta}{2}, \frac{\beta-\alpha}{2} \end{matrix}\right) dI \tag{3.40}$$

The log function in (3.38) is solved using the Meijer-G Function expression [112]: $log_2(1 + x) = \frac{1}{ln2} G_{2,2}^{1,2}\left[x \middle| \begin{matrix} 1,1 \\ 1,0 \end{matrix}\right]$.

Therefore, the channel capacity integral is formulated as in (3.41).

$$C = \frac{B}{\ln(2)} \int_0^\infty ln(1 + \gamma I^2) \frac{(\alpha\beta)^{\frac{\alpha+\beta}{2}}}{\Gamma(\alpha)\Gamma(\beta)} \frac{I^{\frac{\alpha+\beta}{2}-1}}{I_l^{\frac{\alpha+\beta}{2}}} G_{0,2}^{2,0}\left(\alpha\beta \frac{I}{I_l} \middle| \begin{matrix} \frac{\alpha-\beta}{2}, \frac{\beta-\alpha}{2} \end{matrix}\right) dI \tag{3.41}$$

Furthermore, the average channel capacity closed-form expression based on the gamma-gamma channel distribution model can be obtained for OOK, BPSK, and DPSK transmission format as in equations (3.42), (3.43), and (3.44) with the aid of the integral property of the Meijer-G function as:

$$C_{(OOK)} = \frac{2^{\alpha+\beta-2}B}{4\pi \ln(2)\,\Gamma(\alpha)\Gamma(\beta)} G_{6,2}^{1,6}\left(\frac{16\gamma I_l^2}{(\alpha\beta)^2}\middle|{}^{1,1,\frac{1-\alpha}{2},\frac{2-\alpha}{2},\frac{1-\beta}{2},\frac{2-\beta}{2}}_{0,1}\right) \tag{3.42}$$

$$C_{(BPSK)} = \frac{2^{\alpha+\beta}B}{\pi \ln(2)\,\Gamma(\alpha)\Gamma(\beta)} G_{6,2}^{1,6}\left(\frac{16\gamma I_l^2}{(\alpha\beta)^2}\middle|{}^{1,1,\frac{1-\alpha}{2},\frac{2-\alpha}{2},\frac{1-\beta}{2},\frac{2-\beta}{2},1}_{0,1}\right) \tag{3.43}$$

$$C_{(DPSK)} = \frac{2^{\alpha+\beta}B}{\pi \ln(2\Gamma)(\alpha)\Gamma(\beta)} G_{6,1}^{1,6}\left(\frac{8\gamma I_l^2}{(\alpha\beta)^2}\middle|{}^{1,1,\frac{1-\alpha}{2},\frac{2-\alpha}{2},\frac{1-\beta}{2},\frac{2-\beta}{2}}_{1,0}\right) \tag{3.44}$$

3.9 Summary

This section provides a detailed research design, system modelling and channel capacity metrics with a focus on understanding the feasibility of FSO technology within the regions of interest. The study models atmospheric turbulence using gamma-gamma distribution channels. The Meijer-G function is utilized to extract meaningful patterns from the dataset, specifically examining atmospheric effects on optical signal attenuation, especially under dense fog and turbulence conditions.

Simulation of FSO links using BPSK, DPSK, and OOK transmission schemes show relationship between laser beam performance and atmospheric losses due to factors such as fog, Mie scattering, and signal attenuation caused by weather conditions. By modeling these effects, this research elucidates how different climatic and environmental factors influence FSO technology, providing valuable insights for improving optical communication systems under varying weather conditions.

Chapter Four Results and Discussion

4.1 Variability of Atmospheric Weather Parameters

Atmospheric events usually impact communication system signals due to its variation per location and time. This requires constant check to proffer solutions or enhance the systems. Numerous studies and statistical assessments have been conducted to examine the FSO system [113] in different atmospheric conditions, including factors such as atmospheric scattering and turbulence. However, further investigation over some specific locations still requires attention due to impressive demands on communication systems. This chapter presents some atmospheric parameters measurements (such as atmospheric visibility, relative humidity, temperature, and wind speed) obtained over two coastal regions of South Africa.

The rest the chapter is organized as follows: Provides the cumulative distribution of the atmospheric weather parameters in Section 4.2. Presentation of aggression models for visibility in Section 4.3. Provides the summary of the chapter in Section 4.4.

4.2 Cumulative Distributions of the Atmospheric Weather Parameters

Two years atmospheric data from January 2018 to December 2019 obtained from SAWS were analysed in this section to understand weather patterns and trends over the locations of study.

4.2.1 Monthly Mean Variation of Visibility

Figure 4.1 shows the measured monthly mean visibility (km) observed over the study duration for the locations of study in Cape Town. It is evident that the highest mean visibility is accumulated during the summer months (December to February) with values of 30, 31.33, and 29.62 km for the year 2018. Similarly, in 2019 the highest mean visibility is observed during the spring and summer season (November to January) with values of 30.6, 30.5, and 30.3 km. This implies that the warmer months offer the clearest conditions, with the highest mean visibility values, compared to other seasons, for both years under study. Nevertheless, the winter season had the poorest visibility, with the lowest mean visibility values of 20.92 km in August 2018 and 18.2 km in July 2019. Therefore, the winter period had the most

reduced visibility, with the lowest mean visibility values, compared to other seasons, for both years under study.

Figure 4.2 shows the observed variation in the measured monthly mean visibility (km) recorded over the study locations for the study duration in Port Elizabeth. The year 2018 shows that in early summer, autumn, and early winter months (December, April, June, and July) had the highest mean visibility with values between 29.24 km and 29.67 km. The lowest visibility was recorded in February 2018 with the value of 25.16 km. However, the highest mean visibility was recorded during January, June, July, and October, in 2019 with values ranging from 29 km to 29.6 km whereas the lowest mean visibility of 23.3 km was recorded during April 2019.

Figure 4.3 presents the measured monthly mean visibility pattern for both cities over the two years. The results indicate a seasonal variation in visibility between Port Elizabeth and Cape Town. Port Elizabeth had better visibility during the early summer, autumn, winter, and spring months, while Cape Town had better visibility during the late spring and summer months, with the highest visibility values recorded. Port Elizabeth's recorded visibility ranged from 28.43 to 29.54 km, while Cape Town's visibility peaked at 29.41 km to 30.82 km during these months.

Figure 4.4 illustrates the standard deviation of visibility patterns over both study locations. Generally, same trend was observed over locations, both cities exhibit the highest visibility in July and the lowest in September, indicating a consistent trend of peak deviation and minimal deviation, except for the month of April which shows a diverse trend.

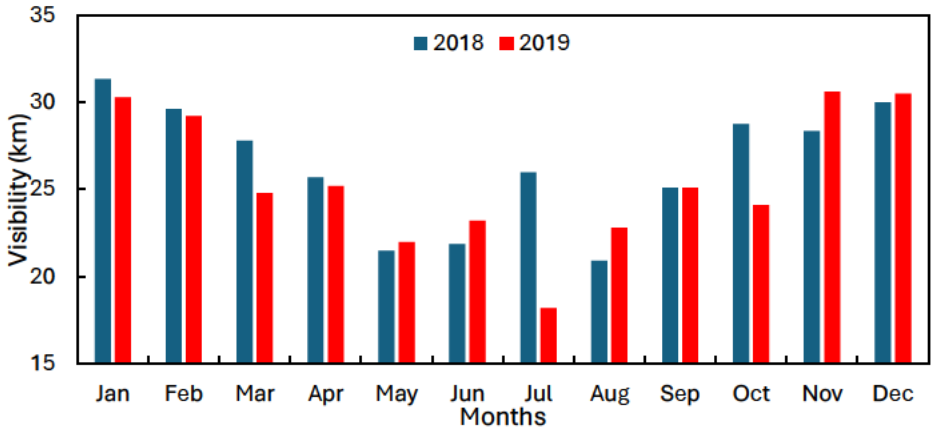

Figure 4.1 Variation of measured monthly mean visibility in Cape Town.

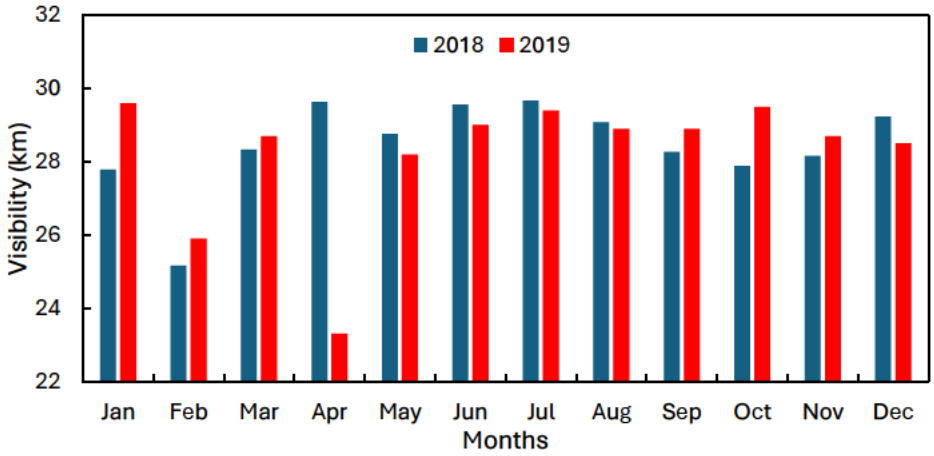

Figure 4.2 Variation of measured monthly mean visibility in Port Elizabeth.

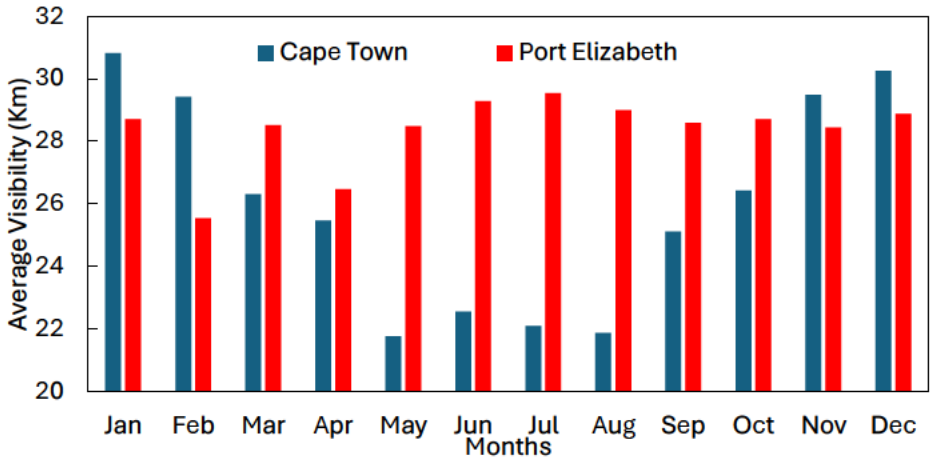

Figure 4.3 Measured monthly mean of visibility over two years for both locations of study.

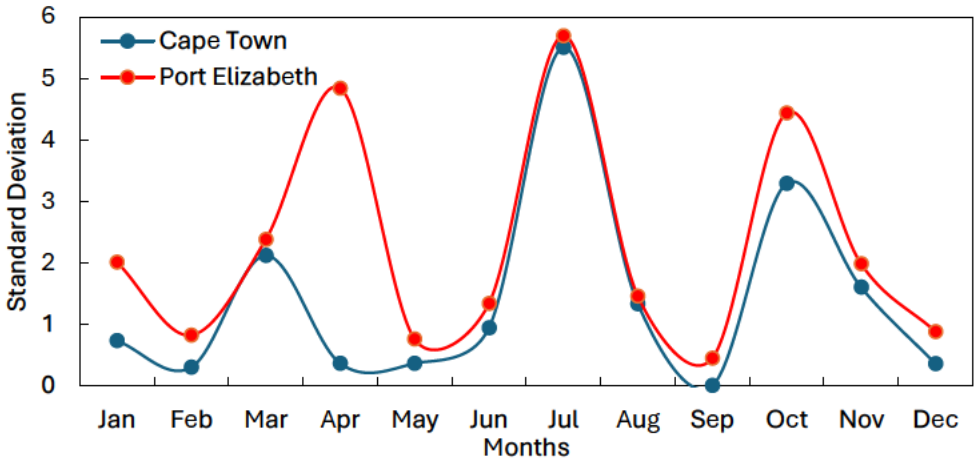

Figure 4.4 Standard deviation of visibility pattern for both stations.

4.2.2 Monthly Mean Variation of Temperature

Figure 4.5 displays the monthly mean temperature (°C) measurements recorded in Cape Town during the study period, revealing that the highest mean temperatures occurred during the summer, early autumn, and late spring months (December to February, March, and November) for both 2018 and 2019, thus indicating a consistent temperature pattern across both years.

The monthly mean temperature measurements shown in Figure 4.6 for Port Elizabeth exhibit a distinct seasonal pattern, with peak temperatures occurring during the early summer, early autumn, and late winter months (April, June, and July), and minimum temperatures during the winter months (June to August).

The statistical analysis of monthly mean temperature measurements presented in Figure 4.7 reveals that Port Elizabeth experiences a bimodal temperature distribution, with a maximum in December and February and a minimum in August. Meanwhile, Cape Town exhibits a trimodal distribution, with a broader temperature maximum during the summer months (December, January, and February) and a minimum during the winter months (June, July, and August).

Figure 4.8 presents the standard deviation temperature, with Port Elizabeth exhibiting the highest deviation in January and the lowest deviation in April and May. Cape Town indicated a consistent trend of peak deviation in September and minimal deviation in April.

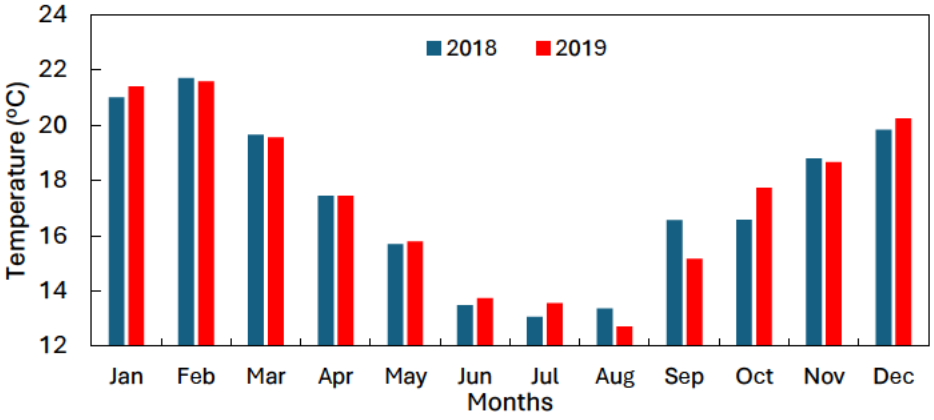

Figure 4.5 Variation of measured monthly mean temperature in Cape Town.

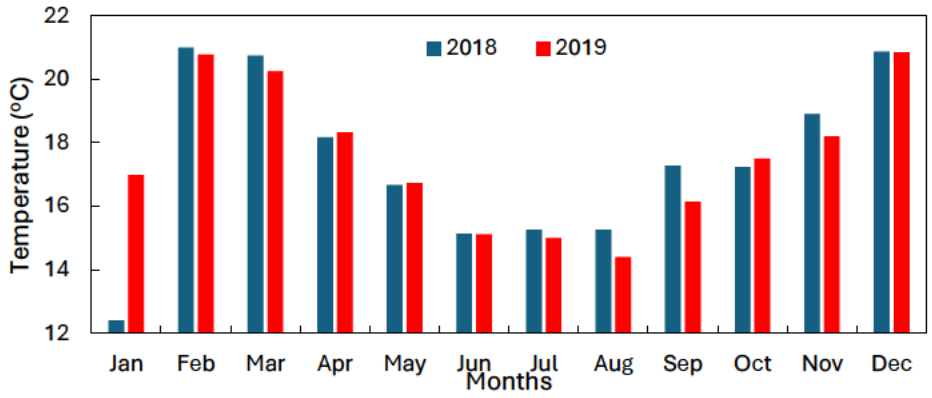

Figure 4.6 Variation of measured monthly mean temperature in Port Elizabeth.

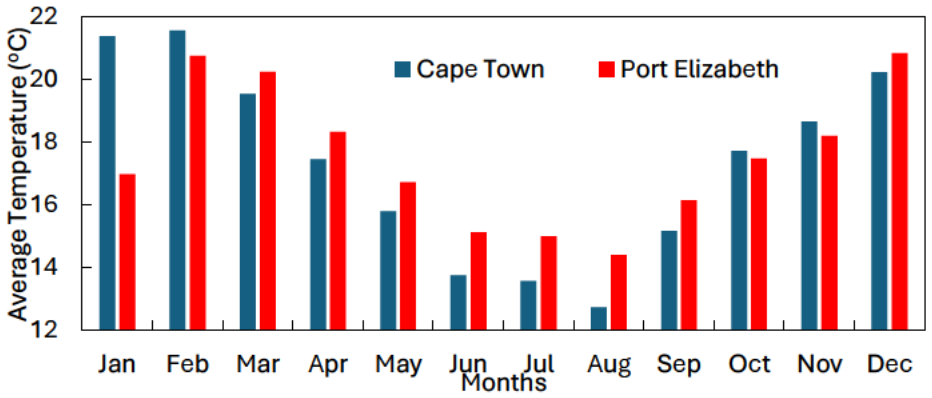

Figure 4.7 Measured monthly average temperature over two years for both locations of study.

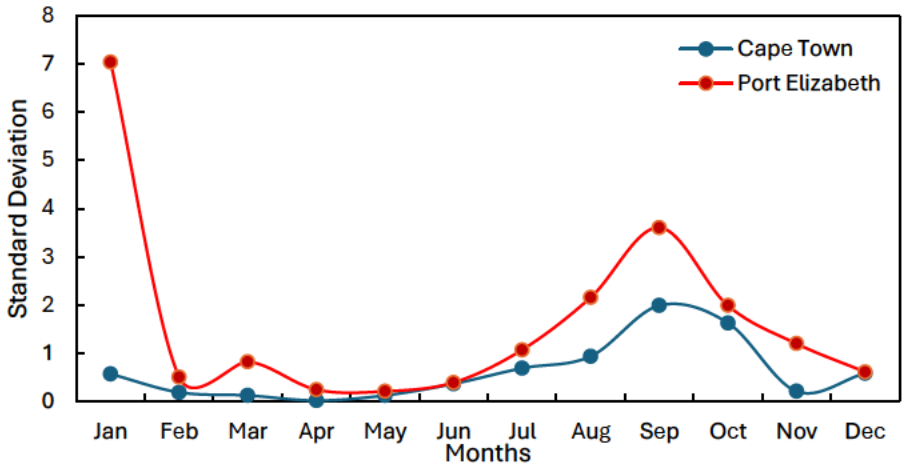

Figure 4.8 Standard deviation temperature pattern for both stations.

4.2.3 Monthly Mean Variation of Relative Humidity

Figure 4.9 displays the mean relative humidity (%) levels measured monthly over the study period in Cape Town. The data reveals that the highest mean humidity levels occurred in May and June, corresponding to late autumn and early winter whereas the lowest mean humidity was recorded in November which is within late spring in year 2018. In contrast, the highest average humidity levels occurred in July, which falls within mid-winter, whereas the lowest mean humidity was recorded in January corresponding to mid-summer for the year 2019.

Figure 4.10 also illustrates the monthly mean relative humidity (%) variations observed in Port Elizabeth during the study period. In 2018, the highest average humidity levels were recorded in February and March (late summer and early autumn), while the lowest levels were observed in June and July (winter months). In contrast, in 2019, the highest average humidity levels were recorded in February, March, and April (late summer and autumn), while the lowest level was observed in January.

Figure 4.11 displays the measured monthly mean relative humidity patterns in both Cape Town and Port Elizabeth over the two-year study period. The data analysis reveals that Port Elizabeth experienced its highest humidity levels in February and March, followed by a significant drop to its lowest levels in June and July. In contrast, Cape Town recorded its highest humidity levels in July and August, while its lowest levels were observed in January.

Figure 4.12 shows the standard deviation of the relative humidity pattern in both Port Elizabeth and Cape Town, revealing that both cities experienced the highest variability in humidity levels in July and the lowest variability in June.

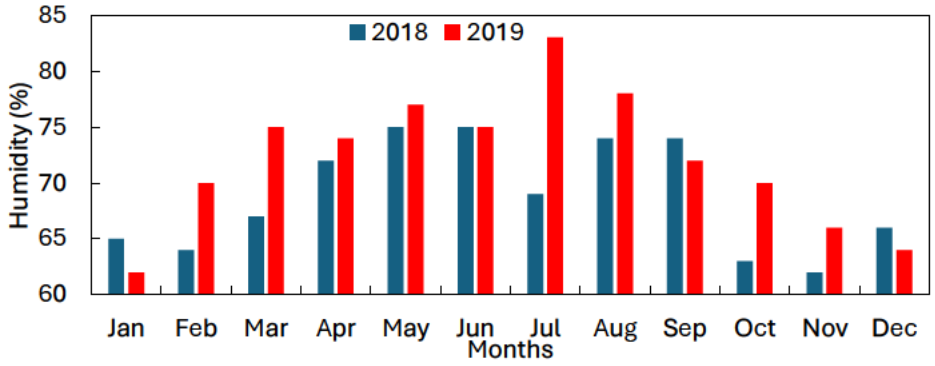

Figure 4.9 Variation of measured monthly mean relative humidity in Cape Town.

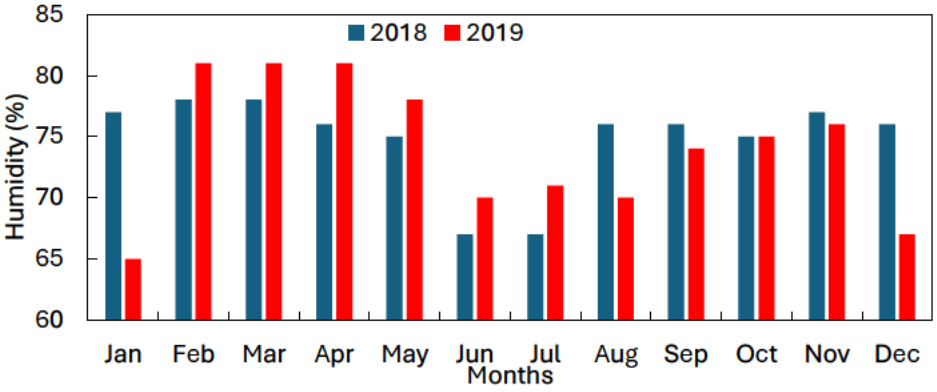

Figure 4.10 Variation of measured monthly mean relative humidity in Port Elizabeth.

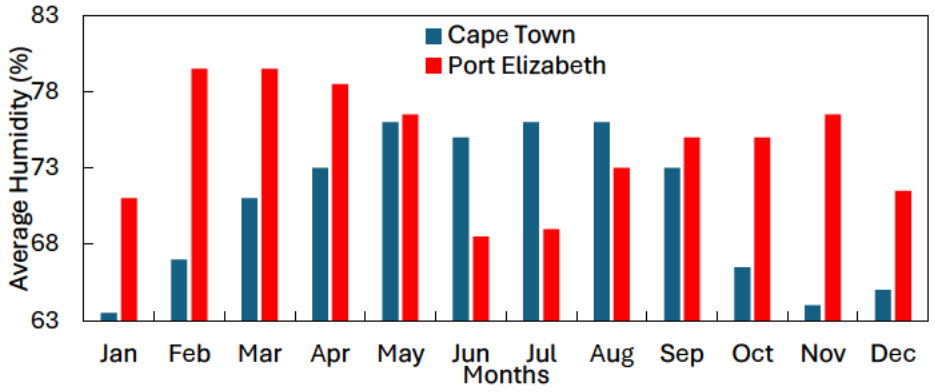

Figure 4.11 Measured monthly mean relative humidity over two years for both locations of study.

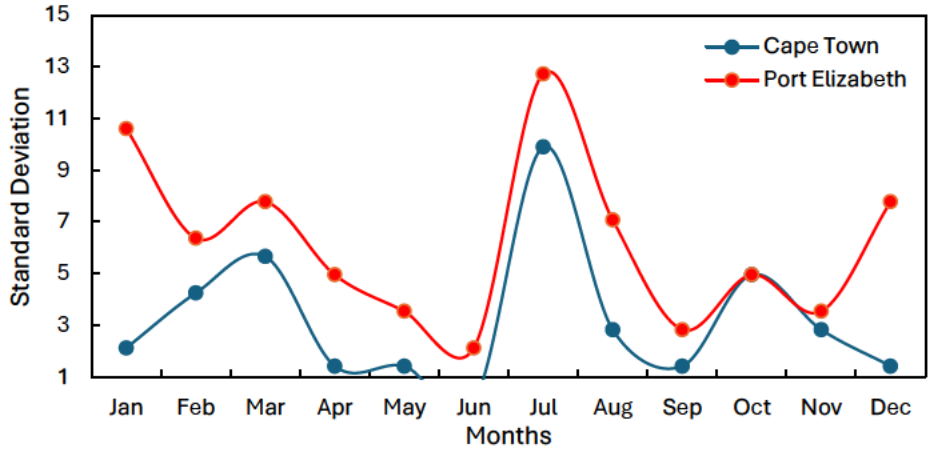

Figure 4.12 Standard deviation relative humidity pattern for both stations.

4.2.4 Monthly Mean Variation of Wind Speed

Figure 4.13 displays the monthly mean wind speed (km/h) measurements in Cape Town over the study period. The data reveals that in 2018, the highest average wind speed occurred in January (mid-summer), followed by a decline to the lowest average wind speed in July (mid-winter). However, in 2019, the pattern differed, with the highest average wind speed observed in December (early summer) and the lowest in May (late autumn).

Figure 4.14 displays the monthly mean wind speed (km/h) variations observed in Port Elizabeth during the study period. The data reveals that January (mid-summer) consistently had the highest average wind speed, while July 2018 recorded the lowest average wind speed. However, in 2019, the highest average wind speed was recorded in January and November, while the lowest mean wind speed was observed during May month.

Figure 4.15 shows the mean wind speed (km/h) patterns in both Cape Town and Port Elizabeth over the two-year study period. The analyzed data has revealed that both cities experienced their highest wind speeds in January. However, Cape Town had its lowest wind speeds in May and August, whereas Port Elizabeth had its lowest average wind speed in May.

Figure 4.16 displays the standard deviation of wind speed patterns in Port Elizabeth and Cape Town, indicating that both cities had the highest variability in wind speeds in July and

the lowest variability in June. This suggests that wind speeds in July were more unpredictable and spread out in both cities, while wind speeds in June were more consistent and stable.

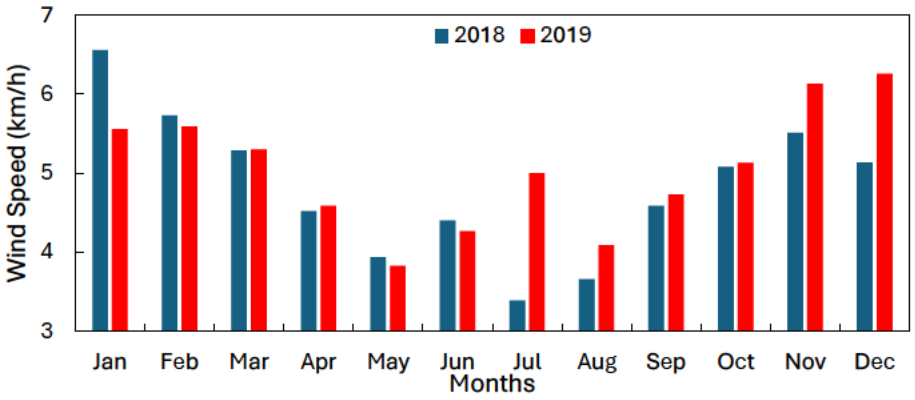

Figure 4.13 Variation of measured monthly mean wind speed in Cape Town.

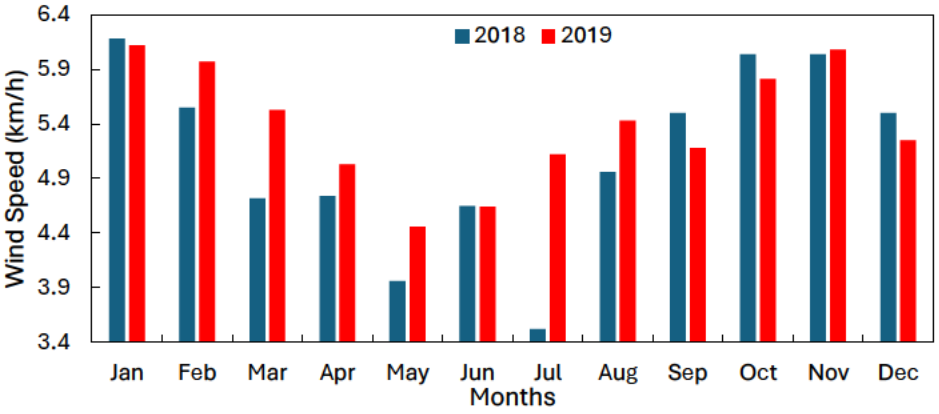

Figure 4.14 Variation of measured monthly mean wind speed in Port Elizabeth.

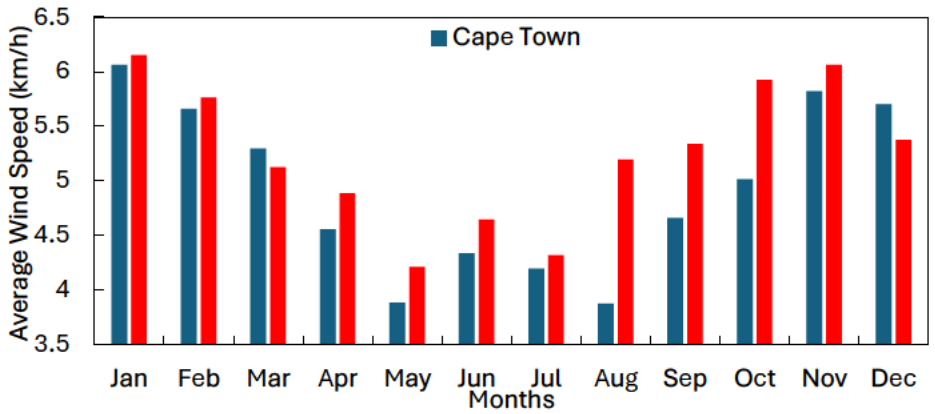

Figure 4.15 Measured monthly mean wind speed pattern for both years over the location of study.

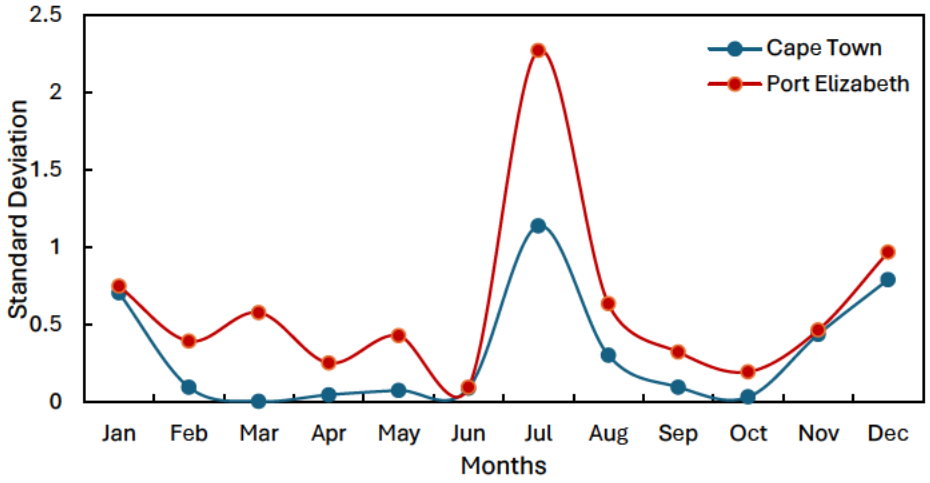

Figure 4.16 Standard deviation wind speed pattern for both stations.

4.3 Determination of regression models for visibility

This section evaluates the regression analysis on visibility and associated parameters (maximum temperature, relative humidity, and wind speed) to determine their influence on variability over the observed period and study location.

4.3.1 Aggregative Visibility (km) versus Aggregative Maximum Temperature (°C) year 2018-2019

Monthly visibility values are plotted in terms of maximum temperature values on a one-to-one monthly basis for the period spanning January 2018 to December 2019. A graphical representation was created, displaying monthly visibility values alongside corresponding maximum temperature values, on a month-by-month basis, for the two years from January 2018 to December 2019, providing patterns to analyse the relationship between the two parameters as seen in Figure 4.17 for Cape Town and Figure 4.18 for Port Elizabeth.

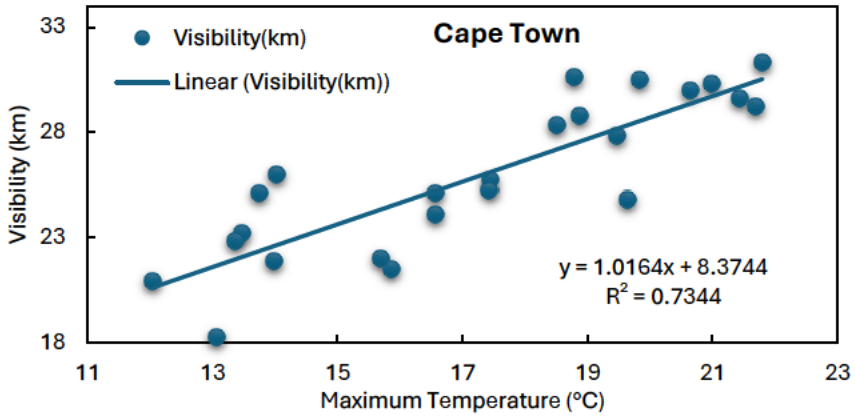

Figure 4.17 Aggregative visibility versus maximum temperature (°C) in Cape Town for two years.

As shown in Figure 4.17, the correlation coefficient is found to be 0.8569, indicating a strong positive correlation, with a standard error of 1.9326. The regression equation for predicting aggregate visibility against the corresponding maximum temperature is thereby determined as shown in equation (4.1):

$$V = 1.0164(Maximum\ Temperature) + 8.3774 \quad (4.1)$$

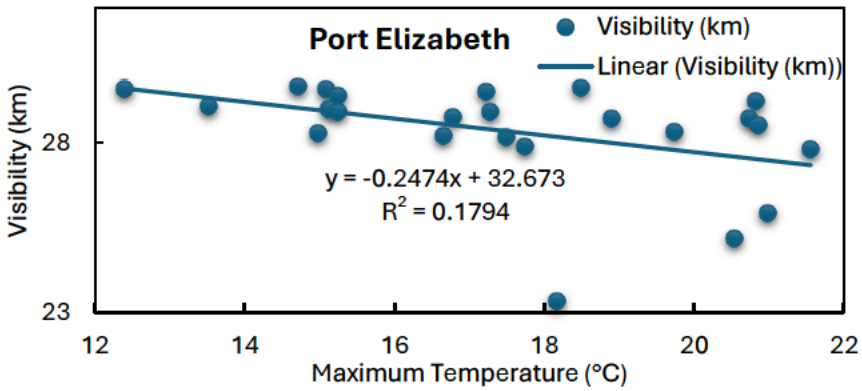

Figure 4.18 Aggregative visibility versus maximum temperature (°C) in Port Elizabeth for two years.

As depicted in Figure 4.18, the correlation coefficient is determined to be 0.4236, indicating a moderate positive correlation, with a standard error of 1.4179. Accordingly, the regression equation for predicting aggregate visibility against the corresponding maximum temperature is seen in equation (4.2):

$$V = -0.2474(Maximum\ Temperature) + 32.673 \quad (4.2)$$

4.3.2 Measured and forecasted visibility metrics based on aggregative maximum temperature regression model

Table 4.1 and Figures 4.19 and 4.20 displays measured and predicted visibility metrics for the year 2018 and 2019 utilizing the aggregative maximum temperature regression model in Cape Town, while Table 4.2 and Figures 4.21 and 4.22 in Port Elizabeth.

Table 4.1 Measured and forecasted visibility metrics based on aggregative maximum temperature regression mode with the RMSE difference in Cape Town.

Cape Town								
Months	**Measured Maximum Temperature (°C)**		**Measured Visibility (km)**		**Forecasted Visibility (km) for Maximum Temperature**		**RMSE (km)**	
	2018	**2019**	**2018**	**2019**	**2018**	**2019**	**2018**	**2019**
January	21.8	21	31.33	30.3	30.59	29.65	1.63299	2.17944
February	21.45	21.71	29.62	29.2	30.27	30.44		
March	19.47	19.64	27.79	24.8	28.41	28.14		
April	17.46	17.44	25.71	25.2	26.53	25.69		
May	15.87	15.7	21.49	22	25.04	23.76		
June	13.99	13.48	21.87	23.2	23.29	21.29		
July	14.04	13.07	25.98	18.2	23.33	20.83		
August	12.05	13.37	20.92	22.8	21.47	21.17		
September	13.76	16.57	25.1	25.1	23,07	24.73		
October	18,88	16.58	28,75	24.1	27.86	24.74		
November	18.51	18.8	28.34	30.6	27.51	27.21		
December	20.65	19.83	30	30.5	29.52	28.35		

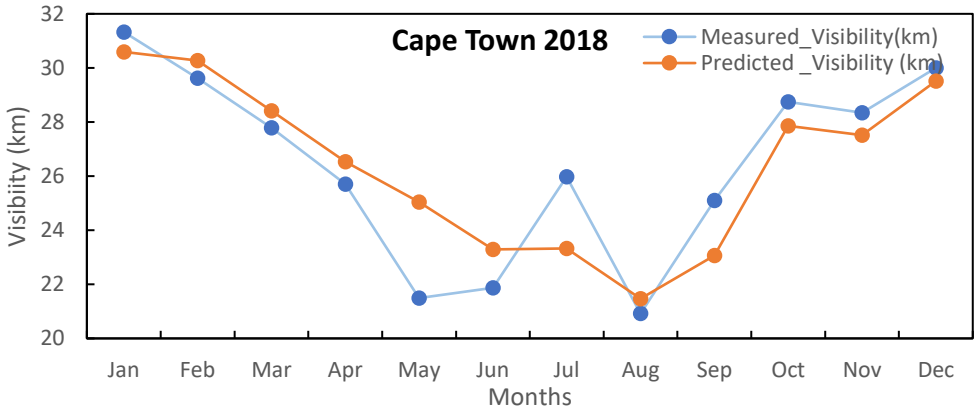

Figure 4.19 Variability between measured and forecasted visibility metrics utilizing the aggregative maximum temperature regression model for Cape Town in the year 2018.

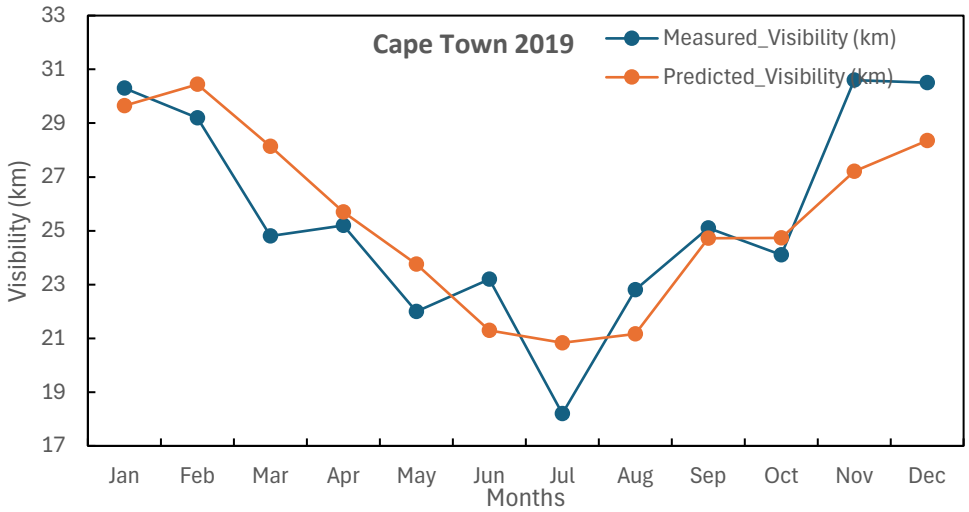

Figure 4.20 Variability between measured and forecasted visibility metrics utilizing the aggregative maximum temperature regression model for Cape Town in the year 2019.

Table 4.2 Measured and forecasted visibility metrics based on maximum temperature regression mode with the RMSE difference in Port Elizabeth.

Port Elizabeth								
Months	**Measured Maximum Temperature (°C)**		**Measured Visibility (km)**		**Forecasted Visibility (km) for Maximum Temperature**		**RMSE (km)**	
	2018	**2019**	**2018**	**2019**	**2018**	**2019**	**2018**	**2019**
January	21.56	29.6	27.79	29.6	27.58	29.59	1.19024	1.82574
February	20.54	25.9	25.16	25.9	27.81	27.26		
March	19.75	28.7	28.33	28.7	27.99	27.29		
April	18.49	23.3	29.63	23.3	28.27	28.01		
May	16.78	28.2	28.76	28.2	28.65	28.42		
June	15.09	29	29.56	29	29.03	28.85		
July	14.72	29.4	29.67	29.4	29.11	28.81		
August	13.53	28.9	29.08	28.9	29.38	28.81		
September	14.99	28.9	28.27	28.9	29.05	28.25		
October	17.74	29.5	27.88	29.5	28.44	28.27		
November	17.5	28.7	28.16	28.7	28.49	27.8		
December	20.83	28.5	29.24	28.5	27.74	27.26		

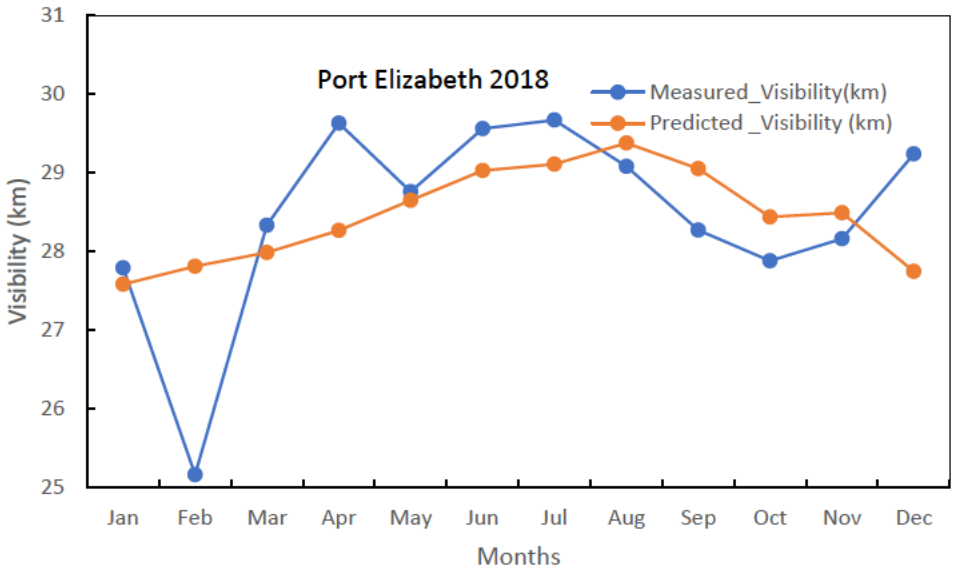

Figure 4.21 Variability between measured and forecasted visibility metrics utilizing the aggregative maximum temperature regression model in Port Elizabeth in the year 2018.

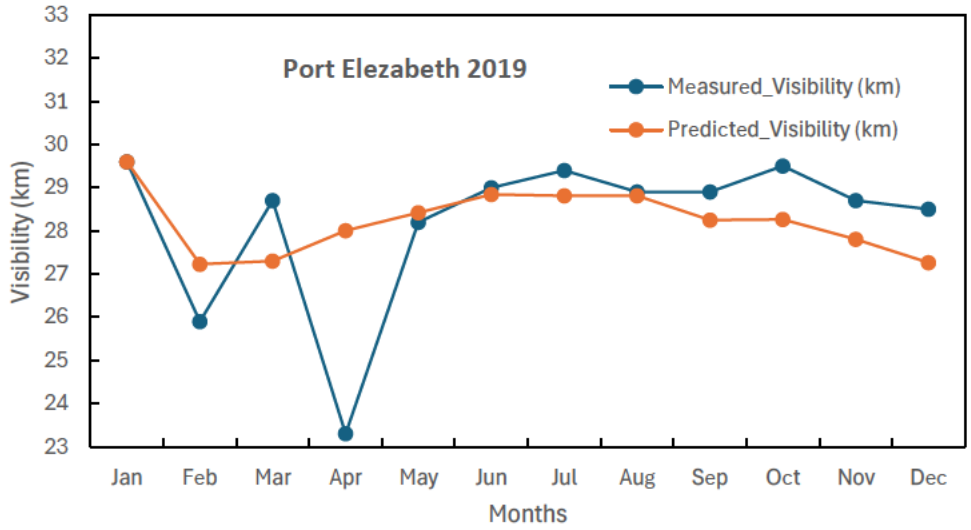

Figure 4.22 Variability between measured and forecasted visibility metrics utilizing the aggregative maximum temperature regression model in Port Elizabeth in the year 2019.

4.3.3 Mean Visibility (km) versus Mean Maximum Temperature (°C)

Figures 4.23 and 4.24 display the relationship between mean monthly visibility and temperature values for Cape Town, while Figures 4.25 and 4.26 illustrate the same relationship for Port Elizabeth, providing patterns to compare the two-year average monthly trends between visibility and temperature in both cities.

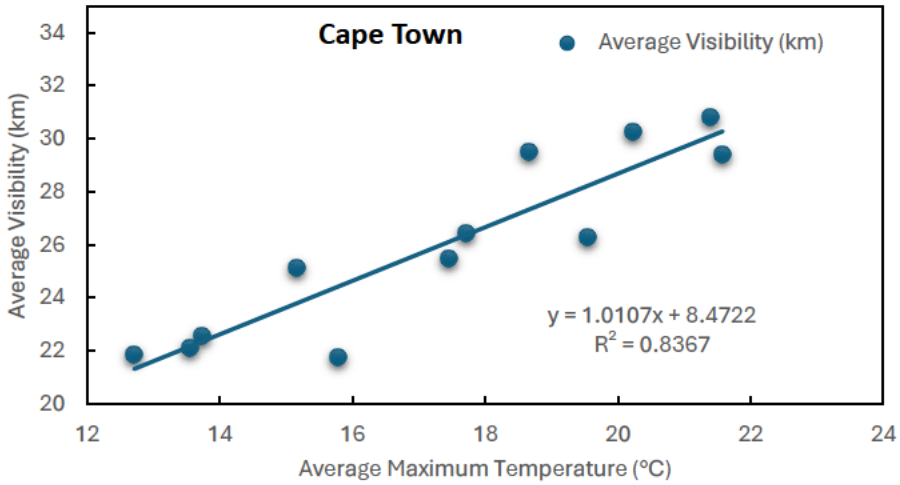

Figure 4.23 Mean visibility versus mean maximum temperature (°C) in Cape Town.

Figure 4.23 reveals a significant positive relationship, with a correlation coefficient of 0.9147 and a standard error of 1.4501. The regression equation for predicting mean visibility against the corresponding maximum temperature is thereby calculated as seen in equation (4.3):

$$V = 1.0107(Maximum\ Temperature) + 8.4722 \quad (4.3)$$

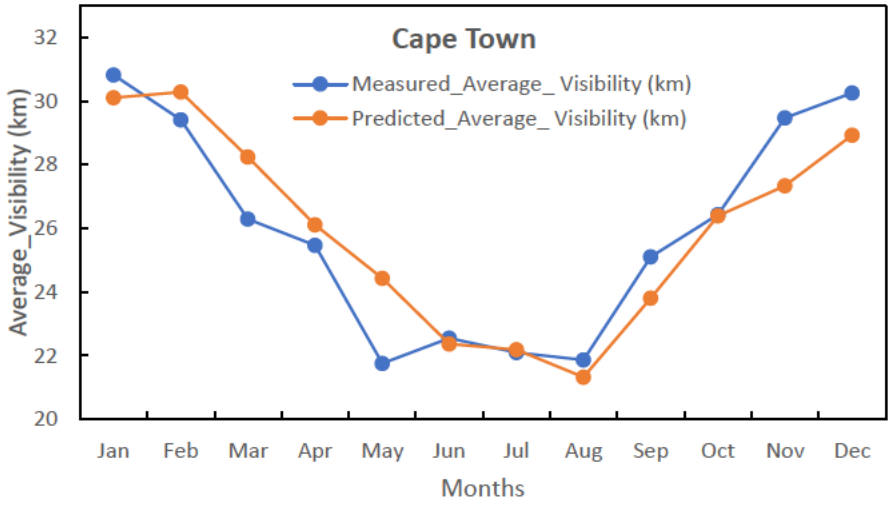

Figure 4.24 Variation between measured and forecasted mean visibility utilizing the average maximum temperature regression model in Cape Town, over two years.

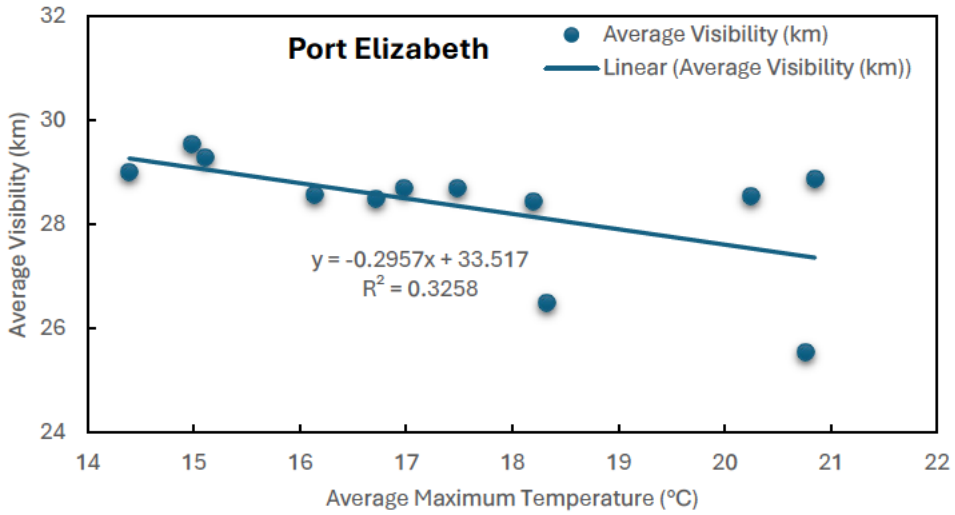

Figure 4.25 Mean visibility versus mean maximum temperature (°C) in Port Elizabeth

Figure 4.25 shows a correlation coefficient of 0.5708, with a standard error of 0.9979, indicating a reasonable positive relationship. The regression equation for predicting mean visibility against the corresponding maximum temperature is thereby determined by the formula in equation (4.4):

$$V = -0.2957(Maximum\ Temperature) + 33.517 \quad (4.4)$$

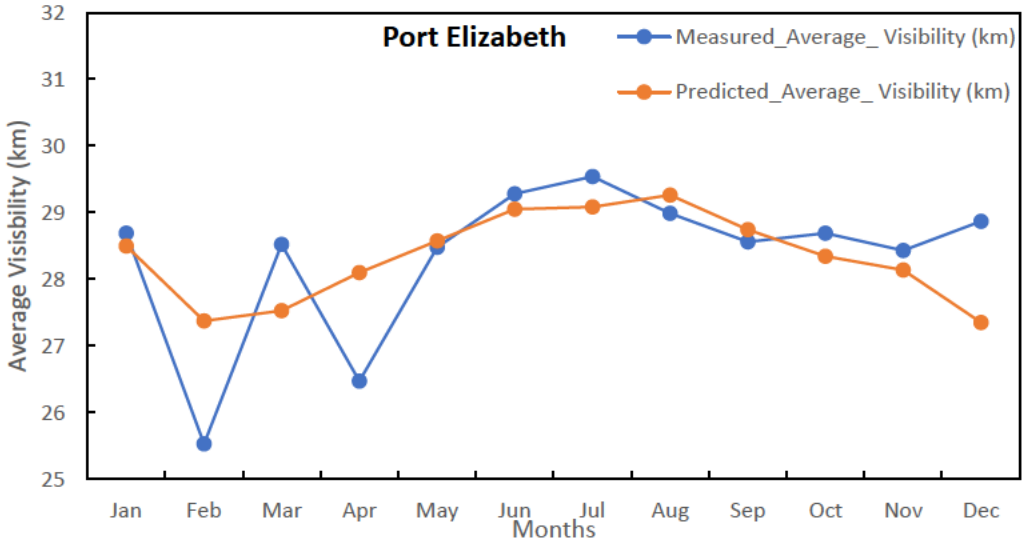

Figure 4.26 Variation between measured and forecasted mean visibility utilizing the average maximum temperature regression model in Port Elizabeth, over two years.

4.3.4 Aggregative Visibility (km) against Aggregative Relative Humidity (%)

Figure 4.27 is meant for Cape Town and Figure 4.28 is for Port Elizabeth showing the one-to-one monthly relative humidity and visibility values for the period spanning January 2018 to December 2019.

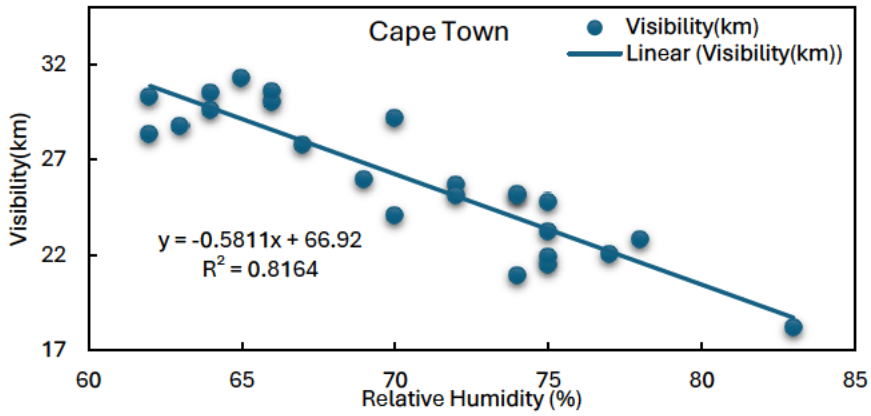

Figure 4.27 Aggregative visibility versus aggregative relative humidity (%) in Cape Town for two years.

Figure 4.27 reveals a significant positive relationship, with a correlation coefficient of 0.9035 and a standard error of 1.6069. The regression equation for aggregate visibility against the corresponding aggregate relative humidity is thereby calculated using equation (4.5):

$$V = 0.5811(Relative\ Humidity) + 66.92 \quad (4.5)$$

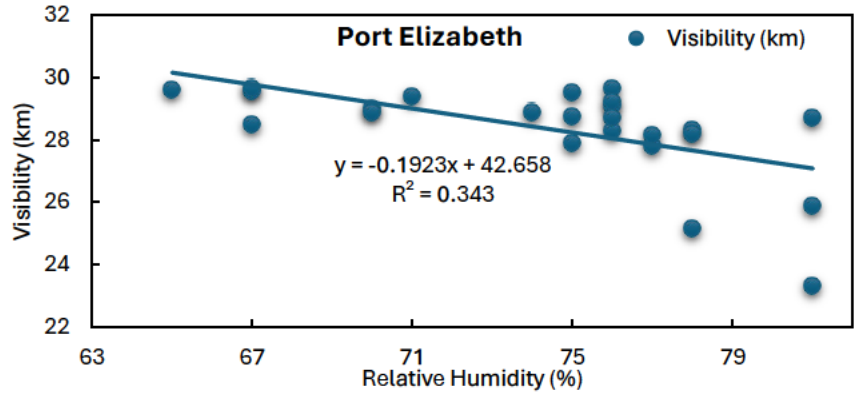

Figure 4.28 Aggregative visibility versus aggregative relative humidity (%) in Port Elizabeth for two years.

In Figure 4.28, the correlation coefficient is found to be 0.5857, indicating a moderate positive correlation, with a standard error of 1.2686. Accordingly, the regression equation for estimating aggregate visibility against the corresponding aggregate relative humidity is calculated using equation (4.6):

$$V = 0.1923(Relative\ Humidity) + 42.658 \quad (4.6)$$

4.3.5 Measured and forecasted visibility metrics based on aggregative relative humidity regression model

Table 4.3, Figures 4.29 and 4.30 are the measured and predicted visibility metrics for the year 2018 and 2019 utilizing the aggregative relative humidity regression model in Cape Town. Table 4.4, Figures 4.31 and 4.32 in Port Elizabeth.

Table 4.3 Measured and forecasted visibility metrics based on aggregative relative humidity regression mode with the RMSE difference in Cape Town.

Cape Town								
Months	**Measured Maximum Relative Humidity (%)**		**Measured Visibility (km)**		**Forecasted Visibility (km) for Relative Humidity**		**RMSE (km)**	
	2018	**2019**	**2018**	**2019**	**2018**	**2019**	**2018**	**2019**
January	65	62	31.33	30.3	28.82	31.59	1.73205	1.47196
February	64	70	29.62	29.2	29.45	26.79		
March	67	75	27.79	24.8	27.56	23.8		
April	72	74	25.71	25.2	24.42	24.4		
May	75	77	21.49	22	22.53	22.6		
June	75	75	21.87	23.2	22.53	23.8		
July	69	83	25.98	18.2	26.30	19.01		
August	74	78	20.92	22.8	23.16	22		
September	74	72	25.1	25.1	23.16	25.59		
October	63	70	28.75	24.1	30,08	26.79		
November	62	66	28.34	30.6	30.71	29.19		
December	66	64	30	30.5	28.19	30.39		

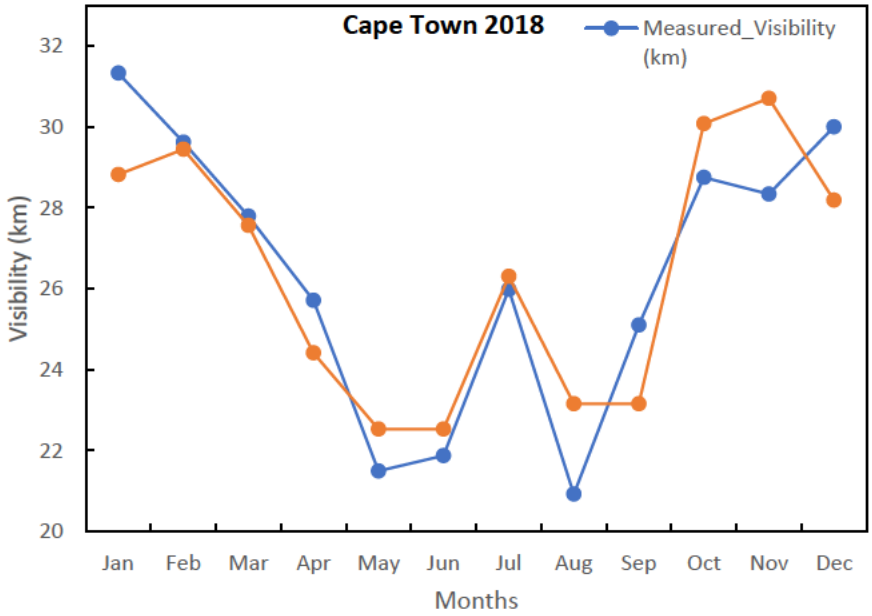

Figure 4.29 Fluctuations between measured and forecasted visibility metrics utilizing the aggregative relative humidity regression model in Cape Town, 2018.

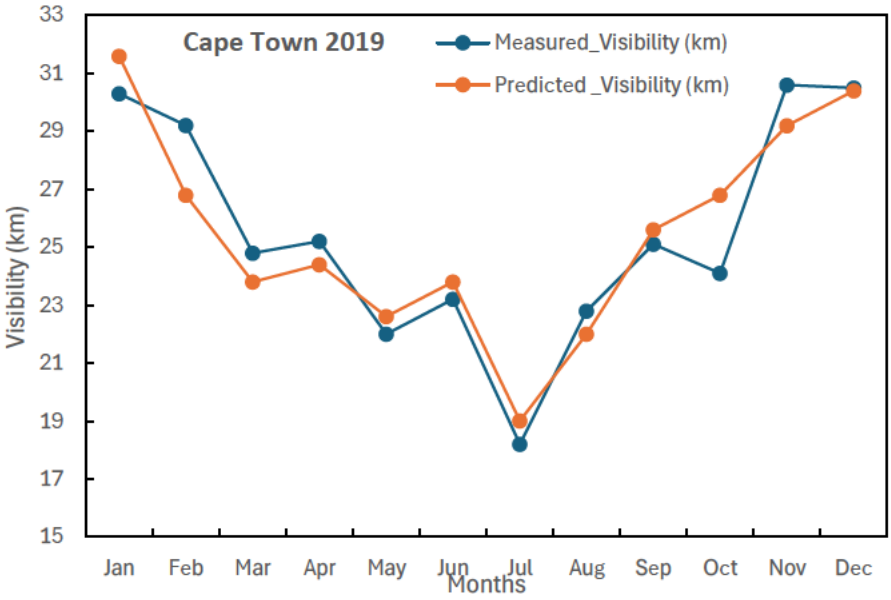

Figure 4.30 Fluctuations between measured and forecasted visibility metrics utilizing the aggregative relative humidity regression model in Cape Town, 2018.

Table 4.4 Measured and forecasted visibility metrics based on aggregative relative humidity regression mode with the RMSE difference in Port Elizabeth.

Port Elizabeth								
Months	**Measured Maximum Relative Humidity (%)**		**Measured Visibility (km)**		**Forecasted Visibility (km) for Relative Humidity**		**RMSE (km)**	
	2018	**2019**	**2018**	**2019**	**2018**	**2019**	**2018**	**2019**
January	77	65	27.79	29.6	28.07	30.06	1.15470	1.55456
February	78	81	25.16	25.9	27.89	26.81		
March	78	81	28.33	28.7	27.89	26.81		
April	76	81	29.63	23.3	28.25	26.81		
May	75	78	28.76	28.2	28.43	27.42		
June	67	70	29.56	29	29.87	29.05		
July	67	71	29.67	29.4	29.87	28.84		
August	76	70	29.08	28.9	28.25	29.05		
September	76	74	28.27	28.9	28.25	28.23		
October	75	75	27.88	29.5	28.43	28.03		
November	77	76	28.16	28.7	28.07	27.83		
December	76	67	29.24	28.5	28.25	29.66		

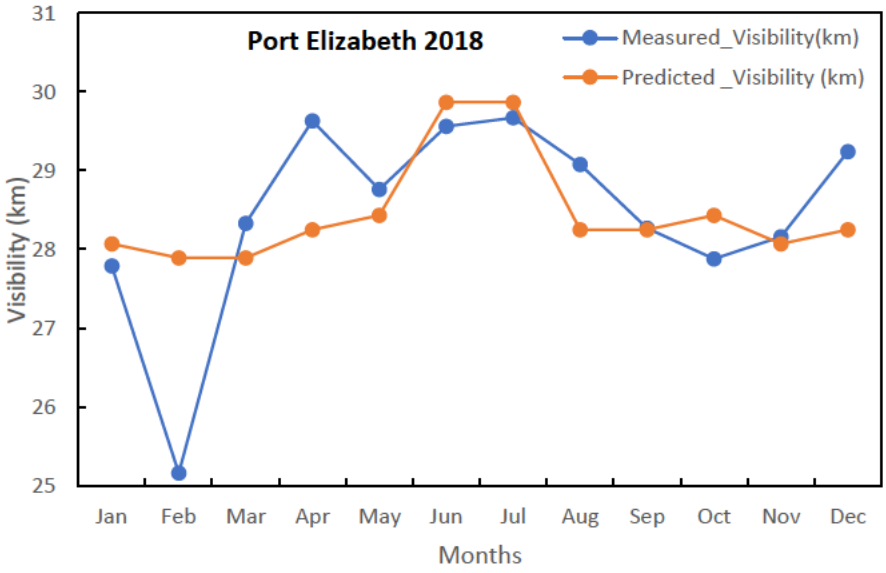

Figure 4.31 Fluctuations between measured and forecasted visibility metrics utilizing the aggregative relative humidity regression model in Port Elizabeth, 2018.

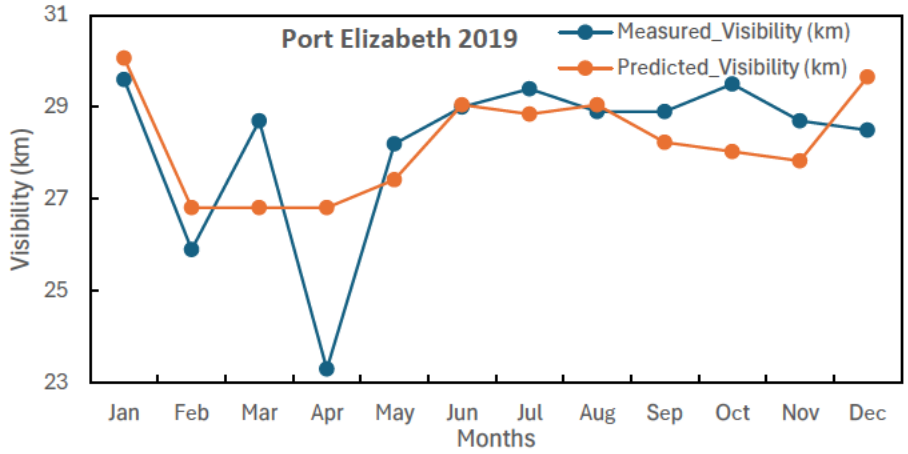

Figure 4.32 Fluctuations between measured and forecasted visibility metrics utilizing the aggregative relative humidity regression model in Port Elizabeth, 2019.

4.3.6 Mean Visibility (km) versus Mean Relative Humidity (%)

Figures 4.33 and 4.34 display the relationship between average monthly visibility and relative humidity values for Cape Town, while Figures 4.35 and 4.36 illustrate the same relationship for Port Elizabeth, providing a visual comparison of the two-year average monthly trends between visibility and relative humidity in both cities.

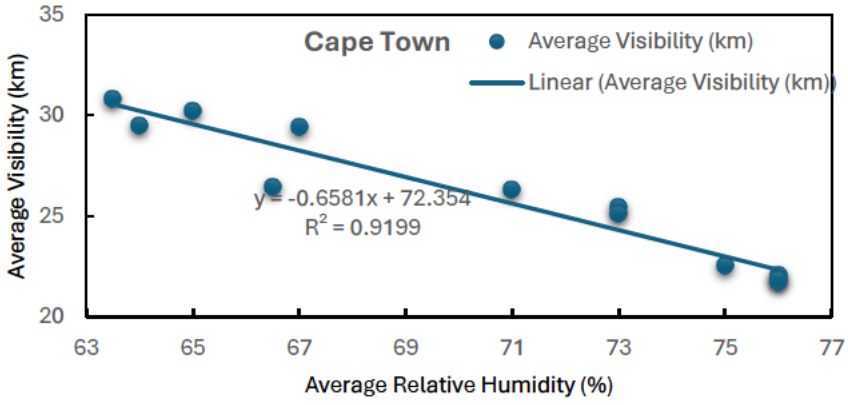

Figure 4.33 Mean visibility versus mean relative humidity (%) in Cape Town

In Figure 4.33, a strong positive correlation is evident, with a correlation coefficient of 0.9591 and a standard error of 1.0153. Consequently, the regression equation for estimating average visibility against corresponding relative humidity is determined using (4.7):

$$V = -0.6581(Relative\ Humidity) + 72.3543 \quad (4.7)$$

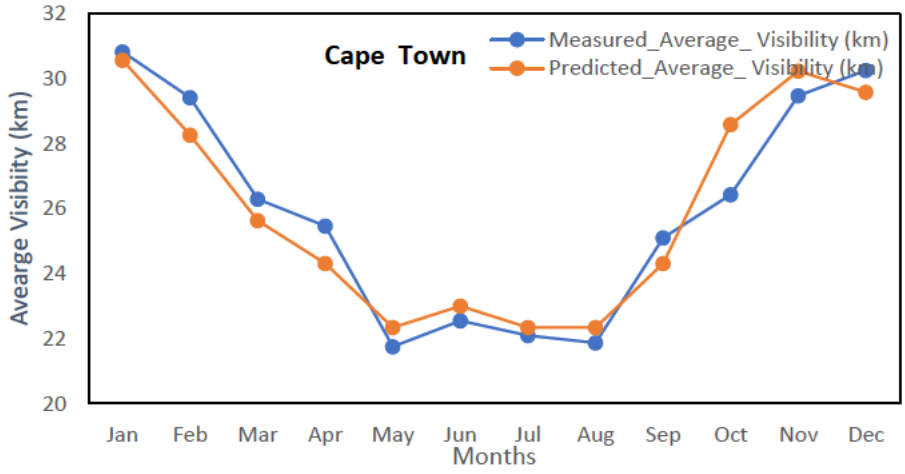

Figure 4.34 Variation between measured and forecasted mean visibility utilizing the mean relative humidity regression model in Cape Town, over two years.

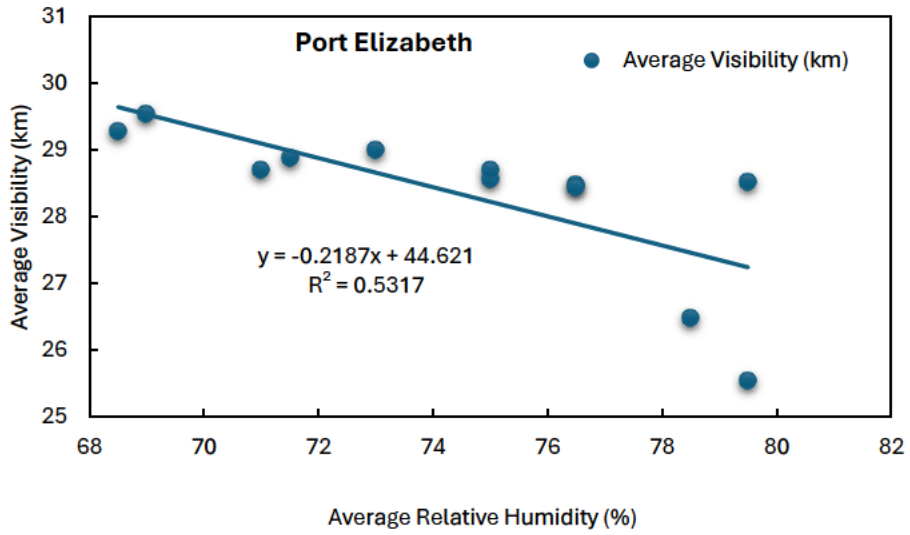

Figure 4.35 Mean visibility versus mean relative humidity (%) in Port Elizabeth.

As depicted in Figure 4.35, the correlation coefficient is found to be 0.7291, indicating a strong positive correlation, with a standard error of 0.8317. Accordingly, the regression equation for estimating aggregative visibility against corresponding average relative humidity is calculated using (4.8):

$$V = -0.2187(Relative\ Humidity) + 44.621 \quad (4.8)$$

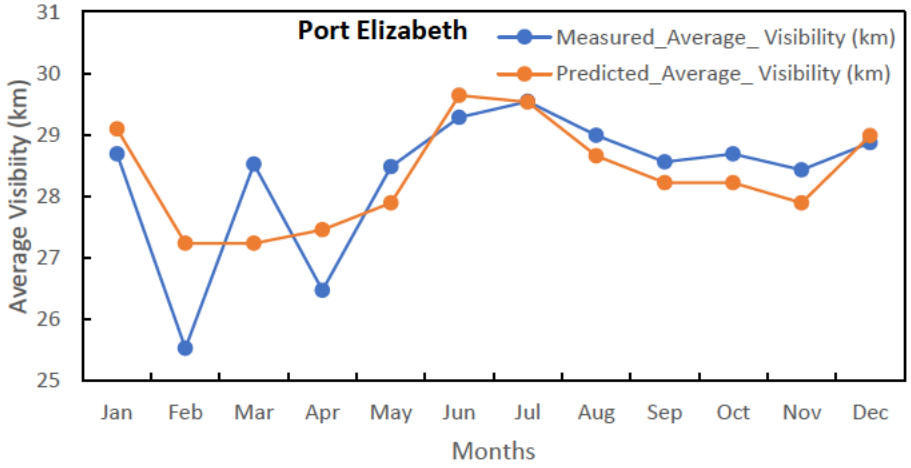

Figure 4.36 Variation between measured and forecasted mean visibility utilizing the average relative humidity regression model in Port Elizabeth, over two years.

4.3.7 Aggregative Visibility (km) versus Aggregative Wind Speed (km/h) year 2018-2019

Figures 4.37 and 4.38 display the monthly wind speed and visibility data for Cape Town and Port Elizabeth, respectively, with each figure showing a one-to-one correspondence between the two parameters over the two years from January 2018 to December 2019.

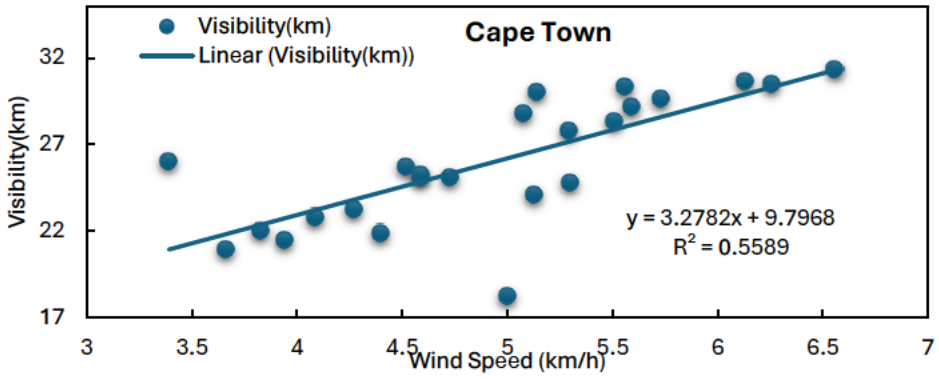

Figure 4.37 Aggregative visibility versus aggregative wind speed (m) in Cape Town over two years.

According to Figure 4.37, the recorded correlation coefficient and the standard error metrics are 0.7476 and 2.4906. The aggregate equation for estimating visibility against the corresponding wind speed is in equation (4.9):

$$V = -3.2782(Wind\ Speed) + 9.7368 \quad (4.9)$$

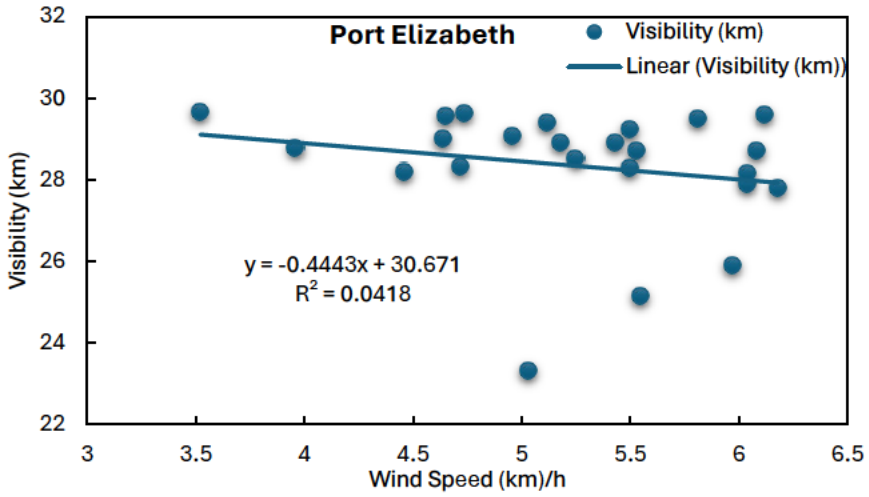

Figure 4.38 Aggregative visibility versus aggregative wind speed (m) in Port Elizabeth over two years.

In Figure 4.38, the obtained correlation coefficient is 0.2046, indicating a weak positive correlation, with a standard error of 1.5321. Consequently, the regression equation for estimating aggregate visibility against corresponding wind speed is calculated using equation (4.10):

$$V = -0.4443(Wind\ Speed) + 30.671 \quad (4.10)$$

4.3.8 Measured and forecasted visibility metrics based on aggregative wind speed regression model

Table 4.5, Figures 4.39 and 4.40 present the observed and predicted visibility metrics for Cape Town in 2018, derived from the aggregative wind speed regression model, while Table 4.6 and Figures 4.41 and 4.42 display the corresponding metrics for Port Elizabeth, also based on the aggregative wind speed regression mode.

Table 4.5 Measured and forecasted visibility metrics based on aggregative wind speed regression mode with the RMSE difference in Cape Town.

Cape Town								
Months	**Measured Maximum Wind Speed (km/h)**		**Measured Visibility (km)**		**Forecasted Visibility (km) for Wind Speed**		**RMSE (km)**	
	2018	**2019**	**2018**	**2019**	**2018**	**2019**	**2018**	**2019**
January	6.56	5.56	31.33	30.3	31.89	27.47	2.16024	2.46644
February	5.73	5.59	29.62	29.2	29.28	27.59		
March	5.29	5.3	27.79	24.8	27.89	26.49		
April	4.52	4.59	25.71	25.2	25.47	23.79		
May	3.94	3.83	21.49	22	23.65	20.91		
June	4.4	4.27	21.87	23.2	25.09	22.58		
July	3.39	5	25.98	18.2	21.92	25.35		
August	3.66	4.09	20.92	22.8	22.77	21.89		
September	4.59	4.73	25.1	25.1	25.69	24.32		
October	5.08	5.13	28.75	24.1	27.23	25.84		
November	5.51	6.13	28.34	30.6	28.59	29.64		
December	5.14	6.26	30	30.5	27.42	30.13		

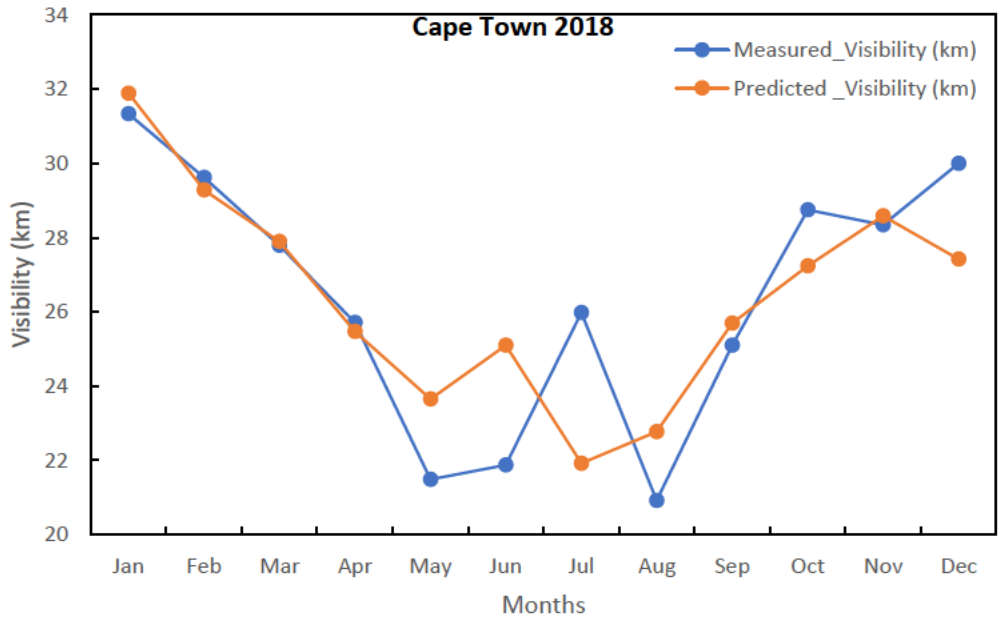

Figure 4.39 Fluctuations between measured and forecasted visibility metrics utilizing the aggregative wind speed regression model in Cape Town, in the year 2018.

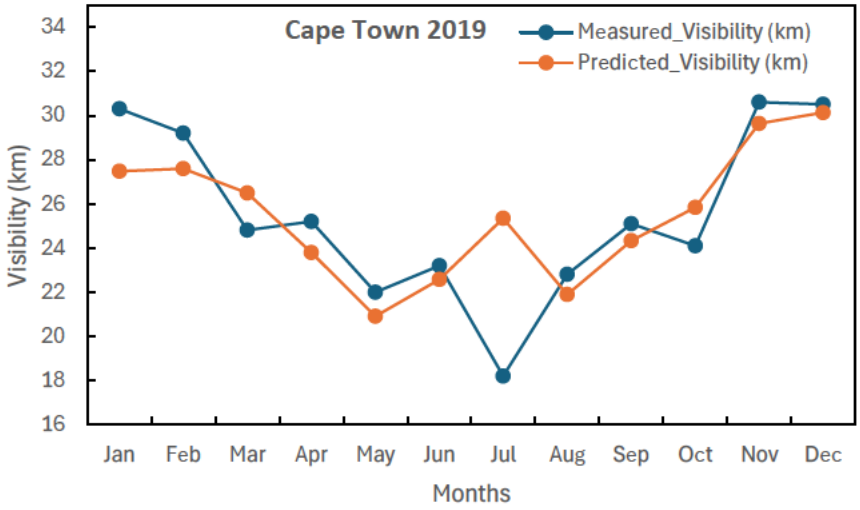

Figure 4.40 Fluctuations between measured and forecasted visibility metrics utilizing the aggregative wind speed regression model in Cape Town, in the year 2019.

Table 4.6 Measured and forecasted visibility metrics based on aggregative wind speed regression mode with the RMSE difference in Port Elizabeth.

Port Elizabeth								
Months	**Measured Maximum Wind Speed (km/h)**		**Measured Visibility (km)**		**Forecasted Visibility (km) for Wind Speed**		**RMSE (km)**	
	2018	**2019**	**2018**	**2019**	**2018**	**2019**	**2018**	**2019**
January	6.18	6.12	27.79	29.6	27.63	28.52	1.0408	1.8930
February	5.55	5.97	25.16	25.9	28.12	28.46		
March	4.72	5.53	28.33	28.7	28.77	28.28		
April	4.74	5.03	29.63	23.3	28.75	28.07		
May	3.96	4.46	28.76	28.2	29.36	27.84		
June	4.65	4.64	29.56	29	28.82	27.91		
July	3.52	5.12	29.67	29.4	29.69	28.11		
August	4.96	5.43	29.08	28.9	28.58	28.24		
September	5.5	5.18	28.27	28.9	28.16	28.13		
October	6.04	5.81	27.88	29.5	27.74	28.39		
November	6.04	6.08	28.16	28.7	27.74	28.5		
December	5.5	5.25	29.24	28.5	28.16	28.16		

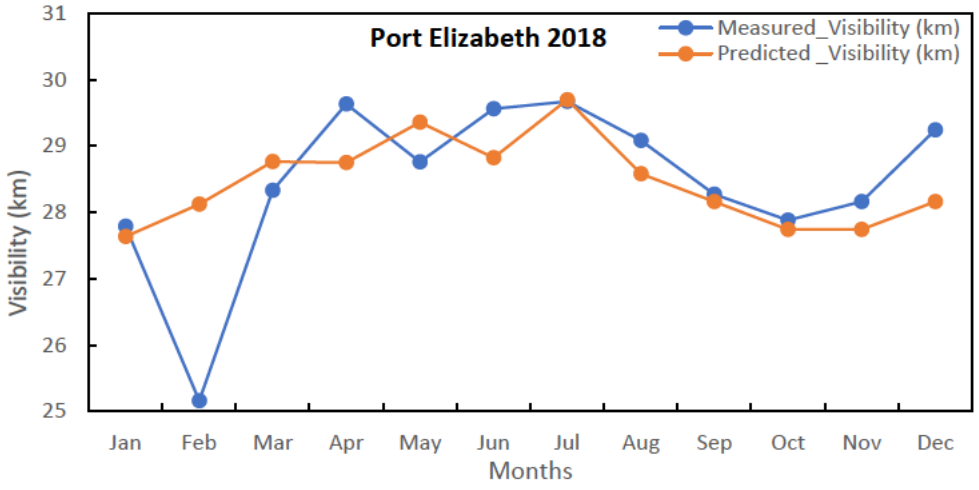

Figure 4.41 Fluctuations between measured and forecasted visibility metrics utilizing the aggregative wind speed regression model in Port Elizabeth, the year 2018.

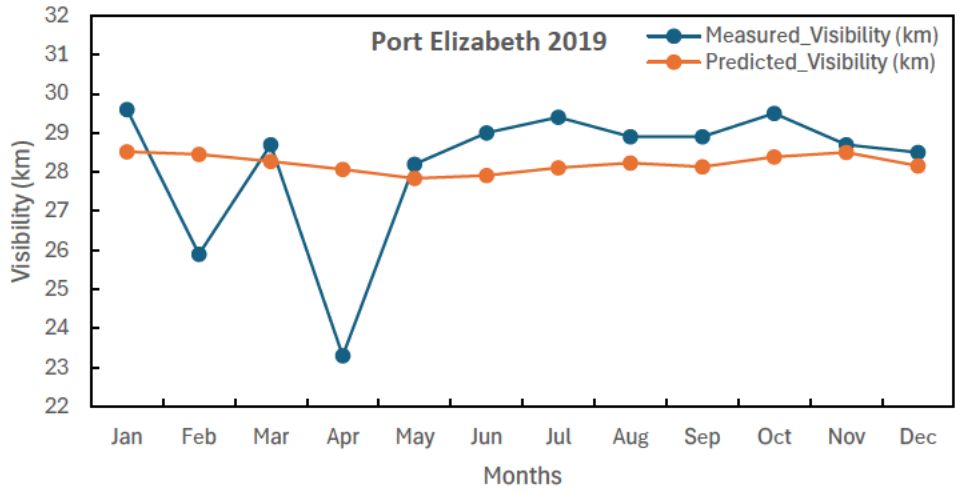

Figure 4.42 Fluctuations between measured and forecasted visibility metrics utilizing the aggregative wind speed regression model in Port Elizabeth, the year 2019.

4.3.9 Mean Visibility (km) versus Mean Wind Speed (km/h)

Figures 4.43 and 4.44 display the correlation between average monthly visibility and average wind speed values for Cape Town over two years, while Figures 4.45 and 4.46 illustrate the corresponding correlation for Port Elizabeth, showcasing the relationship between these two meteorological parameters.

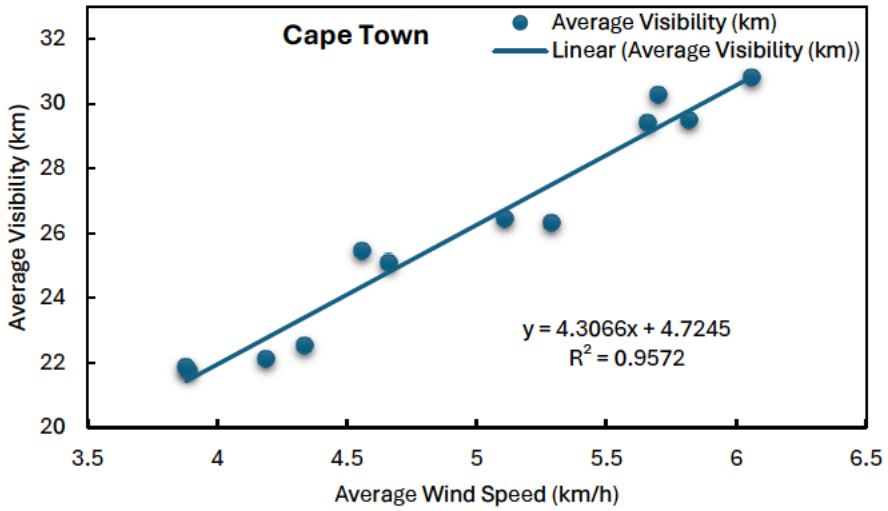

Figure 4.43 Mean visibility versus mean wind speed (km/h) in Cape Town.

In Figure 4.43, a strong positive correlation is evident, with a correlation coefficient of 0.9784 and a standard error of 0.7420. Accordingly, the regression equation for estimating average visibility against corresponding wind speed is calculated by equation (4.11):

$$V = 4.3066(Wind\ Speed) + 4.7245 \tag{4.11}$$

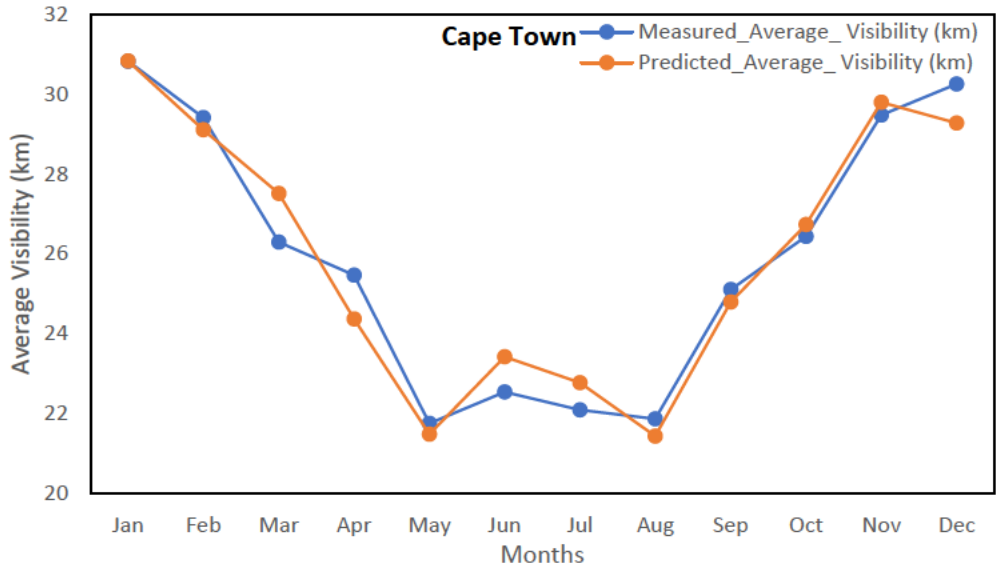

Figure 4.44 Variation between measured and forecasted mean visibility utilizing the average wind speed regression model in Cape Town, over two years.

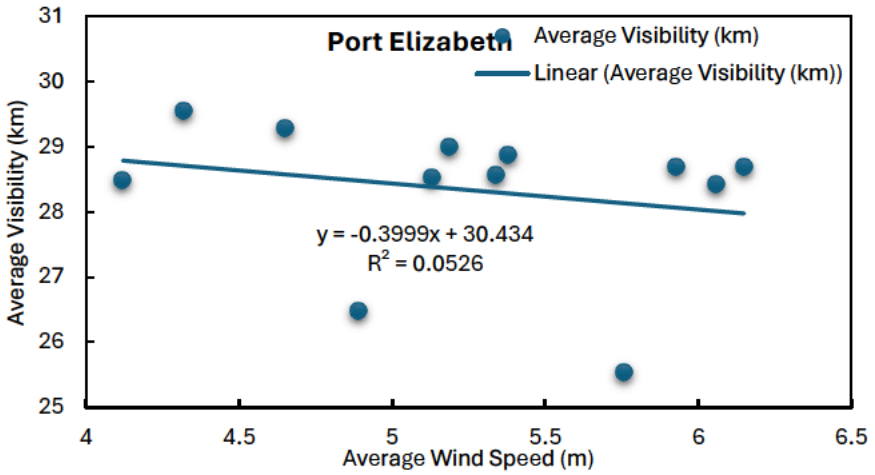

Figure 4.45 Mean visibility versus mean wind speed (km/h) in Port Elizabeth.

Figure 4.45 reveals a correlation coefficient of 0.2294, with a standard error of 1.1831, indicating a relatively weak positive relationship. The regression equation for estimating average visibility against average wind speed is thereby determined by (4.12):

$$V = -0.3999(Wind\ Speed) + 30.434 \tag{4.12}$$

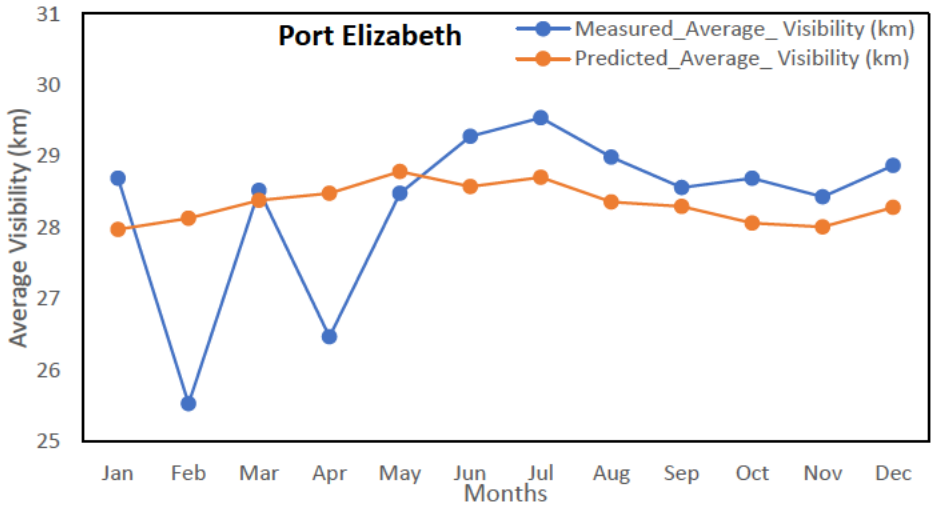

Figure 4.46 Variation between measured and forecasted mean visibility utilizing the average wind speed regression model in Port Elizabeth, over two years.

4.4 Summary

This chapter assesses visibility evaluation methods that are used for analyzing the collected meteorological data such as fog visibility, maximum temperature, relative humidity, and wind speed over two years from two coast regions in South Africa. Creating graphs to compare the visibility data between each year from each city over two years. This is followed by contrasting the visibility data of each year for each city with that of the other city. Moreover, another approach involves determining visibility through various single and multiple regression models, which are then applied to analyze the graph to detect trends, patterns, and correlations.

Chapter Five Link Performance Analysis

5.1 Introduction

This section demonstrates the impacts of different atmospheric parameters, including weather parameters, within the unique climatic parameters of selected locations, highlighting how environmental factors affect the aspect of performance and reliability of FSO technology within these distinct geographic areas. The study demonstrates the implications of atmospheric transmission on laser signal quality in these regions, exploring various scenarios that consider different turbulence strengths and visibility ranges, supported by climatic data. This analysis sheds light on the potential effects of atmospheric conditions on optical signal transmission in these specific regions. Further investigates the transmission schemes (BPSK, DPSK, and OOK) in terms of performance metrics such as average BER and achieved channel capacity. Through the impact of atmospheric conditions affecting the FSO channel, it further incorporates various models in the analysis. These models are evaluated and implemented within this chapter.

The rest of the chapter is as follows: Section 5.2 presents the FSO link availability using the climate data. The summary of the chapter is provided in Section 5.3.

5.2 FSO Link Availability Utilizing Climate Data

The attenuation characterized in this study is those induced by fog conditions because of scatterings or absorption through the atmosphere influenced by, visibility, different wavelengths, and transmission range. The attenuation was calculated, computed, and modelled through the accumulation of scattering losses. The changes in visibility influence the specific fog attenuation and therefore it is apparent that atmospheric fog attenuation is dependent on visibility. In characterizing these losses, the study evaluates selected coastal cities to figure out the viability of the FSO technology system.

5.2.1 Estimation of scattering attenuation

This section presents the findings on how the attenuation due to atmospheric parameters and scattering coefficient impact the performance of the FSO technology in the designated study regions, highlighting the effects of these factors on the system's behaviour and efficiency.

The fog-induced attenuation for the proposed locations is based on the visibility data, Mie scattering, attenuation coefficient, and the transmission range which is then assumed to be 5km for this work. This link range will provide a comparison of attenuation performance between lower to higher link range based on various operating wavelengths. The average scattering coefficients for various optical wavelengths (650, 850, 1200, and 1550 nm) are presented in Table 5.1, based on a 2% transmittance threshold and calculated using Kim's model for the two years (2018-2019). The scattering coefficient for each coastal city is estimated and modelled using (3.5), utilizing the average visibility values corresponding with the selected operating wavelengths. Equation (3.6) is applied to calculate and model the specific atmospheric attenuation for each city, as presented in Table 5.2, revealing the extent to which atmospheric conditions influence light transmission in each location.

Table 5.1 Average visibility versus scattering coefficient (1/km) throughout the study period.

Location	**Average Visibility (km)**	**Scattering coefficient at 650 nm**	**Scattering coefficient at 850 nm**	**Scattering coefficient at 1200 nm**	**Scattering coefficient at 1550 nm**
Cape Town	25.96	0.121	0.086	0.055	0.039
Port Elizabeth	28.34	0.111	0.078	0.050	0.035

Table 5.2 Average visibility versus average specific atmospheric (dB/km) attenuation

Location	**Average Visibility (km)**	**Average Specific attenuation at 650 nm**	**Average Specific attenuation at 850 nm**	**Average Specific attenuation at 1200 nm**	**Average Specific attenuation at 1550 nm**
Cape Town	25.96	2.634	1.858	1.187	0.851
Port Elizabeth	28.34	2.412	1.702	1.087	0.779

In Figure 5.1, the scattering coefficient is plotted against mean visibility in Cape Town, revealing that at an average visibility of 25.96 km, the corresponding scattering coefficients are 0.121 km^{-1} at 650 nm, 0.086 km^{-1} at 850 nm, 0.055 km^{-1} at 1200 nm, 0.039 km^{-1} at 1550 nm, respectively, indicating the variability of scattering coefficients with wavelength and visibility.

Figure 5.2 displays the correlation between atmospheric attenuation (dB/km) and average visibility (km) in Cape Town, revealing that at a visibility of 25.96 km, the attenuation values are 2.634 dB/km at 650 nm, 1.858 dB/km at 850 nm, 1.187 dB/km at 1200 nm, and 0.851 dB/km at 1550 nm, accordingly.

Figure 5.3 illustrates the relationship between atmospheric attenuation and link range, showing that at a link range of 1.11 km, the attenuation values are 0.58 dB/km at 650 nm, 0.41 dB/km at 850 nm, 0.26 dB/km at 1200 nm, and 0.19 dB/km at 1550 nm. However, when the link range increases to its maximum of 5 km, the attenuation values increase to 2.6 dB/km at 650 nm, 1.86 dB/km at 850 nm, 1.19 dB/km at 1200 nm, and 0.85 dB/km at 1550 nm, respectively.

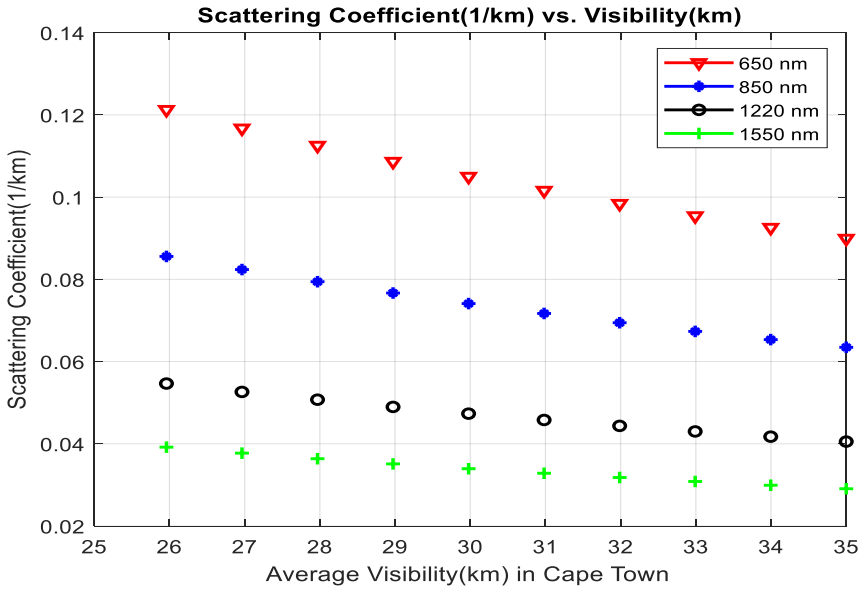

Figure 5.1 Light scattering factor (km^{-1}) against average visibility (km) for Cape Town.

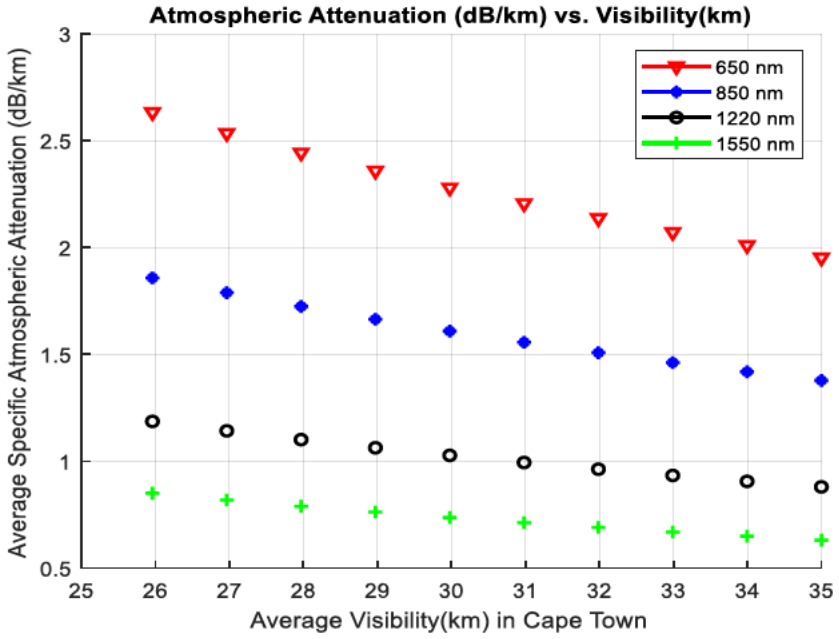

Figure 5.2 Average specific atmospheric attenuation (dB/km) against average visibility (km) in Cape Town.

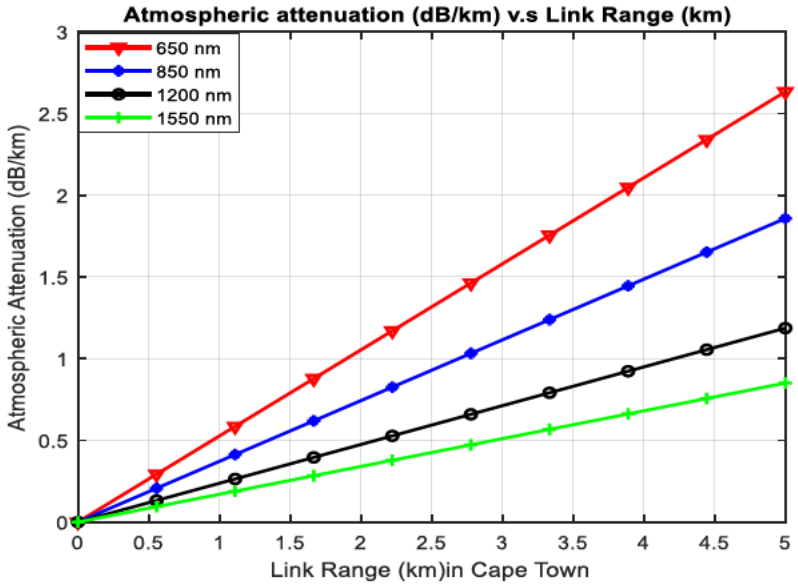

Figure 5.3 Atmospheric attenuation (dB/km) against propagation range (km) in Cape Town.

Figure 5.4 shows the correlation between the scattering coefficient and average visibility in Port Elizabeth, highlighting their relationship. The city's average visibility range is 28.34 km, and for this range, the scattering coefficients are 0.111 km^{-1} at 650 nm, 0.078 km^{-1} at

850 nm, km-^{1} at 1200 nm, and 0.036 km-^{1} at 1550 nm, respectively, demonstrating the dependence of scattering coefficients on visibility and wavelength.

Figure 5.5 illustrates the correlation between specific atmospheric signal losses (dB/km) and average visibility (km) in Port Elizabeth, showing that at average visibility of 28.34 km, the specific atmospheric attenuation values are 2.412 dB/km at 650 nm, 1.702 dB/km at 850 nm, 1.087 dB/km at 1200 nm, and 0.779 dB/km at 1550 nm, respectively, indicating the dependence of atmospheric attenuation on wavelength and visibility.

Figure 5.6 shows the relationship between atmospheric attenuation and transmission range up to 5 km in Port Elizabeth. At a range of 1.11 km, the attenuation values are 0.546 dB/km at 650 nm, 0.318 dB/km at 850 nm, 0.242 dB/km at 1200 nm, and 0.173 dB/km at 1550 nm. However, at the maximum transmission range of 5 km, the attenuation values increase to 2.412 dB/km at 650 nm, 1.702 dB/km at 850 nm, 1.087 dB/km at 1200 nm, and 0.779 dB/km at 1550 nm, respectively, demonstrating the impact of transmission link range on atmospheric attenuation.

This section evaluated the effects of scattering coefficient and atmospheric attenuation on the FSO link performance within the two coastal cities. There is a correlation between the transmission range extending between 0 km to 5 km and the visibility range. An observed regional visibility variation between Cape Town and Port Elizabeth exhibits different visibility ranges. Cape Town had achieved a low visibility of 25.96 km, followed by Port Elizabeth, with a visibility of 28.34 km. Therefore, considering these visibility variations can ensure optimal performance. Port Elizabeth maintained better scattering coefficient and atmospheric attenuation than Cape Town because each visibility range can impact FSO link performance differently.

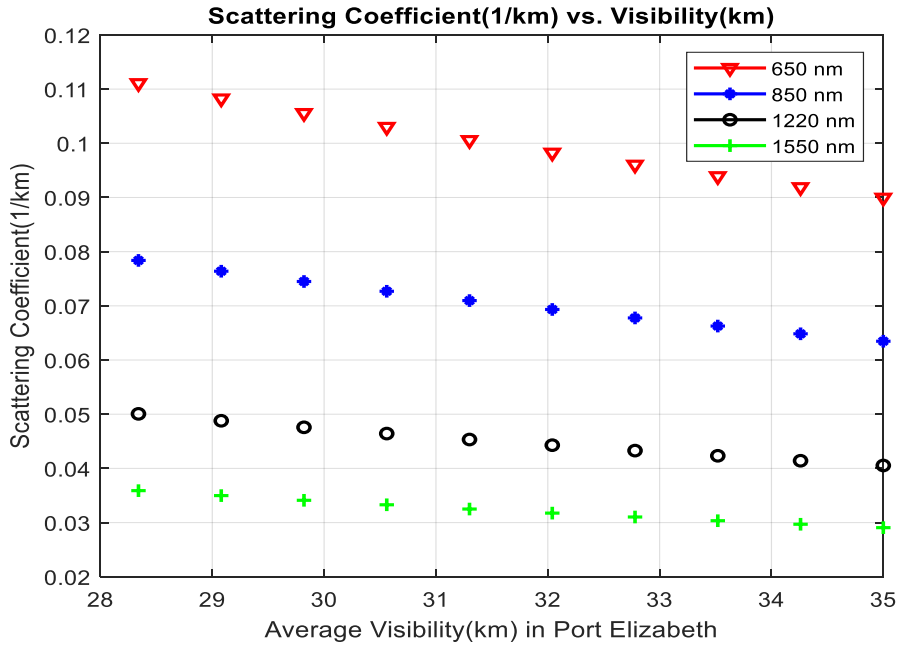

Figure 5.4 Scattering coefficient (1/km) against average visibility (km) in Port Elizabeth.

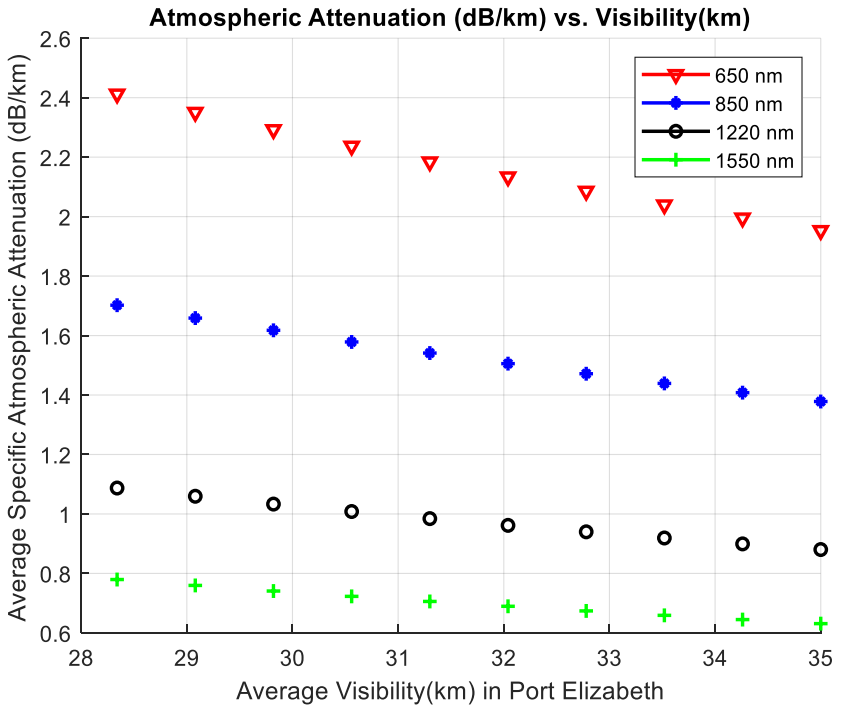

Figure 5.5 Average atmospheric attenuation (dB/km) against average visibility (km) in Port Elizabeth.

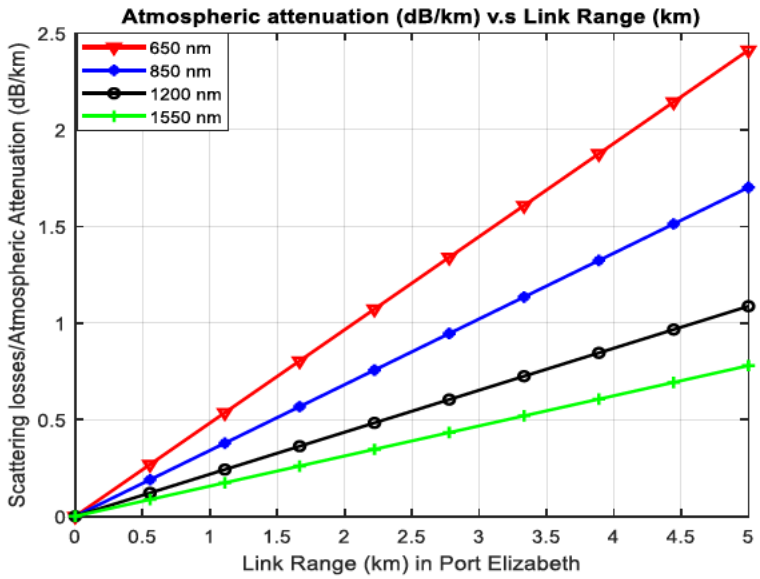

Figure 5.6 Atmospheric attenuation (dB/km) against propagation range (km) in Port Elizabeth.

5.2.2 Reflective index structure parameter (RISP)

Two years of mean wind speed (km/s) and altitude data from the identified locations have been used to compute and obtain the RISP values, C_n^2 by utilizing the Hufnagel-Valley model in (3.14). Thus, the results are provided and tabulated in Table 5.3 for each city. It is observed that while having a constant RISP, and when the propagation link distance between the receiver and the transmitter is varied, Rytov variance (σ_I^2) measures the signal fading strength, accordingly, including the atmospheric instability losses known as the scintillation index. The locations have recorded the strong turbulences according to RISP value as seen in Table 5.3, and this is measured through the Rytov variance. According to equations (2.3) and (2.4) Rytov variance depends on RISP. Therefore, this requires the link distance to be reduce from 5km to at 3.5 km.

Table 5.3 Wind speed, Altitude, RISP, Rytov variance.

Location	Wind speed (km/s)	Altitude (m)	RISP ($m^{-2/3}$)	(σ_I^2) at 1.5 km	(σ_I^2) at 2.5 km	(σ_I^2) at 3.5 km
Cape Town	4.93	42	1.143×10^{-14}	0.48	1.22	2.26
Port Elizabeth	5.29	85	7.521×10^{-15}	0.31	0.80	1.49

Table 5.4 Wind speed, Altitude, RISP, scintillation index.

Location	**Wind speed (km/s)**	**Altitude (m)**	**RISP ($m^{-2/3}$)**	**Scintillation index (dB) at 1.5 km**	**Scintillation index (dB) at 2.5 km**	**Scintillation index (dB) at 3.5 km**
Cape Town	4.93	42	$1.143x10^{-14}$	0.51	0.67	0.42
Port Elizabeth	5.29	85	$7.521x10^{-15}$	0.34	0.69	0.60

5.2.3 Average BER Versus SNR

The average BER in terms of average SNR was computed for both cities over different modulation schemes, considering the parameters in Table 5.3 and Table 5.4. For this analysis, the effects of wind speed, and altitude are assumed through equation (3.14), and the effect of atmospheric turbulences and fog conditions were assumed by applying equation (3.26), taking into consideration other parameters such as the propagation, signal fading strength as discussed above. Thus, the average system error performance of the SIM FSO link is modeled using the gamma-gamma distribution channel model, as described by (3.27). This model takes into account the effects of path loss and atmospheric turbulence on the average SNR, which in turn affects the FSO link BER performance.

To accurately estimate the system's error performance in the Western Cape region, the atmospheric fading strength was observed to range as $\emptyset_R^2 = 0.48$ (weak fading), $\emptyset_R^2 = 1.22$ (moderate fading) and $\emptyset_R^2 = 2.26$ (strong fading). This range of fading strengths was achieved by adjusting the propagation link range (L) to 1500 m, 2500 m, and 3500 m, respectively, allowing for the simulation of different fading regimes. The impact of turbulence-induced signal fading on the system's performance is assessed using the calculated C_n^2 values, which remain constant across the city for each link distance. These values are used to estimate the average BER performance of the system at a laser wavelength $\lambda = 1550$ nm, providing insights into the system's reliability and accuracy.

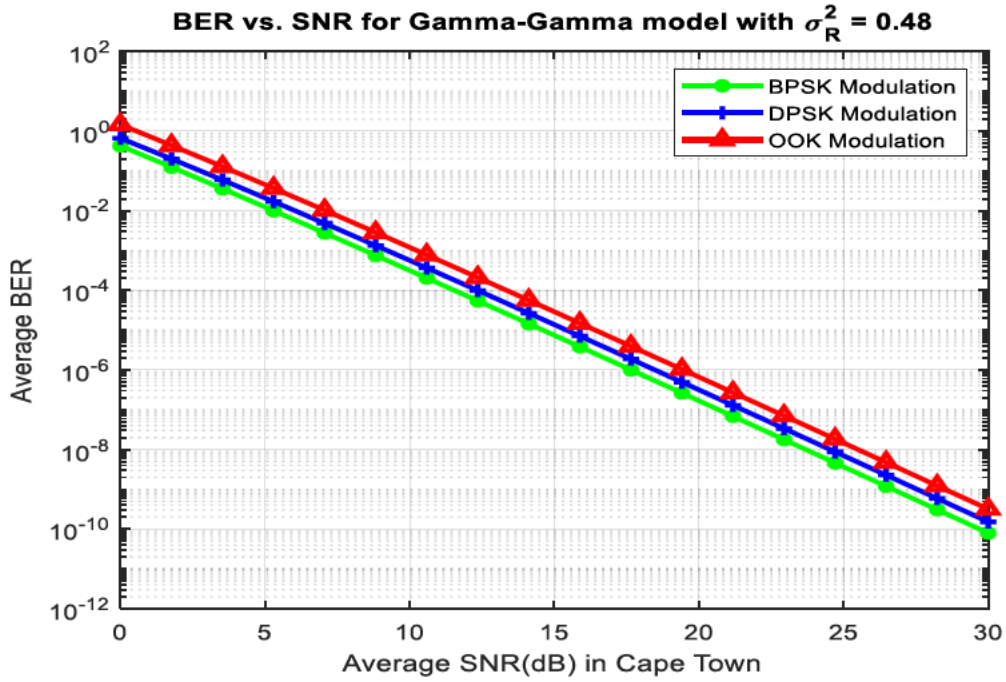

Figure 5.7 Average BER against SNR under weak fading strength at 1.5 km in Cape Town.

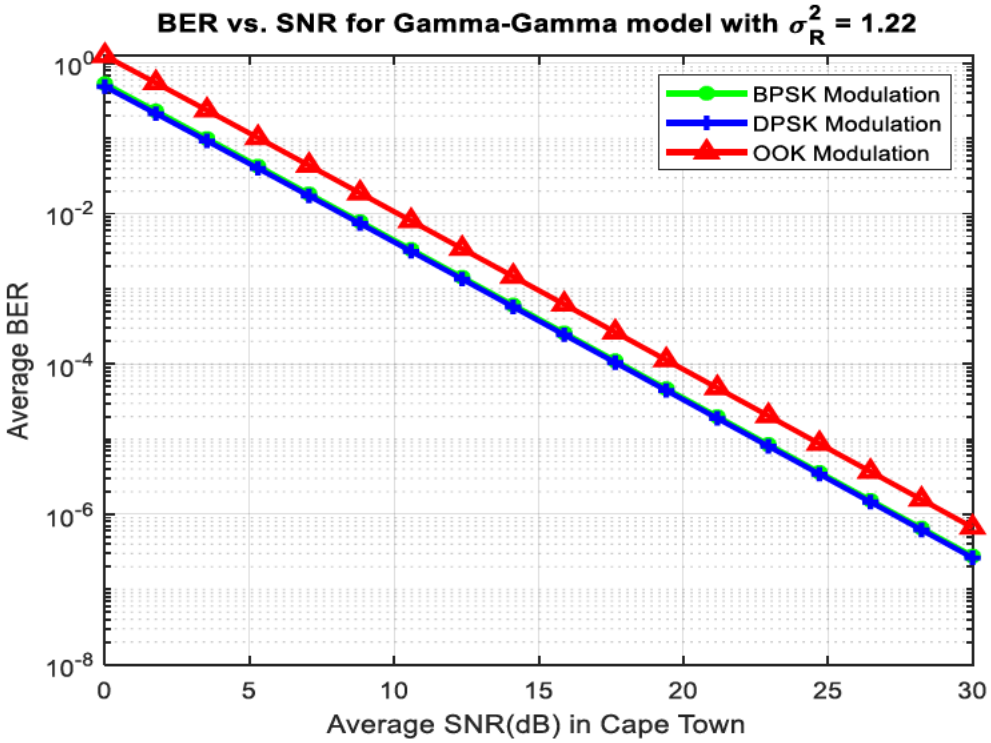

Figure 5.8 Average BER against SNR under moderate fading strength at 2.5 km in Cape Town.

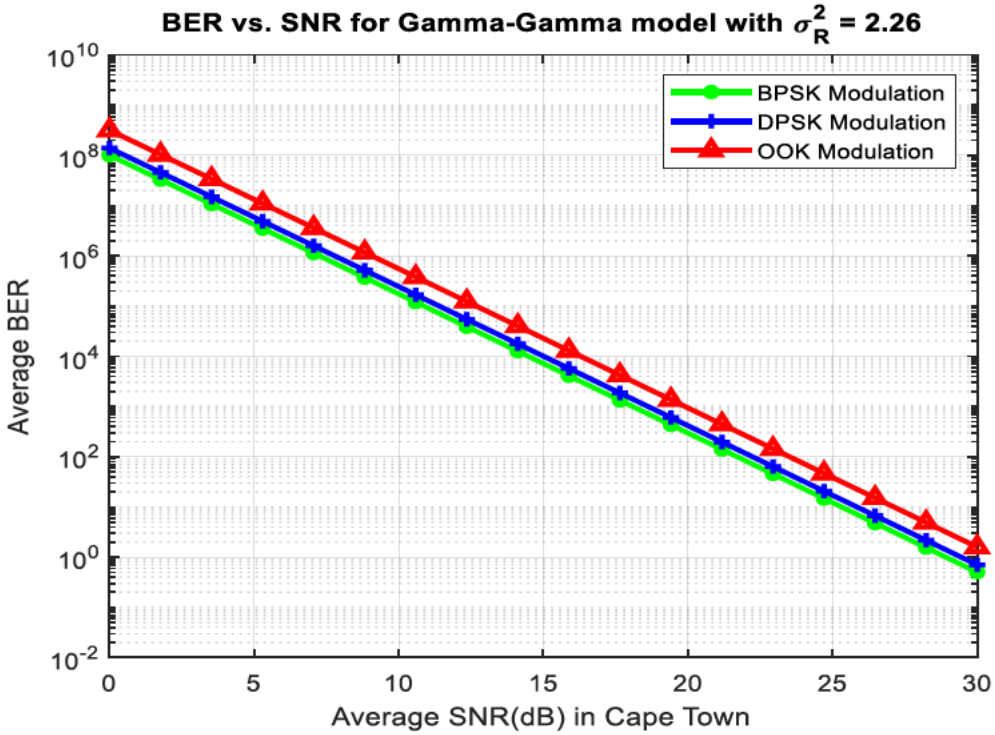

Figure 5.9 Average BER versus SNR under strong fading strength at 3.5 km in Cape Town.

In Port Elizabeth, the same approach was applied, and the signal fading strength was observed to range from $\emptyset_R^2 = 0.31$ (weak fading), $\emptyset_R^2 = 0.80$ (moderate fading) and $\emptyset_R^2 = 1.49$ (moderate fading). By adjusting the propagation link range (L) to 1500 m, 2500 m, and 3500 m, the regime of weak to moderate fading strength was achieved, allowing for the assessment of the system's performance under varying conditions.

In conclusion, a comparative error performance analysis was carried out on three different modulation schemes to determine the viability of link performance. Theoretical studies showed that BPSK outperformed other modulation formats, emerging as the most dependable and efficient transmission technique in both cities. Specifically, BPSK consistently produces a reduced average BER, substantially minimizing the adverse effects of weather conditions and atmospheric turbulence, especially during periods of weak fading.

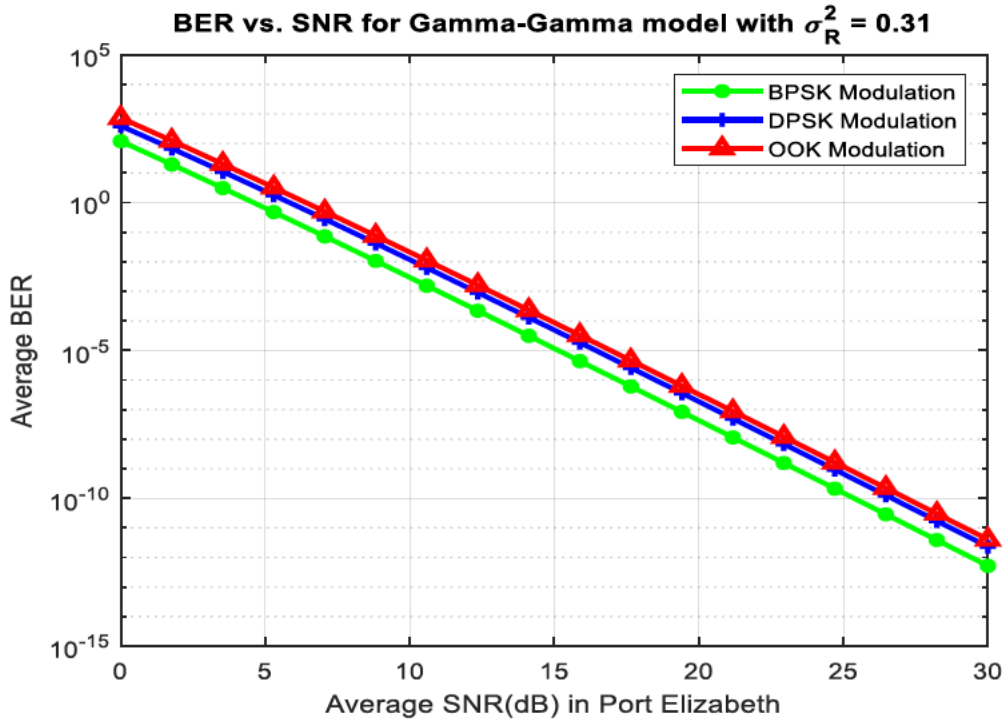

Figure 5.10 Average BER against SNR under weak fading strength at 1.5 km in Port Elizabeth.

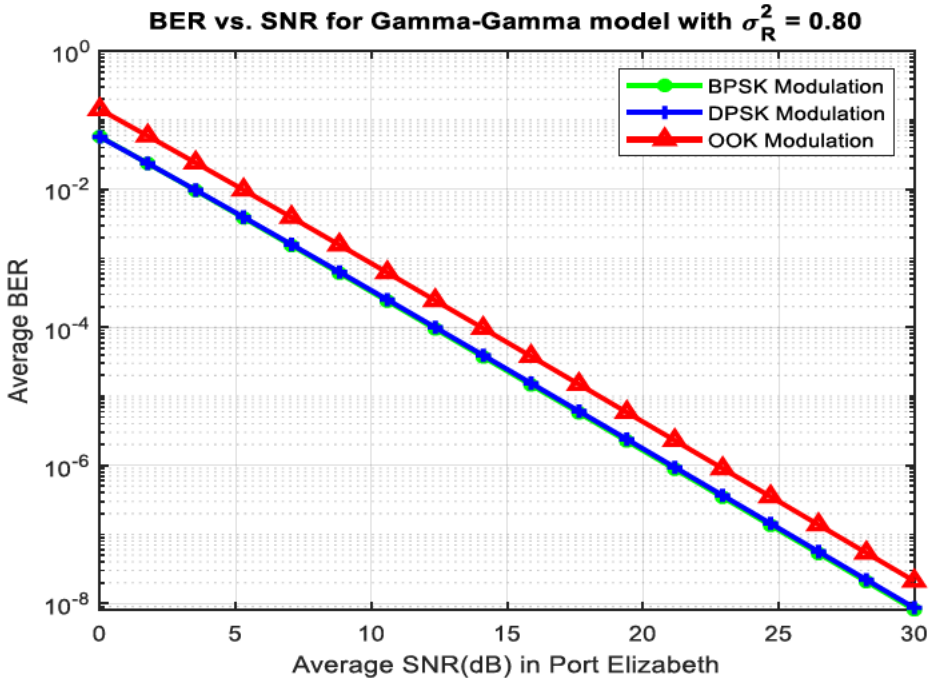

Figure 5.11 Average BER against SNR under moderate fading strength 2.5 km in Port Elizabeth.

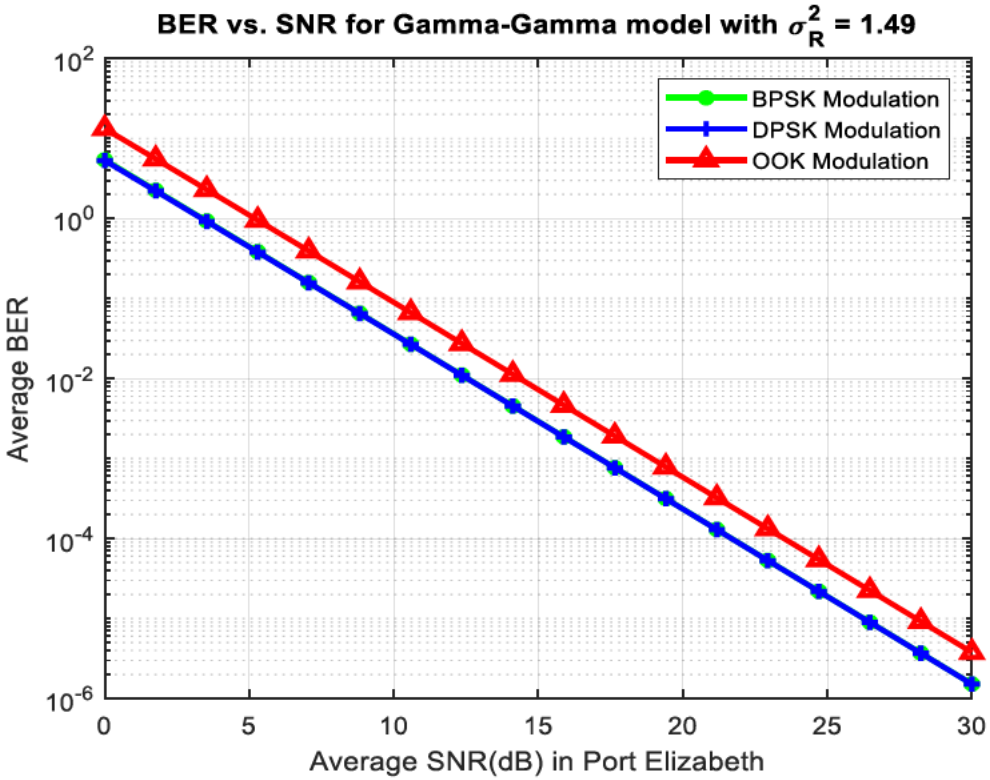

Figure 5.12 Average BER against SNR under moderate fading strength at 3.5 km in Port Elizabeth.

5.2.4 Average channel capacity for various modulation schemes

In this section, the average channel capacity (ACC) was computed in terms of the average SNR considering the turbulence strength that each city contributed over different link ranges of 1.5 km, 2.5 km, and 3.5 km. These results align with [114] demonstrating a decline in ACC as the turbulence strength transitions from weak to strong and it was observed that the same applies when the signal fading strength transitions from weak to strong fading strength. Instead, the turbulence strength in Cape Town is moderate and that of Port Elizabeth is weak, thus the channel capacity observed in Port Elizabeth is much larger than the channel capacity in Cape Town in all the propagation link ranges. Therefore, the channel capacity is influenced by climate conditions and instability in the atmospheric. Furthermore, the channel capacity shows an improvement with the increase in the average SNR.

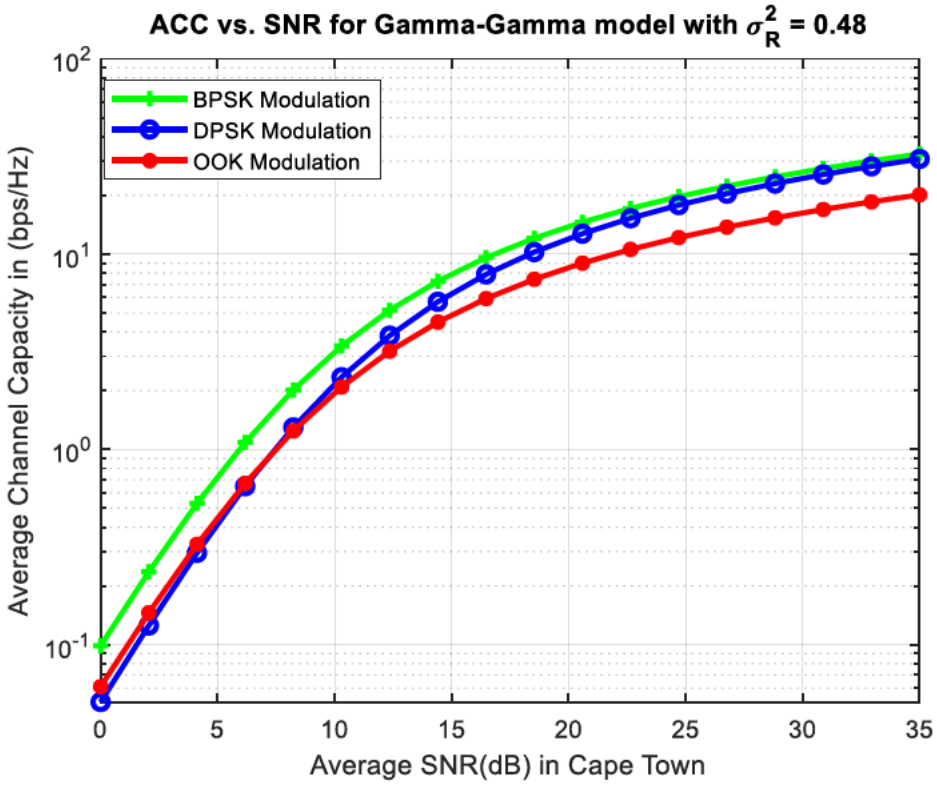

Figure 5.13 ACC against SNR under weak fading strength at 1.5 km in Cape Town.

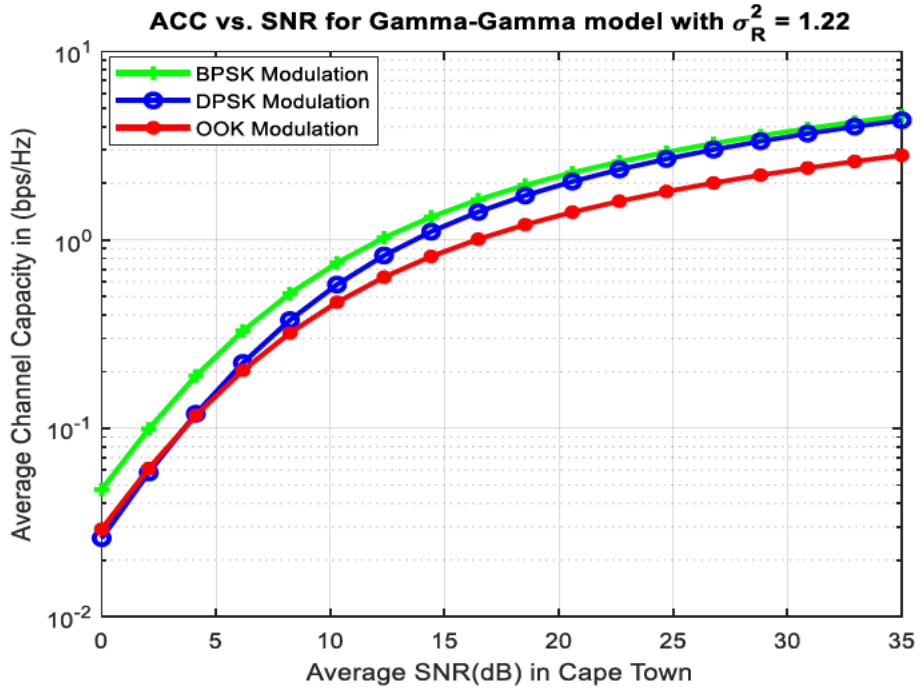

Figure 5.14 ACC against SNR under moderate fading strength at 2.5 km in Cape Town.

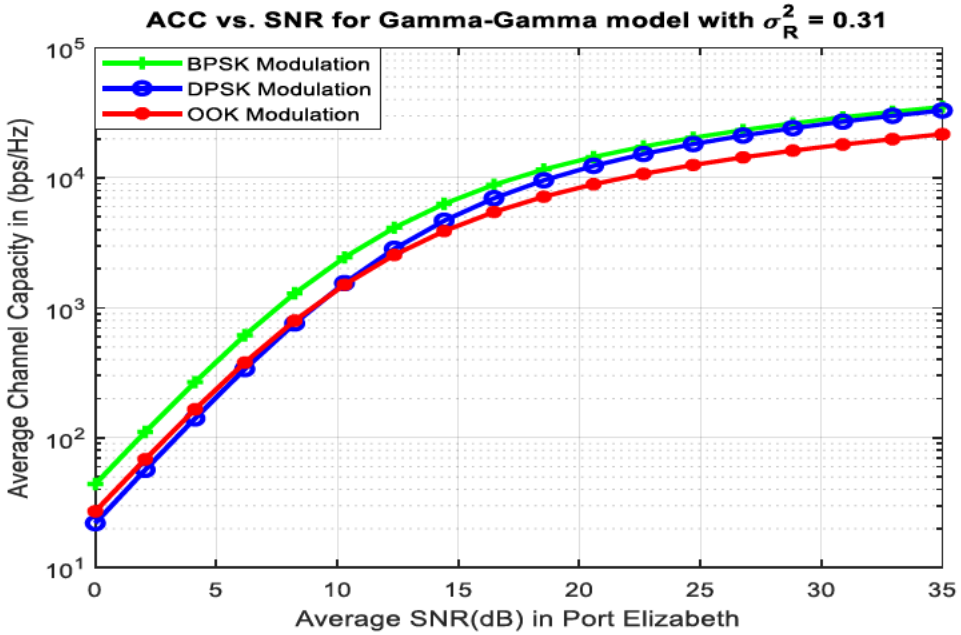

Figure 5.15 ACC against SNR under weak fading strength at 1.5 km in Port Elizabeth.

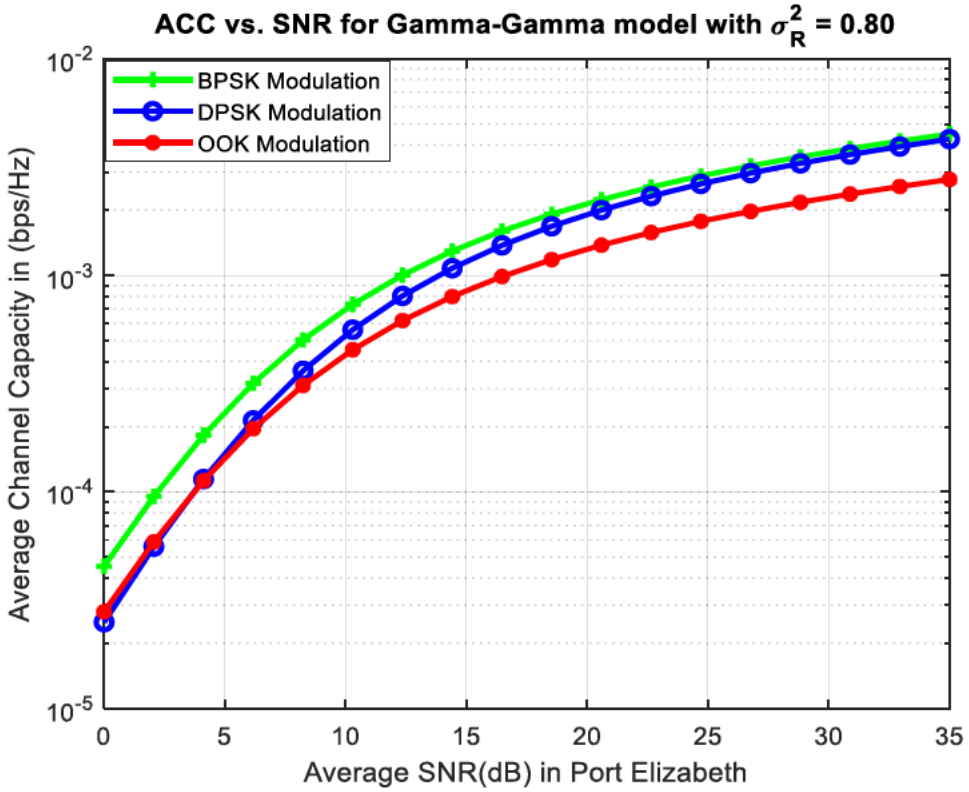

Figure 5.16 ACC against SNR under moderate fading strength at 2.5 km in Port Elizabeth.

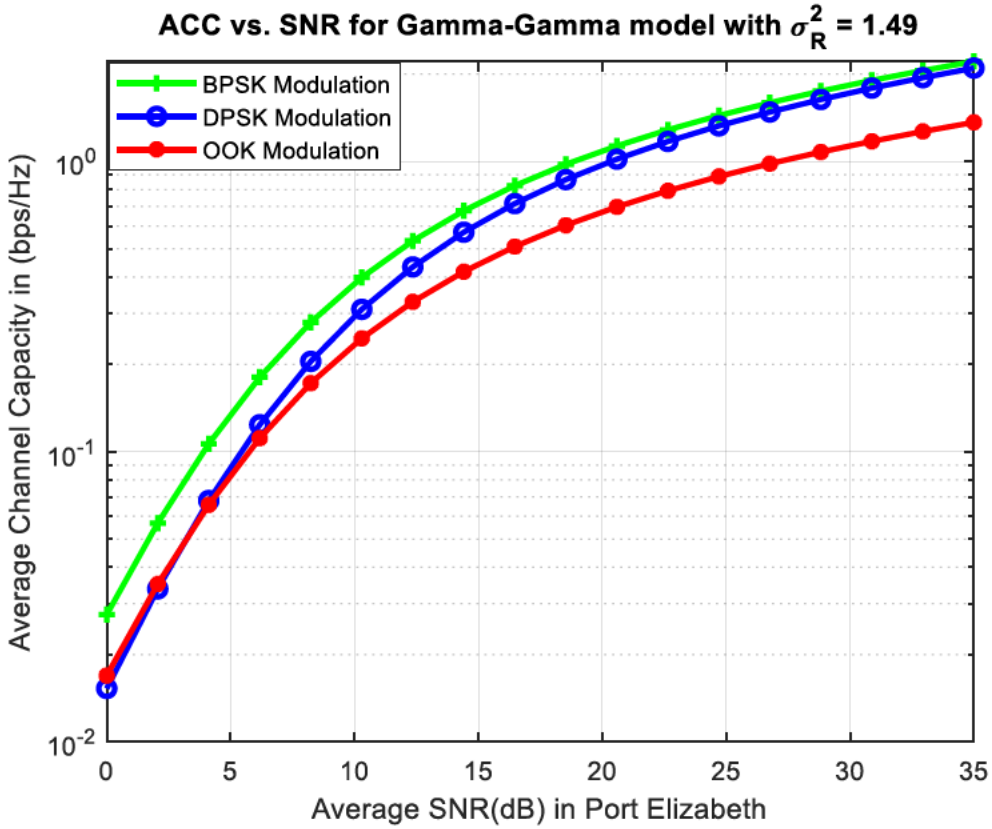

Figure 5.17 ACC against SNR under moderate fading strength at 3.5 km in Port Elizabeth.

5.3 Summary

The influence on fog-induced attenuation based on various operating wavelengths was considered using KIM's model. Demonstrating the results during the presence of the aerosol scattering attenuation against the average visibility obtained from the identified locations. The assessment of signal attenuation considers the chosen operating wavelength, visibility conditions, and a minimum transmission distance of 5 km. Furthermore, the FSO system performance is based on the various transmissions (BPSK, DPSK, and OOK) was conducted considering performance metrics such as average channel capacity and BER.

Chapter Six Conclusions and Recommendations

6.1 Introduction

As wireless communications and applications continue to be relevant in new technologies, FSO and its applications will also continue to be relevant in the telecommunication world. This section provides a summary of the conclusions drawn from the previous chapters of this work. It highlights the key findings and their implications for the field of FSO communication.

6.2 Visibility

Each operating wavelength is influenced differently by the fog particles in the atmosphere, these particles scatter shorter wavelengths more efficiently than longer wavelengths, contributing to higher attenuation at shorter wavelengths.

Port Elizabeth experienced the highest visibility, reaching approximately 28.34 km over two years, with corresponding average attenuations of 2.412 dB/km at the wavelengths of 650 nm, 1.702 dB/km at the operating spectral wavelengths of 850 nm, 1.087 dB/km at the wavelengths of 1200 nm, and 0.779 dB/km at the wavelengths of 1550 nm, as indicated in Table 5.2. It is thus observed that the operating spectral wavelength influences keeping a minimal fog attenuation, as it seems to be inversely proportional to the fog attenuation. The estimated average attenuation reduces by 29.44% when the operating spectral wavelength rises from 650 nm to 850 nm, by 54.93% when the operating spectral wavelength rises from 650 nm to 1200 nm, and by 67.70% when the operating spectral wavelength rises from 650 nm to 1550 nm.

Cape Town has recorded the lowest average visibility of about 25.96 km with an average attenuation of 2.634 dB/km at 650 nm, 1.858 dB/km at 850 nm, 1.187 dB/km at 1200 nm, and 0.851 dB/km at 1550 nm accordingly. Notable, the average attenuation has declined by 29.46% from 650 nm to 850 nm, by 54.94 % between 650 nm to 1200 nm, and by 67.69% from 650 nm to 1550 nm, indicating a substantial reduction in attenuation as the wavelength increases.

The influence of the scattering coefficient over the visibility of each city has been observed and tabulated in Table 5.1. Based on the recorded data it is obvious that Cape Town has the highest scattering due to its lowest visibility. It is then deduced that based on the recorded data the higher the visibility the smaller the scattering coefficient, and the higher the operating wavelength the smaller the fog attenuation.

6.3 Average BER versus SNR

The results have revealed a degradation in system error performance and link availability as the link distance increases, which can be attributed to several factors. These factors combined lead to a decline in system performance and link availability as the link distance increases, making it more challenging to maintain reliable connections over longer ranges.

i. Attenuation: As the distance increases, the signal strength weakens due to absorption and scattering by the atmosphere, leading to higher attenuation.
ii. Noise accumulation: Longer distances mean more opportunity for noise to accumulate, degrading SNR and increasing errors.
iii. Interference: Increased distance can lead to higher interference from other sources, further degrading the signal quality.
iv. Dispersion: Signals spread over longer distances, causing dispersion, which can lead to intersymbol interference and errors.
v. Atmospheric effects: Weather conditions like fog, haze, or smoke can worsen with distance, impacting signal transmission.

Therefore, as discussed in Section 5.2, the σ_l^2 and the scintillation index were observed by adjusting the propagation link between the receiver and the transmitter, however, the altitude of the location has a great influence on either of the two parameters. Instead, Cape Town has the lowest altitude thus resulting in the highest scintillation index as well as high Rytov variance values. Significantly, lower scintillation index and Rytov variance values are recorded in Port Elizabeth with the highest altitude regardless of the transmission link range.

Furthermore, Port Elizabeth has experienced the highest average wind speed of 5.29 km/h, with the highest altitude thus contributing to a value of 7.521×10^{-15} $m^{-2/3}$ as RISP which can

be categorized to be under weak atmospheric turbulence strength regime, while Cape Town experienced the lowest average wind speed of 2.93 km/h with the lowest altitude and thus recording an RISP value of 1.143×10^{-14} $m^{-2/3}$ which can be categorized as moderate turbulence strength regime. These observations are recorded in Tables 5.3 and 5.4, respectively.

Figures 5.7 to 5.9, demonstrate how the average BER of the SIM-FSO link changes with increasing average electrical SNR, under the effects of atmospheric turbulence and weather-related path losses in the Western Cape region, as simulated using the Gamma-Gamma distribution channel model. Figures 5.10 to 5.12 show that as the transmission link range increases from 1500 m to 3500 m in the Eastern Cape region, the signal fading strength becomes more pronounced, transitioning from weak to strong fading conditions.

Although the system's performance deteriorates with longer transmission link ranges in both cities, FSO technology can provide a vast, unregulated bandwidth, supporting data rates of 100 Gbit/s over distances of 1km - 4 km, as reported in [19]. The analysis reveals that, in both cities, the signal fading strength (σ_l^2) increases from weak to strong as the link range is extended, suggesting a deterioration in signal quality with increasing distance. Nevertheless, Port Elizabeth has recorded a better system error performance during all three different link ranges, compared to Cape Town. This improved performance is due to its RISP which recorded a weak atmospheric turbulence strength whereas Cape Town recorded a moderate atmospheric turbulence strength. Thus, to mitigate the influence of atmospheric turbulences and weather conditions in Cape Town, the propagation link between the receiver and the transmitter must be kept smaller. According to Figure 5.9. there is a significant degradation in system performance at the maximum link range of 3.5 km, regardless of the evaluated modulation transmission schemes.

Now, the viability of the transmission range is further assessed in consideration of atmospheric turbulence and weather conditions to determine the most effective modulation scheme in enhancing the system's performance and mitigating the impacts of environmental factors. At the shortest propagation link range of 1500 m, the results show a notable fading strength, classified as weak signal fading strength, in both cities, as depicted in Figure 5.7

for Cape Town and Figure 5.12 for Port Elizabeth, indicating a significant impact of fading on the signal even at this relatively short distance. At the mean SNR of 30 dB in Cape Town, the achievable mean BER is approximately 7.940×10^{-11} for BPSK, 1.520×10^{-10} for DPSK, and 3.175×10^{-10} for OOK, indicating the relative performance of each modulation scheme in terms of error probability. In Port Elizabeth for the same average SNR of 30 dB, the achievable average BER is approximately 5.184×10^{-13} for BPSK, 2.309×10^{-13} for DPSK, and 4.041×10^{-12} for OOK, indicating the relative performance of each modulation scheme in terms of error probability in this region.

With the transmission length increased to 2.5 km and an average SNR kept at 30 dB, the average BER is approximately 2.784×10^{-7} for BPSK, 2.630×10^{-7} for DPSK, and 6.677×10^{-7} for OOK in Cape Town. This is shown in Figure 5.2, where the signal fading strength is moderate. DPSK further demonstrates improved error performance, with a negligible error difference of 1.54×10^{-8} compared to BPSK, making it a viable alternative. However, in Port Elizabeth, the average BER is approximately 8.078×10^{-9} for BPSK, 8.637×10^{-9} for DPSK, and 2.110×10^{-8} for OOK respectively, as shown in Figure 5.5, where the signal fading strength is moderate. This indicates a relatively low error rate for all three modulation schemes in this region.

Furthermore, with an increase in link distance to 3.5 km, the system error performance further increases, especially in Cape Town compromising the link availability altogether for all the transmission schemes as seen in Figure 5.3. However, with the signal fading strength remaining at moderate in Port Elizabeth as shown in Figure 5.6 the observed mean BER is approximately 1.522×10^{-6} for BPSK, 1.514×10^{-6} for DPSK, and 3.782×10^{-6} for OOK. Notably, under moderate fading conditions, DPSK has demonstrated superior performance, achieving comparable error performance to BPSK, with a negligible error difference of 8×10^{-9} at an SNR of 30 dB. This underscores DPSK's robustness in mitigating the effects of fading, making it a viable option for reliable data transmission.

The results indicate that BPSK significantly outperforms OOK and DPSK in terms of system error performance, particularly under weak signal fading conditions in both Cape Town and Port Elizabeth. This suggests that BPSK is a more efficient modulation scheme in mitigating

the effects of fading, leading to improved error performance in these scenarios. Nevertheless, the trend shifts during moderate fading strength, especially in Port Elizabeth, where DPSK demonstrates enhanced system performance, outperforming BPSK and OOK. This indicates that DPSK is more effective in mitigating the effects of moderate fading, making it a preferred modulation scheme in these conditions.

The results reveal that the system error performance of BPSK is significantly better than that of OOK and DPSK, particularly in conditions of weak signal fading strength in both Cape Town and Port Elizabeth. This indicates that BPSK is more resilient to signal fading and offers improved error performance in these scenarios. However, the situation reverses during moderate signal fading strength, particularly in Port Elizabeth, DPSK exhibits improved system performance and outperforms Binary BPSK and OOK. This suggests that DPSK is more suitable for conditions of moderate signal fading, offering better error performance in these scenarios. Additionally, the data shows an inverse relationship between SNR and BER, where an increment in average SNR leads to a reduction in average BER. This suggests that enhancing the signal strength relative to noise results in improved error performance, highlighting the importance of SNR in ensuring reliable data transmission.

6.4 Average Channel Capacity versus SNR Discussion

Figures 5.7 and 5.8 depict the achievable ACC as the function of the SNR of the FSOC system modeled with the Gamma-Gamma distribution channel model, subjected to signal loss due to atmospheric conditions and fog-induced loss for the Western Cape region and so is Figures 5.9 to 5.11 for the Eastern Cape Region, respectively. It is worth noting that the ACC declines as the fading strength transitions from weak to moderate fading strength. Furthermore, the ACC increases significantly with the average SNR irrespective of the changes in the fading strength. According to [23] the acceptable communication BER is $1x10^{-9}$ hence the achievable channel capacity for Cape Town at 3.5 km is not demonstrated because the communication link is not feasible within this range. This is also the case when the channel has a stronger atmospheric turbulence parameter and based on the data analyzed Cape Town has stronger turbulences compared to Port Elizabeth thus a shorter propagation range should be considered.

Furthermore, the average channel capacity is evaluated based on atmospheric turbulence and weather conditions to identify the modulation scheme that can achieve a better channel capacity. Therefore, based on the observed simulated results at the lowest transmission link range of 1.5 km and at an average SNR of 35 dB, BPSK, DPSK, and OOK, and the AAC achieved for Cape Town is approximately 32.613 bps/Hz, 30.726 bps/Hz, and 20.117 bps/Hz under weak fading strength as observed in Figure 5.7 whilst it is 351.505 bps/Hz, 329.845 bps/Hz, and 216.826 bps/Hz for Port Elizbeth as observed in Figure 5.9.

Nevertheless, when the same average SNR value with the propagation link increased to 2.5 km the achieved ACC for BPSK, DPSK, and OOK is 4.559 bps/Hz, 4.320 bps/Hz, and 2.812 bps/Hz, observed under moderate signal fading strength as shown in Figure 5.8 for Cape Town. However, for the same fading strength in Port Elizbeth, an achieved ACC for BPSK, DPSK, and OOK is 44.928 bps/Hz, 42.568 bps/Hz, and 27.714 bps/Hz, as seen in Figure 5.5.

As the link range is further adjusted to 3.5 km, specifically for Port Elizbeth under the same average SNR value, as the fading signal strength remains moderate, the achieved ACC for BPSK, DPSK, and OOK is 2.12 bps/Hz, 2.098 bps/Hz, and 1.364 bps/Hz. During all the observations it was noted that at the lowest SNR regions, DPSK achieves an ACC that is approximately and comparable to that of OOK, while at the high SNR region, the DPSK achieves an ACC that is approximately and comparable to that of the BPSK transmission format. Amongst the three transmission schemes, BPSK has achieved higher channel capacity in both locations. The observed better performance for channel capacity in Port Elizbeth owes to its metrological data that contributed to the lowest atmospheric turbulence strength and invariably that contributes a major effect compared to Cape Town, therefore the meteorological parameter variation within the transmission path results in variation in the refractive index based on the location. Thus, both cities do have a feasibility FSO link performance, but it does differ with location indeed. Furthermore, it can be deduced that BPSK channel capacity performance is much better than DPSK and OOK transmission schemes thus it can resist the effects of weather conditions and atmospheric turbulence.

6.5 Recommendations

Due to the rapid expansion of communication, it is recommended that additional research be conducted on the following topics:

- Adopt BPSK modulation scheme: Considering its superior performance in mitigating weather-related impairments and achieving lower average BER.
- Optimize link parameters: Further optimize link parameters, such as transmit power, receiver sensitivity, and antenna gain, to improve link performance and reliability.
- Implement diversity techniques: Consider implementing diversity techniques, such as spatial diversity or frequency diversity, to further improve link reliability and robustness.
- Conduct site-specific analysis: Perform site-specific analysis to determine the optimal link configuration and modulation scheme for each location.
- Monitor weather conditions: Continuously monitor weather conditions to anticipate and prepare for potential link outages or performance degradation.
- Develop maintenance schedules: Establish regular maintenance schedules to ensure link equipment is functioning correctly and optimize link performance.
- Develop predictive models: Develop predictive models to forecast link performance and reliability based on weather conditions and other environmental factors.
- Examine the impact of atmospheric phenomena: Investigate the impact of atmospheric phenomena, such as fog, haze, or atmospheric turbulence, on FSO link performance.

6.6 Summary

This section discussed the findings from the observed analysis as part of summarizing and concluding the study.

References

[1] S. Malik and P. K. Sahu, "Free space optics/millimeter-wave based vertical and horizontal terrestrial backhaul network for 5G," *Optics Communications,* vol. 459, p. 125010, 2020/03/15/ 2020.

[2] P. Saxena, A. Mathur, and M. R. Bhatnagar, "BER performance of an optically pre-amplified FSO system under turbulence and pointing errors with ASE noise," *Journal of Optical Communications and Networking,* vol. 9, no. 6, pp. 498-510, 2017.

[3] A. K. Majumdar, Z. Ghassemlooy, and A. A. B. Raj, *Principles and applications of free space optical communications*. 2019.

[4] C. Ng Boon, A. Premadi, M. S. Ab-Rahman, and K. Jumari, "Optical power budget and cost estimation for Intelligent Fiber-To-the-Home (i-FTTH)," in *International Conference On Photonics 2010*, 5-7 July 2010 2010, pp. 1-5.

[5] X. Sun *et al.*, "A review on practical considerations and solutions in underwater wireless optical communication," *Journal of Lightwave Technology,* vol. PP, pp. 1-1, 12/16 2019, doi: 10.1109/JLT.2019.2960131.

[6] N. C. Luong, D. T. Hoang, P. Wang, D. Niyato, D. I. Kim, and Z. Han, "Data collection and wireless communication in Internet of Things (IoT) using economic analysis and pricing models: A survey," *IEEE Communications Surveys & Tutorials,* vol. 18, no. 4, pp. 2546-2590, 2016

[7] M. Z. Chowdhury, M. Shahjalal, S. Ahmed, and Y. M. Jang, "6G Wireless Communication Systems: Applications, Requirements, Technologies, Challenges, and Research Directions," *IEEE Open Journal of the Communications Society,* vol. 1, pp. 957-975, 2020.

[8] S. E. Falodun, J. S. Ojo, and O. L. Ojo, "Analysis of visibility effects on free space earth-to-satellite optical link based on measurement data in Nigeria," *Nigeria Journal of Pure and Applied Physics,* vol. 9, no. 1, pp. 41–45, 2020, doi: 10.4314/njpap.v9i1.8.

[9] E. Verdugo, R. Nebuloni, L. Luini, C. Riva, L. d. S. Mello, and G. Roveda, "Rain effects on fso and mmwave links: Preliminary results from an experimental study," presented at the 2020 29th Wireless and Optical Communications Conference (WOCC), 1-2 May 2020, 2020.

[10] P. Krishnan, G. K. Jha, and A. Walia, "Performance enhancement of BPSK-SIM- and DPSK-SIM-based FSO downlink over atmospheric turbulence using aperture averaging and receiver diversity," *Photonic Network Communications,* vol. 38, 08/01 2019.

[11] M. Ehsan, U. A. Korai, A. W. Memon, A. Ullah, B. Muneer, and A. A. Memon, "Availability of free space optical links of hyderabad pakistan using climate data," presented at the 2023 Global Conference on Wireless and Optical Technologies (GCWOT), 24-27 Jan. 2023, 2023.

[12] D. Agarwal and A. Bansal, "Unified performance of free space optical link over exponentiated Weibull turbulence channel," *IET Communications,* vol. 12, no. 20, pp. 2568-2573, 2018.

[13] C. Huang, P. Wang, W. Pang, L. Guo, and X. Liu, "The performance analysis of multi-hop mimo free space optical communications with space–time block codes over exponentiated weibull fading channels," *Optics Communications,* vol. 442, pp. 95-100, 2019.

[14] H. E. Nistazakis and G. S. Tombras, "On the use of wavelength and time diversity in optical wireless communication systems over gamma–gamma turbulence channels," *Optics & Laser Technology,* vol. 44, no. 7, pp. 2088-2094, 2012/10/01/ 2012.

[15] N. S. Sadzali, N. A. M. Nor, and S. H. B. A. Aziz, "Performance analysis of FSO systems using different modulation techniques under the influence of atmospheric turbulence," in *2021 8th International Conference on Computer and Communication Engineering (ICCCE)*, 22-23 June 2021 2021, pp. 397-400.

[16] M. Sahu, K. V. Kiran, and S. K. Das, "FSO link performance analysis with different modulation techniques under atmospheric turbulence," in *2018 Second International Conference on Electronics, Communication and Aerospace Technology (ICECA)*, 29-31 March 2018 2018, pp. 619-623.

[17] K. O. Odeyemi, P. A. Owolawi, and V. M. Srivastava, "A comparison between mathematical tools for analyzing FSO systems over Gamma-Gamma atmospheric channel," in *2017 IEEE AFRICON*, 18-20 Sept. 2017 2017, pp. 549-554.

[18] S. Malik and P. K. Sahu, "Performance analysis of free space optical communication system using different modulation schemes over weak to strong atmospheric turbulence channels," in *Optical and Wireless Technologies*, Singapore, V. Janyani, G. Singh, M. Tiwari, and A. d'Alessandro, Eds., 2020// 2020: Springer Singapore, pp. 387-399.

[19] S. P. Maswikaneng, P. A. Owolawi, S. O. Ojo, and M. I. Mphahlele, "Atmospheric effects on free space optics wireless communication: Applications and challenges," in *2018 International Conference on Intelligent and Innovative Computing Applications (ICONIC)*, 6-7 Dec. 2018 2018, pp. 1-5.

[20] S. P. Maswikaneng, P. A. Owolawi, S. O. Oio, M. I. Mphahlele, and Z. L. Mahlobogwane, "Investigation of different modulation techniques under strong FSO turbulance channel in South Africa," *2020 Asia Conference on Computers and Communications, ACCC 2020*, pp. 75-81, 2020.

[21] M. I. Petković, G. T. Dordević, and D. N. Milić, "BER performance of IM/DD FSO system with OOK using APD receiver," *Radioengineering,* vol. 23, no. 1, pp. 480-487, 2014.

[22] A. Tellez, "Design and characterization of an affordable laser communication system," 2018.

[23] A. G. Alkholidi and K. S. Altowij, "Free space optical communications — theory and practices," 2014, pp. 159-212.

[24] R. C. Conzalez and R. E. Woods, *Digital image proccessing* Prentice Hall, 2009.

[25] M. A. Khalighi and M. Uysal, "Survey on free space optical communication: A communication theory perspective," *IEEE communications surveys & tutorials,* vol. 16, no. 4, pp. 2231-2258, 2014.

[26] I. Alimi, A. Shahpari, A. Sousa, R. Ferreira, P. Monteiro, and A. Teixeira, "Challenges and opportunities of optical wireless communication technologies," *Optical communication technology,* vol. 10, 2017.

[27] T. Plank, E. Leitgeb, P. Pezzei, and Z. Ghassemlooy, "Wavelength-selection for high data rate Free Space Optics (FSO) in next generation wireless communications," in *2012 17th European Conference on Networks and Optical Communications*, 2012, pp. 1-5.

[28] H. Kaushal and G. Kaddoum, "Optical Communication in Space: Challenges and Mitigation Techniques," *IEEE Communications Surveys & Tutorials,* vol. 19, no. 1, pp. 57-96, 2017.

[29] F. Vatansever and M. Hamblin, "Far infrared radiation (FIR): Its biological effects and medical applications," *Photon Lasers Med,* vol. 1, pp. 255-266, 2012.

[30] Sawhil, S. Agarwal, Y. Singhal, and P. Bhardwaj, "An overview of free space optical communication," *International Journal of Engineering Trends and Technology (IJETT),* vol. 55, 2018.

[31] S. A. Al-Gailani *et al.*, "A survey of free space optics (FSO) communication systems, links, and networks," *IEEE Access,* vol. 9, pp. 7353-7373, 2021.

[32] A. Malik and P. Singh, "Free space optics: Current applications and future challenges," *International Journal of Optics,* vol. 2015, p. 945483, 2015.

[33] S. A. Zabidi, M. R. Islam, W. A. Khateeb, and A. W. Naji, "Investigating of rain attenuation impact on Free Space Optics propagation in tropical region," in *2011 4th International Conference on Mechatronics (ICOM)*, 17-19 May 2011 2011, pp. 1-6.

[34] A. Jahid, M. H. Alsharif, and T. J. Hall, "A contemporary survey on free space optical communication: Potentials, technical challenges, recent advances and research direction," *Journal of Network and Computer Applications,* vol. 200, p. 103311, 2022/04/01/ 2022.

[35] E. Michailidis, P. Bithas, N. Nomikos, D. Vouyioukas, and A. Kanatas, "Outage probability analysis in multi-user FSO/RF and UAV-enabled MIMO communication networks," *Physical Communication,* vol. 49, p. 101475, 10/22 2021, doi: 10.1016/j.phycom.2021.101475.

[36] S. Kumar and N. Sharma, "Emerging military applications of free space optical communication technology: A detailed review," *Journal of Physics: Conference Series,* vol. 2161, 2022.

[37] R. Hou, Y. Chen, J. Wu, and H. Zhang, "A brief survey of optical wireless communication," in *Proc. Australas. Symp. Parallel Distrib. Comput.(AusPDC 15)*, 2015, vol. 163, pp. 41-50.

[38] H. Ogunmodede, "Performance evaluation of FSO communication systems over weak atmospheric turbulence channel for eastern coast of south africa," 2017.

[39] K. Mtshiza, N. Pillay, and E. O. Olurotimi, "Free Space Optical Communication Link Performance Based on Various Transmission Schemes Over Gamma-Gamma Distribution Channel," in *2023 International Conference on Electrical, Computer and Energy Technologies (ICECET)*, 16-17 Nov. 2023 2023, pp. 1-6.

[40] J. Mikolajczyk *et al.*, "Analysis of free-space optics development," *Metrology and Measurement Systems*, vol. 24, 12/20 2017, doi: 10.1515/mms-2017-0060.

[41] K. Wang, Q. Chen, C. Jiang, Z. Chen, Q. Lu, and W. Guo, "Narrow linewidth and low thermal tuning power thermally tuned multi-channel interference widely tunable semiconductor laser," in *Optical Fiber Communication Conference (OFC) 2021*, Washington, DC, 2021/06/06 2021: Optica Publishing Group.

[42] J. Lee, J. Hahn, and H. Kim, "Diffractive optical element for noise-reduced beam shaping of multi-array point light source," *Current Optics and Photonics*, vol. 5, no. 5, pp. 506-513, 2021/10/25 2021.

[43] R. Ramirez-Iniguez, S. M. Idrus, and Z. Sun, *Optical wireless communications: IR for wireless connectivity*. CRC press, 2008.

[44] J. C. Ricklin, S. M. Hammel, F. D. Eaton, and S. L. Lachinova, "Atmospheric channel effects on free-space laser communication," *Journal of Optical and Fiber Communications Reports*, vol. 3, pp. 111-158, 2006.

[45] M. Ijaz, Z. Ghassemlooy, H. L. Minh, S. Rajbhandari, and J. Perez, "Analysis of fog and smoke attenuation in a free space optical communication link under controlled laboratory conditions," in *2012 International Workshop on Optical Wireless Communications (IWOW)*, 22-22 Oct. 2012 2012, pp. 1-3, doi: 10.1109/IWOW.2012.6349680.

[46] D. A. Rockwell and G. S. Mecherle, "Wavelength selection for optical wireless communications systems," in *Optical Wireless Communications IV*, 2001, vol. 4530: SPIE, pp. 27-35.

[47] O. O. Kolawole, "Performance analysis of optical wireless communication systems in a warm-summer mediterranean climatic region," 2017.

[48] H. Singh and A. Sappal, "Performance analysis of FSO link in log-normal channel using different modulation schemes," 2020, pp. 143-155.

[49] K. Kaur, R. Miglani, and G. Gaba, "Communication theory review perspective on channel modeling, modulation and mitigation techniques in free space optical communication," *International Journal of Control Theory and Applications*, vol. 09, pp. 4969-4978, 09/30 2016.

[50] K. O. Odeyemi, P. A. Owolawi, and V. M. Srivastava, "A comparison between mathematical tools for analyzing FSO systems over Gamma-Gamma atmospheric channel," *2017 IEEE AFRICON: Science, Technology and Innovation for Africa, AFRICON 2017*, pp. 549-554, 2017.

[51] I. Alimi, A. Shahpari, V. Ribeiro, N. Kumar, P. Monteiro, and A. Teixeira, "Optical wireless communication for future broadband access networks," in *2016 21st European Conference on Networks and Optical Communications (NOC)*, 1-3 June 2016 2016, pp. 124-128.

[52] K. Sharma and S. K. Grewal, "A new ABER approximation of FSO system using PPM–GMSK hybrid modulation scheme under weak turbulence," *Optik,* vol. 248, no. May 2019, pp. 168129-168129, 2021.

[53] D. Anandkumar and R. G. Sangeetha, "A survey on performance enhancement in free space optical communication system through channel models and modulation techniques," *Optical and Quantum Electronics,* vol. 53, no. 1, p. 5, 2020/11/28 2020.

[54] V. Srivastava, A. Mandloi, D. Patel, and P. Shah, "Performance analysis of negative exponential turbulent FSO links with wavelength diversity," in *2020 12th International Symposium on Communication Systems, Networks and Digital Signal Processing (CSNDSP)*, 20-22 July 2020 2020, pp. 1-5.

[55] M. Ding, Y. Li, Y. Quan, L. Guo, and M. Xing, "A novel reconstruction method of k-distributed sea clutter with spatial-temporal correlation," (in eng), *Sensors (Basel),* vol. 20, no. 8, Apr 22 2020.

[56] S. Tannaz, C. Ghobadi, J. Nourinia, and E. Mostafapour, *The effects of negative exponential and k-distribution modeled fso links on the performance of diffusion adaptive networks*. 2018, pp. 19-22.

[57] K. Kaur, R. Miglani, and J. Malhotra, "The Gamma-Gamma channel model - a survey," *Indian Journal of Science and Technology,* vol. 9, 12/28 2016.

[58] A. K. M. S. J. Choyon, R. Chowdhury, and S. M. R. Chowdhury, "Optimum Link Distance and BER Performance Investigation for BPSK RF Sub-carrier Coherent FSO Communication System under Strong Turbulence," *International Journal of Scientific & Technology Research,* vol. 9, pp. 282-287, 09/01 2020.

[59] D. Luong, T. Cong Thang, and A. Pham, "Effect of avalanche photodiode and thermal noises on the performance of binary phase-shift keyingsubcarrier-intensity modulation/free-space optical systems over turbulence channels," *Communications, IET,* vol. 7, pp. 738-744, 05/21 2013.

[60] N. Lazer and Y. P. A. Teen, "Free space optical communication and laser beam propagation through turbulent atmosphere: A brief survey," in *2019 International Conference on Recent Advances in Energy-efficient Computing and Communication (ICRAECC)*, 7-8 March 2019 2019, pp. 1-6.

[61] E. Farooq, A. Sahu, and S. K. Gupta, "Survey on FSO communication system—limitations and enhancement techniques," in *Optical and wireless technologies: proceedings of OWT 2017*, 2018: Springer, pp. 255-264.

[62] Z. Wang, W. D. Zhong, S. Fu, and C. Lin, "Performance comparison of different modulation formats over free-space optical (FSO) turbulence links with space diversity reception technique," *IEEE Photonics Journal,* vol. 1, no. 6, pp. 277-285, 2009.

[63] H.-M. Park, Y.-J. Hyun, and S.-K. Han, "Adaptive beam divergence control to mitigate scintillation effect caused by pointing error in vertical FSO transmissions," *Sensors,* vol. 23, no. 11, doi: 10.3390/s23115045.

[64] G. Aarthi, K. Prabu, and G. R. Reddy, "Aperture averaging effects on the average spectral efficiency of FSO links over turbulence channel with pointing errors," *Optics Communications,* vol. 385, pp. 136-142, 2017.

[65] N. Rani, P. Singh, and P. Kaur, "Mitigation of Scintillation effects in WDM-FSO system using Homodyne detection," *Optik*, vol. 248, p. 168165, 2021.

[66] I. Alimi, A. Shahpari, V. Ribeiro, A. Sousa, P. Monteiro, and A. Teixeira, "Channel characterization and empirical model for ergodic capacity of free-space optical communication link," *Optics Communications*, vol. 390, pp. 123-129, 2017/05/01/ 2017.

[67] Y. Wu, H. Mei, C. Dai, F. Zhao, and H. Wei, "Design and analysis of performance of FSO communication system based on partially coherent beams," *Optics Communications*, vol. 472, p. 126041, 2020.

[68] B. Barua and S. P. Majumder, "Free Space Optical Communication with OOK and BPSK modulation under different turbulent condition," in *2013 International Conference on Informatics, Electronics and Vision (ICIEV)*, 2013, pp. 1-5.

[69] I. S. Ansari, F. Yilmaz, and M. S. Alouini, "Performance analysis of free-space optical links over málaga (*M*) turbulence channels with pointing errors," *IEEE Transactions on Wireless Communications*, vol. 15, no. 1, pp. 91-102, 2016.

[70] S. Ghoname, H. A. Fayed, A. A. E. Aziz, and M. H. Aly, "Performance analysis of FSO communication system: Effects of fog, rain and humidity," in *2016 Sixth International Conference on Digital Information Processing and Communications (ICDIPC)*, 2016, pp. 151-155.

[71] S. Borwankar and D. Shah, "Effect of weather conditions on FSO link," in *Electrical Engineering and System Science*, 2020.

[72] A. Kesarwani, Anuranjana, S. Kaur, M. Kaur, and P. S. Vohra, "Performance analysis of fso link under diferent conditions of fog in delhi, india," in *2018 2nd IEEE International Conference on Power Electronics, Intelligent Control and Energy Systems (ICPEICES)*, 22-24 Oct. 2018 2018, pp. 958-961.

[73] Anuranjana, S. Kaur, and R. Goyal, "Analysis of terrestrial fso link performance considering different fog conditions and internal parameters of the system," in *2019 6th International Conference on Signal Processing and Integrated Networks (SPIN)*, 2019, pp. 552-557.

[74] J. S. Ojo, J. A. Olaitan, and O. L. Ojo, "Characterization of fog-induced attenuation for optimizing optical propagation links in Nigeria," *Results in Optics*, vol. 9, no. July, pp. 100279-100279, 2022, doi: 10.1016/j.rio.2022.100279.

[75] O. B. Aborisade, J. S. Ojo, P. A. Owolawi, and K. D. Adedayo, "Prediction of attenuation using visibility variations and other meteorological parameters in george, western cape, south africa," *IOP Conference Series: Earth and Environmental Science*, vol. 665, no. 1, p. 012053, 2021/03/01 2021, doi: 10.1088/1755-1315/665/1/012053.

[76] J. Mohale, M. R. Handura, T. O. Olwal, and C. N. Nyirenda, "Feasibility study of free-space optical communication for South Africa," *Optical Engineering*, vol. 55, 2016.

[77] J. Singh and N. Kumar, "Performance analysis of different modulation format on free space optical communication system," *Optik*, vol. 124, no. 20, pp. 4651-4654, 2015, doi: 10.1016/j.ijleo.2013.02.014.

[78] K. Md.shahiduzzaman, M. Hassan, B. Karmaker, and L. Biswas, "Scattering effect on terrestrial free space optical signal in tropical weather condition," *IOSR Journal of Electronics and Communication Engineering (IOSR-JECE),* vol. 10, pp. 12-18, 07/04 2015, doi: 10.9790/2834-10411218.

[79] M. Singh, S. Bhatia, and H. Kaushal, "Performance evaluation of free space optical link under various weather conditions," *Advances in Intelligent Systems and Computing,* vol. 379, pp. 329-342, 01/01 2016, doi: 10.1007/978-81-322-2517-1_33.

[80] S. Shah, S. Mughal, and S. Memon, "Theoretical and empirical based extinction coefficients for fog attenuation in terms of visibility at 850 nm," in *2015 International Conference on Emerging Technologies (ICET),* 19-20 Dec. 2015 2015, pp. 1-4, doi: 10.1109/ICET.2015.7389190.

[81] S. Ghoname, H. A. Fayed, A. A. El Aziz, and M. H. Aly, "Performance evaluation of an adaptive hybrid FSO/RF communication system: impact of weather attenuation," *Iranian Journal of Science and Technology, Transactions of Electrical Engineering,* vol. 44, pp. 119-128, 2020.

[82] P. Demir and G. Yılmaz, "Investigation of the Atmospheric Attenuation Factors in FSO Communication Systems Using the Taguchi Method," *International Journal of Optics,* vol. 2020, p. 9038053, 2020/03/12 2020, doi: 10.1155/2020/9038053.

[83] T. Siegel and S.-P. Chen, "Investigations of free space optical communications under real-world atmospheric conditions," *Wireless Personal Communications,* vol. 116, 01/01 2021, doi: 10.1007/s11277-020-07724-1.

[84] F. Hossain and Z. Afroze, "Eliminating the effect of fog attenuation on FSO link by multiple TX/RX system with travelling wave semiconductor optical amplifier," in *2013 2nd International Conference on Advances in Electrical Engineering (ICAEE),* 19-21 Dec. 2013 2013, pp. 267-272, doi: 10.1109/ICAEE.2013.6750345.

[85] O. Ajewole, O. Pius, J. Ojo, and M. Adetunji, "Fog and rain attenuation characterization and performance of terrestrial free space optical communication in Akure, Nigeria," *APTIKOM Journal on Computer Science and Information Technologies,* vol. 4, pp. 125-134, 01/27 2020, doi: 10.34306/csit.v4i3.100.

[86] J. Latal *et al.*, "Simulation and measurement of atmospheric effect on optical beam," in *2018 20th International Conference on Transparent Optical Networks (ICTON),* 1-5 July 2018 2018, pp. 1-7, doi: 10.1109/ICTON.2018.8473649.

[87] M. A. Ali, "Characterization of fog attenuation for free space optical communication link," *International Journal of Electronics and Communication Engineering & Technology (IJECET),* vol. 4, pp. 244-255, 06/01 2013.

[88] S. Ghoname, H. A. Fayed, A. Abd El Aziz, and M. H. Aly, "Performance analysis of FSO communication system: Effects of fog, rain and humidity," in *2016 Sixth International Conference on Digital Information Processing and Communications (ICDIPC),* 2016: IEEE, pp. 151-155.

[89] A. Alatawi, A. Youssef, M. Abaza, M. A. Uddin, and A. Mansour, "Effects of Atmospheric Turbulence on Optical Wireless Communication in NEOM Smart City," (in English), *Photonics,* vol. 9, no. 4, p. 262, 2022-04 2022, doi: 10.3390/photonics9040262.

[90] C. A. B. Dath and N. A. B. Faye, "Resilience of long range free space optical link under a tropical weather effects," *Scientific African,* vol. 7, pp. e00243-e00243, 2020, doi: 10.1016/j.sciaf.2019.e00243.

[91] A. S. Alatawi, A. A. Youssef, M. Abaza, M. A. Uddin, and A. Mansour, "Effects of atmospheric turbulence on optical wireless communication in NEOM smart city," in *Photonics*, 2022, vol. 9, no. 4: MDPI, p. 262.

[92] R. Barrios, "Exponentiated Weibull fading channel model in free-space optical communications under atmospheric turbulence Ph. D. dissertation," *Dept. Signal Theory Commun., Univ. Politcnica de Catalunya,* 2013.

[93] O. O. Kolawole, T. J. O. Afullo, and M. Mosalaosi, "Analysis of Scintillation Effects on Free Space Optical Communication Links in South Africa," *Photonics,* vol. 9, no. 7, 2022, doi: 10.3390/photonics9070446.

[94] A. Lionis, K. Peppas, H. E. Nistazakis, A. D. Tsigopoulos, and K. Cohn, "Experimental performance analysis of an optical communication channel over maritime environment," *Electronics,* vol. 9, no. 7, doi: 10.3390/electronics9071109.

[95] J. Kwiecień, "The effects of atmospheric turbulence on laser beam propagation in a closed space—An analytic and experimental approach," *Optics Communications,* vol. 433, pp. 200-208, 2019/02/15/ 2019.

[96] E. S. Olukanni, O. A. Olayemi, E. Amao, and J. A. Adeyemi, "Analysis of Atmospheric Turbulence Effect on Free Space Optical Communications in Ilorin, Kwara State, Nigeria," *Kufa Journal of Engineering,* vol. 10, no. 2, pp. 126-133, 2019, doi: 10.30572/2018/kje/100210.

[97] Y. Chahine, S. A. Tedder, B. E. Vyhnalek, and A. C. Wroblewski, "Beam propagation through atmospheric turbulence using an altitude-dependent structure profile with non-uniformly distributed phase screens," pp. 40-40, 2020.

[98] K. S. Altowij, A. Alkholidi, and H. Hamam, "Effect of clear atmospheric turbulence on quality of free space optical communications in yemen," pp. 423–428, 2010.

[99] L. Andrews, R. Philips, and C. Hopen, *Laser Beam Scintillation With Applications*. Bellingham: SPIE, 2001.

[100] H. AlQuwaiee, H. C. Yang, and M. S. Alouini, "On the Asymptotic Capacity of Dual-Aperture FSO Systems With Generalized Pointing Error Model," *IEEE Transactions on Wireless Communications,* vol. 15, no. 9, pp. 6502-6512, 2016.

[101] P. Kaur, V. K. Jain, and S. Kar, "Performance Analysis of FSO Array Receivers in Presence of Atmospheric Turbulence," *IEEE Photonics Technology Letters,* vol. 26, no. 12, pp. 1165-1168, 2014, doi: 10.1109/LPT.2014.2316534.

[102] D. A. Luong and A. T. Pham, "Average capacity of MIMO free-space optical gamma-gamma fading channel," in *2014 IEEE International Conference on Communications (ICC)*, 10-14 June 2014 2014, pp. 3354-3358.

[103] K. Prabu, "Performance analysis of FSO systems over atmospheric turbulence channel for indian weather conditions," in *Turbulence and Related Phenomena*, B. Régis Ed. Rijeka: IntechOpen, 2019, p. Ch. 2.

[104] S. Malik and P. K. Sahu, "Performance analysis of free space optical communication system using different modulation schemes over weak to strong atmospheric turbulence channels," in *Optical and Wireless Technologies: Proceedings of OWT 2018*, 2020: Springer, pp. 387-399.

[105] O. O. Kolawole, T. J. O. Afullo, and M. Mosalaosi, "Analysis of scintillation effects on free space optical communication links in south africa," *Photonics for Solar Energy Systems IX*, vol. 9, p. 446, June 01, 2022 2022.

[106] L. Yang, X. Song, J. Cheng, and J. F. Holzman, "Free-space optical communications over lognormal fading channels using OOK with finite extinction ratios," *IEEE Access*, vol. 4, pp. 574-584, 2016, doi: 10.1109/ACCESS.2016.2520936.

[107] A. Garcia-Zambrana, C. Castillo-Vázquez, and B. Castillo-Vázquez, "On the capacity of FSO links over gamma-gamma atmospheric turbulence channels using OOK signaling," *EURASIP Journal on Wireless Communications and Networking*, vol. 2010, p. 64, 12/01 2010, doi: 10.1155/2010/127657.

[108] S. Johari and V. Sundharam, "Performance analysis of an earth-satellite intensity modulated FSO link in the presence of turbulence and varying path loss," in *2017 7th International Conference on Communication Systems and Network Technologies (CSNT)*, 11-13 Nov. 2017 2017, pp. 38-43, doi: 10.1109/CSNT.2017.8418508.

[109] V. K. Kappala, J. Pradhan, M. Sahu, A. K. Turuk, and S. K. Das, "Performance analysis of FSO for different modulation techniques under atmospheric turbulence with pointing errors," in *2021 2nd International Conference on Range Technology (ICORT)*, 5-6 Aug. 2021 2021, pp. 1-5, doi: 10.1109/ICORT52730.2021.9581438.

[110] M. Al-Nahhal, T. Ismail, H. Selmy, and M. M. Elmesalawy, "BPSK based SIM-FSO communication system with SIMO over log-normal atmospheric turbulence with pointing errors," in *2017 19th International Conference on Transparent Optical Networks (ICTON)*, 2-6 July 2017 2017, pp. 1-4.

[111] Z. Xu, G. Xu, Z. Zheng, and S. Arnon, "BER and channel capacity performance of an FSO communication system over atmospheric turbulence with different types of noise," *Sensors (14248220)*, vol. 21, no. 10, pp. 3454-3454-3454, 2021-05-15 2021.

[112] P. Kaur, V. K. Jain, and S. Kar, "Effect of atmospheric conditions and aperture averaging on capacity of free space optical links," *Optical and Quantum Electronics*, vol. 46, no. 9, pp. 1139-1148, 2014/09/01 2014, doi: 10.1007/s11082-013-9845-3.

[113] S. A. H. Mohsan, M. A. Khan, and H. Amjad, "Hybrid FSO/RF networks: A review of practical constraints, applications and challenges," *Optical Switching and Networking*, vol. 47, p. 100697, 2023/02/01/ 2023.

[114] Z. Huiying, L. Hongzuo, D. Xiao, and C. Cai, "Performance Analysis of Different Modulation Techniques for Free-Space Optical Communication System," *Telecommunication Computing Electronics and Control*, vol. 13, no. 3, pp. 880-888, 2015-09-01 2015, doi: 10.12928/TELKOMNIKA.v13i3.1976.

Appendix A: Scattering Coefficient Computation

```
%November 2023
%Atmospheric Coefficient per unit length
% Writer: Kholekile Mtshiza (20817081)
% Description: This code is used to calculate scattering Coefficient per unit
length

close all;
clc;
%% fog/smoke channel

wavelength=linspace(550e-9,1700e-9,200);
%Propagation wavelength (m) array
Fog_Vis=linspace(25.96,35,10);
%Visibility Cape Town (m)

WaveL_0 = 550e-9;
%Propagation wavelength (green light) reference (m)
ThrH_FS = 2/100;                                                    %Threshold
(2%)
Propagation_Len = 5e3;
%Propagation Distance (m)

%----------Propagation wavelength (m)-------------------------%
WaveL_1=650e-9;
WaveL_2=850e-9;
WaveL_3=1200e-9;
WaveL_4 =1550e-9;

%% atmospheric attenuation
Fog_VisualRange = zeros(size(Fog_Vis));
% update the Vis_fS array

for i=1:length(Fog_Vis)

 Fog_VisualRange(i)=Fog_Vis(i);

    switch logical(true)

    case (Fog_VisualRange(i) > 50)
% Fog_Visibility > 50 km
        q_Fog = 1.6;
    case ((Fog_VisualRange(i)<= 50) && (Fog_VisualRange(i)> 6))
% 6 km < Fog_Visibility <= 50 km
        q_Fog = 1.3;
    case ((Fog_VisualRange(i) <= 6) && (Fog_VisualRange(i) > 1))
% 1 km < Fog_Visibility <= 6 km
        q_Fog = 0.16*Fog_VisualRange(i) + 0.34;
    case ((Fog_VisualRange <= 1) && (Fog_VisualRange > 0.5))
% 0.5 km <Fog_Visibility <= 1 km
        q_Fog = Fog_VisualRange(i) + 0.5;
    case (Fog_VisualRange(i)<= 0.5)
% Fog_Visibility <= 0.5 km
        q_Fog = 0;
```

```
    otherwise
% otherwise
        q_Fog = 0;
    end

   %----- Atmospheric Attenuation Coefficient (Signal Transmission) -----%
beta_1 =(-log(ThrH_FS)./Fog_VisualRange(i)).*(WaveL_1/WaveL_0).^(-q_Fog);
beta_2 =(-log(ThrH_FS)./Fog_VisualRange(i)).*(WaveL_2/WaveL_0).^(-q_Fog);
beta_3 =(-log(ThrH_FS)./Fog_VisualRange(i)).*(WaveL_3/WaveL_0).^(-q_Fog);
beta_4 =(-log(ThrH_FS)./Fog_VisualRange(i)).*(WaveL_4/WaveL_0).^(-q_Fog);

plot(Fog_VisualRange(i),beta_1, 'rv-', 'LineWidth', 1.5, 'MarkerSize', 5);
hold on
plot(Fog_VisualRange(i),beta_2, 'b*-', 'LineWidth', 1.5, 'MarkerSize', 5);
hold on
plot(Fog_VisualRange(i),beta_3, 'yo-', 'LineWidth', 1.5, 'MarkerSize', 5);
hold on
plot(Fog_VisualRange(i),beta_4, 'g+-', 'LineWidth', 1.5, 'MarkerSize', 5);
hold on
end

legend({'650mn','850nm','1220nm','1550nm'});
xlabel('Average Visibility(km) in Cape Town')
ylabel('Scattering Coefficient(1/km)')
title('Scattering Coefficient(1/km) vs. Visibility(km)');
grid on;
```

Appendix B: Specific Atmospheric Attenuation Computation

```
% Cape Town
% November 2023
% Atmospheric attenuation per unit length
% Writer: Kholekile Mtshiza (20817081)
% Description: This code is used to Compute Specific Atmospheric Attenuation
per unit length
close all;
clc;
%% fog/smoke channel
wavelength=linspace(550e-9,1700e-9,200);
%Propagation wavelength (m) array
Fog_Vis=linspace(25.96,35,10);                                          %Highest
Visibility Cape Town(m)
WaveL_0 = 550e-9;
%Propagation wavelength (green light) reference (m)
ThrH_FS = 2/100;
%Threshold (2%)
Propagation_Len =5e3;
%Propagation Distance (m)
%----------Propagation wavelength (m)------------------------%
WaveL_1=650e-9;
WaveL_2=850e-9;
WaveL_3=1200e-9;
WaveL_4 =1550e-9;
%% atmospheric attenuation
Fog_VisualRange = zeros(size(Fog_Vis));              % update the Vis_fS array
hold on;
for i=1:length(Fog_Vis)

 Fog_VisualRange(i)=Fog_Vis(i);

    switch logical(true)

    case (Fog_VisualRange(i) > 50)                                          %
Fog_Visibility > 50 km
        q_Fog = 1.6;
    case ((Fog_VisualRange(i)<= 50) && (Fog_VisualRange(i)> 6))              %
6 km < Fog_Visibility <= 50 km
        q_Fog = 1.3;
    case ((Fog_VisualRange(i) <= 6) && (Fog_VisualRange(i) > 1))             %
1 km < Fog_Visibility <= 6 km
        q_Fog = 0.16*Fog_VisualRange(i) + 0.34;
```

```
    case ((Fog_VisualRange <= 1) && (Fog_VisualRange > 0.5))                  %
0.5 km < Fog_Visibility <= 1 km
        q_Fog = Fog_VisualRange(i) + 0.5;
    case (Fog_VisualRange(i)<= 0.5)                                           %
Fog_Visibility <= 0.5 km
        q_Fog = 0;

        otherwise
% otherwise
        q_Fog = 0;
    end

beta_1 =(-log(ThrH_FS)./Fog_VisualRange(i)).*(WaveL_1/WaveL_0).^(-q_Fog);     %
Scattering Coeffieicnt /Signal Transmission (1/km)
Spc_Atm_Att_Sim1=4.343.*beta_1*Propagation_Len/1e3;                           %
Specific Atmospheric Attenuation (dB/km)

beta_2 =(-log(ThrH_FS)./Fog_VisualRange(i)).*(WaveL_2/WaveL_0).^(-q_Fog);
Spc_Atm_Att_Sim2=4.343.*beta_2*Propagation_Len/1e3;

beta_3 =(-log(ThrH_FS)./Fog_VisualRange(i)).*(WaveL_3/WaveL_0).^(-q_Fog);
Spc_Atm_Att_Sim3=4.343.*beta_3*Propagation_Len/1e3;

beta_4 =(-log(ThrH_FS)./Fog_VisualRange(i)).*(WaveL_4/WaveL_0).^(-q_Fog);
Spc_Atm_Att_Sim4=4.343.*beta_4*Propagation_Len/1e3;

plot(Fog_VisualRange(i),Spc_Atm_Att_Sim1, 'rv-', 'LineWidth', 1.5,
'MarkerSize', 5);
hold on
plot(Fog_VisualRange(i),Spc_Atm_Att_Sim2, 'b*-', 'LineWidth', 1.5,
'MarkerSize', 5);
hold on
plot(Fog_VisualRange(i),Spc_Atm_Att_Sim3, 'yo-', 'LineWidth', 1.5,
'MarkerSize', 5);
hold on
plot(Fog_VisualRange(i),Spc_Atm_Att_Sim4, 'g+-', 'LineWidth', 1.5,
'MarkerSize', 5);
hold on
end

Fog_VisualRange(i)=+1;
legend({'650mn','850nm','1220nm','1550nm'});
xlabel('Avarage Visibility(km) in Cape Town')
ylabel('Avarage Specific Atmospheric Attenuation (dB/km)')
title('Atmospheric Attenuation (dB/km) vs. Visibility(km)');
grid on;
```

Appendix C: Fog Attenuation Computation

```
% Cape Town
% November 2023
% fog/smoke attenuation
% Writer: Kholekile Mtshiza (20817081)
% Description: This file is used to calculate fog attenuation over link range.

close all;
clc;
%% fog/smoke channel

Fog_VisualRange = 25.96;
%Cape Town Avarage VisualRange (m) Over period of 2 years
Propagation_Len=linspace(0,5,10);
%FSO link Length (km)
WaveL_0 = 550e-9;
%Propagation wavelength (green light) reference (m)
ThrH_FS = 2/100;
%contrast threshold (typical value = 2%)
WaveL_1=650e-9;
WaveL_2=850e-9;
WaveL_3=1200e-9;
WaveL_4=1550e-9; % laser wavelength (m)
%% atmospheric attenuation
    switch logical(true)                                                %q
value based on Kim model

    case (Fog_VisualRange > 50)
%Visibility > 50 km
        q_Fog = 1.6;
    case (Fog_VisualRange <= 50) && (Fog_VisualRange > 6)                %6
km < Visibility <= 50 km
        q_Fog = 1.3;
    case (Fog_VisualRange<= 6) && (Fog_VisualRange> 1)                   %1
km < Visibility <= 6 km
        q_Fog = (0.16*Fog_VisualRange) + 0.34;
    case (Fog_VisualRange <= 1) && (Fog_VisualRange > 0.5)               %0.5
km < Visibility <= 1 km
        q_Fog = Fog_VisualRange + 0.5;
        case (Fog_VisualRange <= 0.5)
%Visibility <= 0.5 km
        q_Fog = 0;
        otherwise
%otherwise
```

```
        q_Fog = 0;

    end

beta_1 = (-log(ThrH_FS)/Fog_VisualRange)*(WaveL_1/WaveL_0).^(-q_Fog);
%Calculate the scattering coefficient
Atm_Att_Sim1 = exp(-beta_1*Propagation_Len);
%Calculate the propagtion of the optical
Att_Sim01=-10*log10(Atm_Att_Sim1);
%Calculate the scattering losses/atmospheric attenuation
beta_2 = (-log(ThrH_FS)/Fog_VisualRange)*(WaveL_2/WaveL_0).^(-q_Fog);
Atm_Att_Sim2 = exp(-beta_2*Propagation_Len);
Att_Sim02=-10*log10(Atm_Att_Sim2);

beta_3 = (-log(ThrH_FS)/Fog_VisualRange)*(WaveL_3/WaveL_0).^(-q_Fog);
Atm_Att_Sim3 = exp(-beta_3*Propagation_Len);
Att_Sim03=-10*log10(Atm_Att_Sim3);

beta_4 = (-log(ThrH_FS)/Fog_VisualRange)*(WaveL_4/WaveL_0).^(-q_Fog);
% Calculate the scattering coefficient
Atm_Att_Sim4 = exp(-beta_4*Propagation_Len);
% Calculate signal transmission
Att_Sim04=-10*log10(Atm_Att_Sim4);
% Calculate Scattering losses
plot(Propagation_Len,Att_Sim01,'rv-', 'LineWidth', 0.2, 'MarkerSize', 5);
hold on
plot(Propagation_Len,Att_Sim02, 'b*-', 'LineWidth', 0.2, 'MarkerSize', 5);
hold on
plot(Propagation_Len,Att_Sim03, 'yo-', 'LineWidth', 0.2, 'MarkerSize', 5);
hold on
plot(Propagation_Len,Att_Sim04, 'g+-', 'LineWidth', 0.2, 'MarkerSize', 5);
hold on
legend({'650 nm','850 nm','1200 nm','1550 nm'});
xlabel('Link Range (km)')
ylabel('Atmospheric Attenuation (dB/km)')
title('Atmospheric attenuation (dB/km) v.s Link Range (km) Cape Town');
grid on;
```

Appendix D: Average BER Vs SNR Computation

```
%Cape Town
%November 2023
%Gamma-gamma distribution channel for FSO transmission using different
modulation schemes
%Writer: Kholekile Mtshiza (20817081)
%Description: This code is used to compute the average BER Vs SNR based on the
influence of Atmospheric turbulences and weather conditions
clc;
clearvars;
close all;
Propagation_Len =1500;  % link Length (m)
% Propagation_Len =2500;  % link Length (m)
% Propagation_Len =3500;  % link Length (m)
WaveL = 1550e-9; % laser wavelength (m)
%% analytical loss channel calculations
%--------------- Fog Channel---------------
Fog_Visibility= 25.96;                                          %
fog/smoke visibility (km)
Vis_FS = 25.96;                                                 %
fog/smoke visibility (km)
beta_l= 0.039;                                                  %Fog
Attenuation Coefficient (dB)
Atm_Att= exp(-beta_l*Propagation_Len/1e3);                      % Fog
path loss
Spc_Atm_Att=4.343.*beta_l*Propagation_Len/1e3;                   %
Specific Atmospheric Attenuation (dB/km)
disp(Spc_Atm_Att)
% %% APD Parameters & Functions
Rb=10e9;                                            % Data Rate
Rd=0.85;                                            % Responsivity
g=50;                                               % APD gain
Fn=2;                                               % Amplifier Noise
q=1.6023e-19;                                       % charge of electron (C)
Ka=0.7;                                             % Ionasation factor
Kb=1.38e-23;
Rl=50;                                              % APD Load Resistance

%% Cape Town meteorological Parameters
Temperature=17.28;
WindSpeed=4.93;
Altitude=42;
Turbulence= 1.7e-14;
```

```
%----------------------------------------Power-------------------------------
Ptx_dB = linspace(-10,40,18);                              %  Transmitted signal
power range in dB
Ptx_mW =1e-3*10.^(Ptx_dB/10);                              %  Linear power mW

SNR_dB_Range = linspace(0,30,18);                          %  Array for Linear
SNR_Range = 10.^(SNR_dB_Range/10);

%% Turbulence channel analytical formulation
Cn2 = (0.00594*(WindSpeed/27)^2*(10^-5*Altitude)^10*exp(-Altitude/1000)) + ...
      (2.7e-16*exp(-Altitude/1500)) + (Turbulence*exp(-Altitude/100));
x_Sm = 2*pi/WaveL;                                           % wave number
(rad/m)
zig2_X = 1.23*Cn2*x_Sm^(7/6)*Propagation_Len^(11/6);           % Rytov variance
%--------logarithmic major-scale scintillation---------------
XY2 = (0.49*zig2_X)./(1+1.11*(zig2_X).^(12/5)).^(7/6); % PDF parameter alpha
YZ2 =(0.51*zig2_X)./(1+0.69*(zig2_X).^(12/5)).^(5/6); % PDF parameter beta
%-----------major-scale scintillation-------------
ALPH = 1/(exp(XY2) - 1);  % major-scale scintillationALPH
%-----------minor-scale scintillation-------------
BETTA = 1/(exp(YZ2) - 1);  % minor-scalescintillation
zig2_anl = 1/ALPH + 1/BETTA + 1/(ALPH*BETTA);       % analytical scintillation
index (S.I)for Gamma-Gamma model
Game= gamma(ALPH)*gamma(BETTA);                          % Gamma function of
alpha and beta
I = ALPH*BETTA;             % received normalized I as a product of major and
minor scale atmospheric effects
%% APD APD Receiver noise
SNR_dB = zeros(size(Ptx_mW));
Ptx=zeros(size(Ptx_mW));
for i = 1:length(Ptx_mW)

    Ptx=Ptx_mW(i);                                                  % Update
the dB power array

    Fa=Ka*g+(1-Ka)*(2-g^-1);                                        % Excessive
Nosie Factor
    Sigma_Th=(4*Temperature*Kb*Rb*Fn)/Rl;                                    %
Thermal Noise
    Sigma_Sh= (2*q.*g^2.*Rd.*Fa.*Rb.*Ptx.*abs(I))+Sigma_Th;         % Shot
Noise
    Sigma_N=Sigma_Th+Sigma_Sh;                                      % Total
Power Nosie Variance
    Rx_Signal_P=(2*g*Rd.*Ptx*abs(I)).^2;                            %
Instantaneous Received signal (W): (With Constant Channel loss parameters)After
APD conversion (Electrical Signal)
```

```
    SNR_dB(i) =10*log10(Rx_Signal_P/ Sigma_N);                    %Update SNR
(dB) array
    SNR = 10.^(SNR_dB/10);

end
%% -----------Analytical OOK Modulation BER based on Gamma-Gamma models--------
C = 2^(ALPH + BETTA)/8*(sqrt(pi).^3*Game);    % constant
z = SNR*Spc_Atm_Att.^2*(8/(ALPH*BETTA)^2);   % parameters for meijer G function
 %----- parameter for meijer G function-----%
m1 = (1 - ALPH)/2;
m2 = (2 - ALPH)/2;
m3 = (1 - BETTA)/2;
m4 = (2 - BETTA)/2;
m5 = 1;
n1 = 0;
n2 = 1/2;
%--------parameter vector for meijer G function--------%
m = [m1, m2, m3, m4, m5];
n = [n1, n2];
String = 'meijerG(2, 4, [%e, %e, %e, %e, %e], [%e, %e], %e)';  % meijer G
function engine string
BER_Anl_OOK = zeros(size(z));  % Array for BER
     %-------------Loop for Signal-to-Noise Raio value------------%
for Index_H = 1:length(SNR_dB)
MGFunction = evalin(symengine, sprintf(String, m, n, 2*z(Index_H)));  % use
engine to evaluate meijer G function;

 BER_Anl_OOK(Index_H) = C*MGFunction;  % calculate BER
end
%% -----------Analytical BPSK Modulation BER based on Gamma-Gamma models-------
Cc = 2^(ALPH + BETTA)/8*(sqrt(pi).^3*Game);    % constant
Zz = SNR*Spc_Atm_Att.^2*(16/(ALPH*BETTA)^2);  % parameters of meijer G function

        %-----parameter for meijer G function-----%
jj1 = (1 - ALPH)/2;
jj2 = (2 - ALPH)/2;
jj3 = (1 - BETTA)/2;
jj4 = (2 - BETTA)/2;
jj5 = 1;
kk1 = 0;
kk2 = 1/2;
  %--------parameter vector for meijer G function--------%
jj = [jj1, jj2, jj3, jj4, jj5];
kk = [kk1, kk2];
String = 'meijerG(2, 4, [%e, %e, %e, %e, %e], [%e, %e], %e)';  % meijer G
function engine string
```

```
BER_Anl_Bpsk = zeros(size(Zz));  % Array for BER

        %-------------Loop for Signal-to-Noise Raio value ------------%
for Index_J = 1:length(SNR_dB)
MGFunction = evalin(symengine, sprintf(String, jj, kk, 2*Zz(Index_J)));  % use
engine to evaluate meijer G function;
BER_Anl_Bpsk(Index_J) = Cc*MGFunction;  % calculate BER
end
%% -----------Analytical DPSK Modulation BER based on Gamma-Gamma models-------
Ccc = 2^(ALPH + BETTA)/8*(sqrt(pi)*Game);       % constant argument
Zzz = SNR*Spc_Atm_Att.^2*(8/(ALPH*BETTA)^2);   % meijer G function parameter
%----- parameter vector for meijer G function-----%
jjj1 = (1 - ALPH)/2;
jjj2 = (2 - ALPH)/2;
jjj3 = (1 - BETTA)/2;
jjj4 = (2 - BETTA)/2;
kkk1 = 0;
%-------- parameter vector for meijer G function --------%
jjj = [jjj1, jjj2, jjj3, jjj4];
kkk = kkk1;

String = 'meijerG(1, 4, [%e, %e, %e, %e], [%e], %e)';  % meijer G function
BER_Anl_DPSK = zeros(size(Zzz));  % Array for BER
%----------Loop for Signal-to-Noise Raio value-------------%
for Index_K = 1:length(SNR_dB)
MGFunction = evalin(symengine, sprintf(String, jjj, kkk, 2*Zzz(Index_K)));  %
use engine to evaluate meijer G function;
BER_Anl_DPSK(Index_K) = Ccc*MGFunction;  % calculate BER
end
%% ---Plottinf Avarage BER vs. SNR Over GammaGamma Channel --% figure;
semilogy(SNR_dB_Range,BER_Anl_Bpsk ,'g -*','LineWidth', 2);
hold on;
semilogy(SNR_dB_Range, BER_Anl_DPSK ,'b-+','LineWidth', 2);
hold on;
semilogy(SNR_dB_Range,BER_Anl_OOK ,'r-^','LineWidth', 2);

%Set the range for the x-axis
legend({'BPSK Modulation','DPSK Modulation','OOK Modulation' });
xlabel('Average SNR(dB) in Cape Town');
ylabel('Average BER');
string_paragraph = sprintf('Gamma-Gamma model with \\sigma_{R}^2 = %4.2f',
zig2_X);
string_title = sprintf('BER vs. SNR for %s', string_paragraph);
title(string_title);
grid on;
```

Appendix E: Channel Capacity Computation

```
%December 2023
%Gamma-gamma distribution channel for FSO transmission using different
modulation schemes
%Writer: Kholekile Mtshiza (20817081)
%Description: This code is used to compute the average Channel Capacity
achieved based on the influence Atmospheric turbulences and weather conditions
clc;
clearvars;
close all;
Propagation_Len =1500;  % link Length (m)
% Propagation_Len =2500;  % link Length (m)
% Propagation_Len =3500;  % link Length (m)
WaveL = 1550e-9; % laser wavelength (m)
%% analytical loss channel calculations
%--------------- Fog Channel---------------
Fog_Visibility = 28.34;                                                    %
fog/smoke visibility (km)
beta_l= 0.036;
%Fog Attenuation Coefficient (dB)
Atm_Att= exp(-beta_l*Propagation_Len/1e3);                                 %
Fog path loss
Spc_Atm_Att=4.343.*beta_l*Propagation_Len/1e3;                             %
Specific Atmospheric Attenuation (dB/km)
disp(Spc_Atm_Att)

%% APD Parameters & Functions
Bw= 1e-6;                                          % bandwidth to bit rate
ratio (bps/Hz)
Rb=10e9;                                           % Data Rate
Rd=0.85;                                           % Responsivity
g=50;                                              % APD gain
Fn=2;                                              % Amplifier Noise
q=1.6023e-19;                                      % charge of electron (C)
Ka=0.7;                                            % Ionasation factor
Kb=1.38e-23;
Rl=50;                                             % APD Load Resistance
%% Port Elizabeth meteological Parameters
Temperature=17.82;
Windspeed=5.29;
Altitude=85;
Turbulences= 1.7e-14;
%-------------------------------------------Power---------------------------
```

```
Ptx_dB = linspace(-35,35,18);                                          %
Transmitted power range in dB
Ptx_mW =10.^(Ptx_dB/10);                                               %
Linear power mW
% SNR range in dB
SNR_dB_Range = linspace(0,35,18);
SNR_Range = 10.^(SNR_dB_Range/10);                                     %
Linear array
%% Turbulence channel analytical formulation
Cn2 = (0.00594*(Windspeed/27)^2*(10^-5*Altitude)^10*exp(-Altitude/1000)) + ...
      (2.7e-16*exp(-Altitude/1500)) + (Turbulences*exp(-Altitude/100));

x_Sm = 2*pi/WaveL;                                                     %
wave number (rad/m)
zig2_X = 1.23*Cn2*x_Sm^(7/6)*Propagation_Len^(11/6);          % Rytov variance

%--------logarithmic major-scale scintillation---------------
XY2 = (0.49*zig2_X)./(1+1.11*(zig2_X).^(12/5)).^(7/6);
YZ2 =(0.51*zig2_X)./(1+0.69*(zig2_X).^(12/5)).^(5/6);
%----------- major-scale scintillation-------------
ALPH = 1/(exp(XY2) - 1);                                               %
large-scale scintillation
%-----------minor-scale scintillation-------------
BETTA = 1/(exp(YZ2) - 1);  % minor-scale scintillation
zig2_anl = 1/ALPH + 1/BETTA + 1/(ALPH*BETTA);                          %
analytical scintillation index (S.I)for Gamma-Gamma model
Game= gamma(ALPH)*gamma(BETTA);
% Gamma function of alpha and beta
I = ALPH*BETTA;
% received normalized I as a product of large and small scale atmospheric
effects
%% APD APD Receiver noise
SNR_dB_OOk=zeros(size(SNR_dB_Range));
SNR_dB_BPSK=zeros(size(SNR_dB_Range));
SNR_dB_DPSK=zeros(size(SNR_dB_Range));
SNR_dB=zeros(size(SNR_dB_Range));
Ptx=zeros(size(Ptx_mW));

for i = 1:length(Ptx_mW)

    Ptx=Ptx_mW(i);                                                     %
Upadte the dB power array
    Fa=Ka*g+(1-Ka)*(2-g^-1);                                           %
Excessive Nosie Factor
    Sigma_Th=(4*Temperature*Kb*Rb*Fn)/Rl;                              %
Thermal Noise
```

```
    Sigma_Sh= (2*q.*g^2.*Rd.*Fa.*Rb.*Ptx.*abs(I))+Sigma_Th;                 %
Shot Noise
    Sigma_N=Sigma_Th+Sigma_Sh;                                              %
Total Power Noise Variance
        %---OOK----%
    Rx_Signal_P_OOk=(2*Rd*Ptx).^2;                                          %
Avavarge Received signal (W): After APD conversion (Electrical Signal)
    SNR_dB_OOk(i) =10*log10(Rx_Signal_P_OOk/ Sigma_N);
%Update SNR (dB) array
    SNR_OOk = 10.^(SNR_dB_OOk/10);
    %---BPSK----%
    Rx_Signal_P_BPSK=(2*Rd*Ptx).^2;
%Avavarge Received signal (W): After APD conversion (Electrical Signal)
    SNR_dB_BPSK(i) =10*log10(Rx_Signal_P_BPSK/ Sigma_N); %Update SNR (dB) array
    SNR_BPSK = 10.^(SNR_dB_BPSK/10);
   %---DPSK----%
    Rx_Signal_P_DPSK=(2*Rd*Ptx).^2;                                         %
Avavarge Received signal (W): After APD conversion (Electrical Signal)
    SNR_dB_DPSK(i) =10*log10(Rx_Signal_P_DPSK/ Sigma_N);
%Update SNR (dB) array
    SNR_DPSK = 10.^(SNR_dB_DPSK/10);
end

%% ----Analytical OOK Modulation Capacity based on Gamma-Gamma models-----%%
C = 2^(ALPH + BETTA-2)*Bw/4*pi*log(2)*Game;
% constant
z = SNR_OOk*Spc_Atm_Att.^2*(16/(ALPH*BETTA)^2);
% parameters of meijer G function
        %----- parameter for meijer G function-----%
m1 = 1;
m2 = 1;
m3 = (1 - ALPH)/2;
m4 = (2 - ALPH)/2;
m5 = (1 - BETTA)/2;
m6 = (2 - BETTA)/2;

n1 = 1;
n2 = 0;
%--------parameter vector for meijer G function--------%
m = [m1, m2, m3, m4, m5,m6];
n = [n1, n2];
String = 'meijerG(1, 6, [%e, %e, %e, %e, %e, %e], [%e, %e], %e)';  % meijer G
function engine string
C_Anl_OOK = zeros(size(z));  % BER array

            %-------------Loop for Signal-to-Noise Raio value------------%
for Index_H = 1:length(SNR_dB_OOk)
```

```
MGFunction = evalin(symengine, sprintf(String, m, n, 2*z(Index_H)));       %
use engine to evaluate meijer G function;
 C_Anl_OOK(Index_H) = C*MGFunction;
% calculate BER
end
%% -----------Analytical BPSK Modulation Capacity vs SNR based on Gamma-Gamma
models-------------%%
Cc = 2^(ALPH + BETTA)*Bw/pi*(log(2))*Game;
% constant
Zz = SNR_BPSK*Spc_Atm_Att.^2*(16/(ALPH*BETTA)^2);
%----- parameter for meijer G function-----%
jj1 = 1;
jj2 = 1;
jj3 = (1 - ALPH)/2;
jj4 = (2 - ALPH)/2;
jj5 = (1 - BETTA)/2;
jj6 = (2 - BETTA)/2;

kk1 = 1;
kk2 = 0;
%--------parameter vector for meijer G function--------%
jj = [jj1, jj2, jj3, jj4, jj5,jj6];
kk = [kk1,kk2];
String = 'meijerG(1, 6, [%e, %e, %e, %e, %e, %e], [%e, %e], %e)';  % meijer G
function engine string
C_Anl_BPSK = zeros(size(Zz));  % BER array
         %----------Loop for Signal-to-Noise Raio value-------------%
for Index_J = 1:length(SNR_dB_BPSK)
MGFunction = evalin(symengine, sprintf(String, jj, kk, 2*Zz(Index_J)));      %
use engine to evaluate meijer G function;

 C_Anl_BPSK(Index_J) = Cc*MGFunction;  % calculate BER
end

%%-------Analytical DPSK Modulation BER based on Gamma-Gamma models--------%%
Ccc = 2^(ALPH + BETTA)*Bw/pi*(log(2))*Game;
% constant
Zzz = SNR_DPSK*Spc_Atm_Att.^2*(8/(ALPH*BETTA)^2);
% meijer G function parameter
                %-----parameter vector for meijer G function-----%
jjj1 = 1;
jjj2 = 1;
jjj3 = (1 - ALPH)/2;
jjj4 = (2 - ALPH)/2;
jjj5 = (1 - BETTA)/2;
jjj6 = (2 - BETTA)/2;
```

```
kkk1 = 1;
kkk2 = 0;
        %--------parameter vector for meijer G function--------%
jjj = [jjj1, jjj2, jjj3, jjj4,jjj5, jjj6];
kkk = [kkk1, kkk2];

String = 'meijerG(1, 6, [%e, %e, %e, %e, %e, %e], [%e, %e], %e)';  % meijer G
function engine string
C_Anl_DPSK= zeros(size(Zzz));  % BER array
        %----------------Loop for Signal-to-Noise Raio value--------------%
for Index_K = 1:length(SNR_dB_DPSK)
MGFunction = evalin(symengine, sprintf(String, jjj, kkk, 2*Zzz(Index_K)));  %
use engine to evaluate meijer G function;

 C_Anl_DPSK(Index_K) = Ccc*MGFunction;  % calculate BER
end

%% --------Plottinf Avarage BER vs. SNR Over GammaGamma Channel --% figure;
semilogy(SNR_dB_Range,C_Anl_BPSK ,'g -+','LineWidth', 2);
hold on;
semilogy(SNR_dB_Range,C_Anl_DPSK ,'b -*','LineWidth', 2);
hold on;
semilogy(SNR_dB_Range,C_Anl_OOK ,'r -*','LineWidth', 2);

legend({'BPSK Modulation','DPSK Modulation','OOK Modulation'});
xlabel('Average SNR(dB) in Gqeberha');
ylabel('Average Channel Capacity in (bps/Hz)');
string_paragraph = sprintf('Gamma-Gamma model with \\sigma_{R}^2 = %4.2f',
zig2_X);
string_title = sprintf('ACC vs. SNR for %s', string_paragraph);
title(string_title);
% title('SNR vs. Avarage BER Over GammaGamma Channel');
grid on;
```

Appendix F: Received Irradiance under different levels of turbulences

```
% April 2023
% FSO transmission under different modulation schemes over gamama-gamma
distribution channel
% Writer: Kholekile Mtshiza (20817081)
% Description: This code computes the probability of receiving a certain amount
of optical irradiance
% (light intensity) under different levels of atmospheric turbulence
conditions.
clc;
close all;
%------------------Propagation Distance (m)-----------------%
Propagation_Len = 500;
Propagation_Len01 = 500;
Propagation_Len02 = 1400;
Propagation_Len03 = 4000;
I=0.01:0.01:6;                                  % range of received optical
power values
%% turbulence channel
%-----coefficient parameters for turbulence strength------%
Cn02 = 4e-13;
Cn002 = 4e-13;                                  %Strong turbulence
Cn0002= 4e-14;                                  %Moderate turbulence
Cn00002= 4e-15;                                 %Weak turbulence
WaveL = 1550e-9;                                %Propagation wavelength (m)
k_Sim = 2*pi/WaveL;                             %wave number (rad/m)
%----------------Rytov variance----------------%
sig2_R_Sim = 1.23*Cn02*k_Sim^(7/6)*Propagation_Len^(11/6);
sig2_R_Sim1 = 1.23*Cn002*k_Sim^(7/6)*Propagation_Len01^(11/6);
sig2_R_Sim2 = 1.23*Cn0002*k_Sim^(7/6)*Propagation_Len02^(11/6);
sig2_R_Sim3 = 1.23*Cn00002*k_Sim^(7/6)*Propagation_Len03^(11/6);
%--------logarithmic major-scale scintillation---------------%
slnX2 = (0.49*sig2_R_Sim)./(1+1.11*(sig2_R_Sim).^(6/15)).^(7/6);
slnX02 = (0.49*sig2_R_Sim1)./(1+1.11*(sig2_R_Sim1).^(6/15)).^(7/6);
slnX002 = (0.49*sig2_R_Sim2)./(1+1.11*(sig2_R_Sim2).^(6/15)).^(7/6);
slnX0002 = (0.49*sig2_R_Sim3)./(1+1.11*(sig2_R_Sim3).^(6/15)).^(7/6);
slnY2 =(0.51*sig2_R_Sim)./(1+0.69*(sig2_R_Sim).^(6/15)).^(5/6);
slnY02 = (0.51*sig2_R_Sim1)./(1+0.69*(sig2_R_Sim1).^(6/15)).^(5/6);
slnY002 = (0.51*sig2_R_Sim2)./(1+0.69*(sig2_R_Sim2).^(6/15)).^(5/6);
slnY0002 = (0.51*sig2_R_Sim3)./(1+0.69*(sig2_R_Sim3).^(6/15)).^(5/6);
%----------- major-scale scintillation-------------
```

```
PHI = 1/(exp(slnX2) - 1);
PHI1 = 1/(exp(slnX02) - 1);
PHI2 = 1/(exp(slnX002) - 1);
PHI3 = 1/(exp(slnX0002) - 1);
%----------minor-scale scintillation-------------%
SAI = 1/(exp(slnY2) - 1);
SAI1 = 1/(exp(slnY02) - 1);
SAI2 = 1/(exp(slnY002) - 1);
SAI3 = 1/(exp(slnY0002) - 1);
%-------------analytical scintillation index for Gamma-Gamma model-----------%
sig2_I_GG_anl = 1/PHI + 1/SAI + 1/(PHI*SAI);
sig2_I_GG_anl1 = 1/PHI1 + 1/SAI1 + 1/(PHI1*SAI1);
sig2_I_GG_anl2 = 1/PHI2 + 1/SAI2 + 1/(PHI2*SAI2);
sig2_I_GG_anl3 = 1/PHI3 + 1/SAI3 + 1/(PHI3*SAI3);
Mean_GG_Sim_ANL = 1;                              % theoretical mean value of
the intensity after Gamma-Gamma turbulence
Var_GG_Sim_ANL = 1/PHI + 1/SAI + 1/(PHI*SAI);    % theoretical variance of the
intensity after Gamma-Gamma turbulence (Scintillation Index S.I)
%-----------------------Gamma-gamma-----------------------%
Gam= gamma(PHI)*gamma(SAI);
Gam1= gamma(PHI1)*gamma(SAI1);
Gam2= gamma(PHI2)*gamma(SAI2);
Gam3= gamma(PHI3)*gamma(SAI3);
%-----------------Parameter for Meijer-G function-----------------%
a = (PHI+SAI)/2;
a1 = (PHI1+SAI1)/2;
a2 = (PHI2+SAI2)/2;
a3 = (PHI3+SAI3)/2;

b1 = (PHI-SAI)/2;
b2 = (SAI-PHI)/2;
b01 = (PHI1-SAI1)/2;
b02 = (SAI1-PHI1)/2;
b001 = (PHI2-SAI2)/2;
b002 = (SAI2-PHI2)/2;

b0001 = (PHI3-SAI3)/2;
b0002 = (SAI3-PHI3)/2;

Pe  = (((PHI*SAI).^a).*(I.^(a-1)))/Gam...
.* meijerG([],[],[b1,b2],[],PHI.*SAI.*I);

Pe1  = (((PHI1*SAI1).^a1).*(I.^(a1-1)))/Gam1...
.* meijerG([],[],[b01,b02],[],PHI1.*SAI1.*I);
```

```
Pe2  = (((PHI2*SAI2).^a2).*(I.^(a2-1)))/Gam2...
.* meijerG([],[],[b001,b002],[],PHI2.*SAI2.*I);

Pe3  = (((PHI3*SAI3).^a3).*(I.^(a3-1)))/Gam3...
.* meijerG([],[],[b0001,b0002],[],PHI3.*SAI3.*I);

plot(I,Pe1,'b-','LineWidth', 2);
hold on
plot(I,Pe2,'g-','LineWidth', 2);
hold on
plot(I,Pe3,'r-','LineWidth', 2);
legend({'Strong','Moderate','Weak'});
xlabel('Received Normalised Irradiance, I');
ylabel('Gamma-Gamma PDF, f(I)');
title('Gamma-Gamma Channel PDF');
grid on;
```

Appendix G: Received Irradiance Computation

```
%April 2023
% Writer: Kholekile Mtshiza (20817081)
% Description: Gamma-Gamma PDF against the received irradiance and the
BesselFunction

clc;
close all;
Cn2=1e-13;
WaveL=1550e-9;
%% Parameters & Functions

% zigma= @(y)       (0.492*Cn2*((2*pi/WaveL)^(7/6))*y.^(11/6));
zigma= @(y)       (1.23*Cn2*((2*pi/WaveL)^(7/6))*y.^(11/6));
ALPH=    @(y)       (exp((0.49*zigma(y))./(1+1.11*(zigma(y)).^(12/5)).^(5/6))-
1).^(-1);
BETTA=   @(y)       (exp((0.51*zigma(y))./(1+0.69*(zigma(y)).^(12/5)).^(5/6))-
1).^(-1);
BesselFunction=   @(i,y)     besselk((ALPH(y)-
BETTA(y)),(2*sqrt(ALPH(y)*BETTA(y)*i)));

Game=    @(y)           gamma(ALPH(y))*gamma(BETTA(y));
albe=   @(y)          (ALPH(y)+BETTA(y))/2;
PDF=    @(i,Link)
(2*((ALPH(Link).*BETTA(Link)).^(albe(Link))).*(i.^((albe(Link)-
1))).*BesselFunction(i,Link))/Game(Link); %Gamma-Gamma Distribution PDF

ir=0:0.01:5;
i=10.^(ir/10);                  % Irradiance
Link=3000;

nexttile
plot(ir,PDF(i,Link(1)),'r+-','LineWidth', 0.1, 'MarkerSize', 3);
xlabel('Received Irradiance, I (dBm)');
ylabel('Probability Density Function');
title('Gamma-Gamma Channel PDF');
grid on;

nexttile
plot(ir,BesselFunction(i,Link(1)),'g+-','LineWidth', 0.1, 'MarkerSize', 3);
xlabel('Irradiance, I (dBm)')
ylabel('2nd Order Modified Bessel Function')
title('Bessel Function')
grid on;
```